Springer Theses
Recognizing Outstanding Ph.D. Research

Dan Li

Rail Crack Monitoring Using Acoustic Emission Technique

Springer

Springer Theses

Recognizing Outstanding Ph.D. Research

Aims and Scope

The series "Springer Theses" brings together a selection of the very best Ph.D. theses from around the world and across the physical sciences. Nominated and endorsed by two recognized specialists, each published volume has been selected for its scientific excellence and the high impact of its contents for the pertinent field of research. For greater accessibility to non-specialists, the published versions include an extended introduction, as well as a foreword by the student's supervisor explaining the special relevance of the work for the field. As a whole, the series will provide a valuable resource both for newcomers to the research fields described, and for other scientists seeking detailed background information on special questions. Finally, it provides an accredited documentation of the valuable contributions made by today's younger generation of scientists.

Theses are accepted into the series by invited nomination only and must fulfill all of the following criteria

- They must be written in good English.
- The topic should fall within the confines of Chemistry, Physics, Earth Sciences, Engineering and related interdisciplinary fields such as Materials, Nanoscience, Chemical Engineering, Complex Systems and Biophysics.
- The work reported in the thesis must represent a significant scientific advance.
- If the thesis includes previously published material, permission to reproduce this must be gained from the respective copyright holder.
- They must have been examined and passed during the 12 months prior to nomination.
- Each thesis should include a foreword by the supervisor outlining the significance of its content.
- The theses should have a clearly defined structure including an introduction accessible to scientists not expert in that particular field.

More information about this series at http://www.springer.com/series/8790

Dan Li

Rail Crack Monitoring Using Acoustic Emission Technique

Doctoral Thesis accepted by
the National University of Singapore, Singapore

Springer

Author
Dr. Dan Li
School of Civil Engineering
Hefei University of Technology
Hefei
China

Supervisors
Asst. Prof. Kevin Sze Chiang Kuang
Department of Civil and Environmental Engineering
National University of Singapore
Singapore
Singapore

Prof. Chan Ghee Koh
Department of Civil and Environmental Engineering
National University of Singapore
Singapore
Singapore

ISSN 2190-5053 ISSN 2190-5061 (electronic)
Springer Theses
ISBN 978-981-10-8347-1 ISBN 978-981-10-8348-8 (eBook)
https://doi.org/10.1007/978-981-10-8348-8

Library of Congress Control Number: 2018931484

Printed on acid-free paper

This Springer imprint is published by the registered company Springer Nature Singapore Pte Ltd. part of Springer Nature
The registered company address is: 152 Beach Road, #21-01/04 Gateway East, Singapore 189721, Singapore

Supervisor's Foreword

As Dan Li's main supervisor during her Ph.D. study, it is my pleasure to write this foreword for her thesis, accepted for publication within the Springer Theses book series.

Dr. Li obtained her bachelor's and master's degrees at the School of Civil Engineering, Central south University in China. She started her Ph.D. programme in August 2012 at the Department of Civil and Environmental Engineering, National University of Singapore, and graduated in January 2017. During her Ph.D. study, she exhibited outstanding self-motivation, ingenuity and perseverance. I would like to take this opportunity to send my congratulations again to Dr. Li on obtaining her Ph.D. degree and the Springer Theses Award.

This Ph.D. research is focused on the rail crack monitoring using acoustic emission (AE) technique under both laboratory and field environments. Crack is a common type of rail defects. Rail crack monitoring is needed in order to identify cracks in advance allowing the early repair to be carried out to ensure a smooth and safe operation of the railway system. Various ultrasonic and electromagnetic non-destructive testing (NDT) techniques are under research for efficient rail crack monitoring. Compared with other NDTs, AE technique is more sensitive to crack initiation and propagation, less influenced by the structural geometry, and more capable of long-distance and continuous crack monitoring. In view of its successful applications in the condition monitoring of structures from rolling bearings to bridges, AE technique is considered as a promising solution for the rail crack monitoring.

In order to acquire various AE waves related to rail cracks, fatigue tests were carried out on rail steel specimens in the laboratory, and pencil lead break (PLB) simulation and train-running tests were carried out on rail tracks in the field. The time–frequency characteristics and propagation features of AE waves in rail track and the influence of operational noise were investigated through wavelet analysis. Different types of AE waves were discriminated based on their energy distributions in the time–frequency domain, preliminarily through wavelet transform (WT) under laboratory environment and subsequently through synchrosqueezed wavelet transform (SWT) under field environment. A novel crack

sizing method using crack closure (CC)-induced AE waves was brought forward. The methodology for crack identification and location in the rail track was initially proposed to be the wavelet transform-based modal analysis (WTMA) method and finally upgraded to be a new method, Tsallis synchrosqueezed wavelet entropy (TSWE) with time. The time-TSWE was able to efficiently identify and locate cracks in the field with complex crack conditions and high operational noise. More importantly, it was suitable to detect not only surface cracks but also internal cracks. The performance of proposed crack monitoring strategy was validated by the analysis results of field tests. Overall, the AE rail crack monitoring strategy, in aspects of crack identification, location and sizing, as well as noise cancellation, proposed in this thesis is of great importance to the railway industry and academe.

On behalf of other authors, I sincerely acknowledge the efforts of the editorial team to make this book printed and published. We hope that you would find this book useful in your research/professional endeavours.

Singapore
August 2017

Asst. Prof. Kevin Sze Chiang Kuang

Parts of this thesis have been published in the following journal articles:

- **Li, D.** *, Kuang, K. S. C., Koh, C. G. (2017). Rail crack monitoring based on Tsallis synchrosqueezed wavelet entropy of acoustic emission signals: a field study. *Structural Health Monitoring*. Prepublished online December 4, 2017, DOI: 10.1177/1475921717742339.
- **Li, D.**, Kuang, K. S. C. *, Koh, C. G. (2017). Fatigue crack sizing in rail steel using crack closure-induced acoustic emission waves. *Measurement Science and Technology*. 28(6): 065601.
- Kuang, K. S. C., **Li, D.***, Koh, C. G. (2016). Acoustic emission source location and noise cancellation for crack detection in rail head. *Smart Structures and Systems*. 18(5): 1063–1085.

Acknowledgements

First of all, I would like to express my deepest appreciation to my two supervisors, Dr. Kevin Sze Chiang Kuang and Prof. Chan Ghee Koh. Without them, my Ph.D. study in National University of Singapore would not have been possible. I am grateful for their support, guidance and motivation. Their critical and rigorous attitude in research and other aspects will leave a long-term impact on my life.

Great acknowledgments are expressed to the Wuhan Railway Bureau in China who helped to arrange the field tests. Without their help, my Ph.D. study would not be completed with success. Thanks also go to the staffs in the structural laboratory, Mr. Beng Oon Ang, Mr. Stanley Kah Wai Wong, Mr. Bin Rasman Kamsan and Mr. Yian Kheng Koh, and to my friends in NUS, Dr. Abraham Christian, Mr. Bin Yan, Dr. Shan-Li Zhang and Dr. Shan Yang. Without their assistance, my experimental work would not have been finished. In addition, helpful suggestions on the AE instrumentation from Dr. Jason Dong from MISTRAS Group, Inc. are also appreciated.

Heartfelt gratitude is sent to Prof. Wei-Xin Ren and Assoc. Prof. Dong Yang at Hefei University of Technology and Assoc. Prof. Yi-Ding Hu at Wuyi University for the valuable discussions on signal processing algorithms and field tests.

I would like to thank my parents and brother for their unconditional love and moral support. I would also like to give thanks to all my friends for their sweet company and help. They are my inspiration throughout this journey.

Last but not least, financial supports in the form of NUS Research Scholarship and the NUS Academic Research Fund (Grant No. R-302-000-097-112) are gratefully acknowledged.

Contents

Abbreviations

AE	Acoustic emission
CC	Crack closure
COD	Crack opening displacement
CP	Crack propagation
CWT	Continuous wavelet transform
HT	Hilbert transform
KDE	Kernel density estimation
MAD	Median absolute deviation
NDT	Non-destructive testing
PDF	Probability density function
PLB	Pencil lead break
PSD	Power spectral density
RCF	Rolling contact fatigue
RMS	Root mean square
SEM	Scanning electron microscope
SNR	Signal-to-noise ratio
SWE	Shannon wavelet entropy
SWT	Synchrosqueezed wavelet transform
TOA	Time-of-arrival
TSWE	Tsallis synchrosqueezed wavelet entropy
WP	Wavelet power
WT	Wavelet transform
WTMAL	Wavelet transform-based modal analysis location

Nomenclature

a	Crack length
a_i	Crack length at the ith load cycle
B	Thickness of rail steel specimen
c_c	AE counts induced by crack closure
c_p	AE counts induced by crack propagation
C	Positive constant in the gamma correction
C_0, C_1, C_2 and C_3	Material constants in the crack sizing methods
C_i	Experimental compliance at the ith load cycle
d	Distance from the AE source to the sensor
d_0	Distance between two sensors
d_1 and d_2	Distances between AE source and two sensors
E	Modulus of elasticity
E^S	Shannon entropy
E^S_{WT}	Shannon entropy of wavelet coefficients
E^T	Tsallis entropy
E^T_{SWT}	Tsallis entropy of synchrosqueezed wavelet coefficients
f	Frequency in Hz
f_b	Bandwidth parameter of complex Morlet wavelet
f_c	Central frequency of complex Morlet wavelet
K	Stress intensity factor
L	Length of time window
n_v	Number of voices in the synchrosqueezed wavelet transform
q	Non-extensive parameter
p	Energy probability distribution of wavelet coefficients
P	Fatigue load
swt	Synchrosqueezed wavelet coefficients
S	Support span of rail steel specimen
t	Time
t_1 and t_2	Arrival times of AE wave at two sensors
$t_{1,1}$ and $t_{1,2}$	Arrival times of M1 at the two sensors

$t_{2,1}$ and $t_{2,2}$	Arrival times of M2 at the two sensors
T	Threshold value in the synchrosqueezed wavelet transform
v_m	Crack mouth opening displacement at notched edge
V	Velocity of AE wave propagating in the rail head
V_1 and V_2	Group velocities of M1 and M2
wt	Wavelet coefficients
W	Width of rail steel specimen
α_0 and α_1	Material constants in the crack sizing methods
β_0, β_1 and β_2	Material constants in the crack sizing methods
γ	Positive constant in the gamma correction
γ_0, γ_1, γ_2 and γ_3	Material constants in the crack sizing methods
ψ	Wavelet function
$\hat{\psi}$	Fourier transform of wavelet function
ω	Angular frequency
ω_c	Cut-off frequency in the Hilbert transform-based noise cancellation method

List of Figures

List of Tables

Summary

Crack monitoring of rail tracks aims to identify fatigue cracks in advance allowing the timely repair to be carried out to ensure a smooth and safe operation of the railway system. Acoustic emission (AE) technique is a promising tool for crack monitoring that is highly sensitive to crack growth and able to detect cracks over long distances. Research on rail crack monitoring using AE technique to date is limited to laboratory fatigue tests and small-scale test rigs. However, real rail profile has a strong impact on the propagation features of AE waves. Complex crack conditions and noisy environment in the field may significantly reduce the performance of crack detection algorithms. In addition, it is still a challenge to accurately quantify the size of fatigue cracks. In this context, this thesis studies the strategy for AE rail crack monitoring based on a series of laboratory and field tests, in aspects of crack identification, location and sizing, as well as noise cancellation.

The focus of this study was to investigate AE waves induced by different mechanisms, i.e. pencil lead break (PLB), crack propagation (CP), crack closure (CC), wheel–rail impact and railway noise. Through continuous wavelet analysis (CWT), it was found that AE waves behave with dispersion when propagating along the rail head and that the energy distribution of different types of AE waves varies in the time-frequency domain. The classification of different types of AE waves was carried out by using the wavelet power (WP)-based index and the enhanced synchrosqueezed wavelet transform (SWT) scalogram.

It was of interest to develop a crack sizing method, and this was done through laboratory fatigue tests on rail steel specimens. Here, a novel method to quantify fatigue crack length was proposed by taking advantage of the CC-induced AE waves. In contrast to other methods, the proposed method does not require prior knowledge of initial crack length, integration of AE data or real-time load amplitude, allowing it to be applied to both new and existing structures. The experimental results validated the ability of the proposed method to determine the crack length with good accuracy.

The crack location method under field environment was studied initially based on PLB-simulated AE sources and subsequently with real rail cracks. For PLB-simulated AE sources which are widely used in the literature, the wavelet

transform-based modal analysis location (WTMAL) method was able to locate the AE sources in a range of 30.0 m with errors less than 0.3 m. However, this could not be achieved under field environment where complex crack conditions and high operational noise exist. Tsallis synchrosqueezed wavelet entropy (TSWE) with time was then proposed to detect the crack-related AE transients in order to identify the existence and location of cracks. After the key parameters were appropriately determined, the time-TSWE successfully located an incipient rolling contact fatigue (RCF) crack at 11.7 m away from the sensor with errors less than 0.3 m. In the crack monitoring strategy proposed, the working distance of AE sensors is relatively short compared to the length of railway lines. An efficient use of AE technique would be to deploy the sensors at critical rail sections such as curved sections where lateral forces result in high occurrences of cracks.

Chapter 1
Introduction

1.1 Background

Rail defects due to dynamic wheel-rail interaction and environmental exposure could result in catastrophic failures. Every year millions of Euros are being spent on the maintenance and renewal of large railway network in Europe. However, accidents still happen occasionally (Esveld 2001). The Hatfield train derailment in 2000 is a tragic example of fractured rail track that went undetected (Fig. 1.1) (Office of Rail Regulation 2006). In the United States, broken rails or welds are the leading derailment causes on main, yard, and siding tracks (Liu et al. 2012). The cases are similar in other countries, such as the Mass Rapid Transit (MRT) system in Singapore (AsiaOne Transport 2013) and the nationwide railway network in China.

To date, the maintenance of rail tracks worldwide mainly depends on the scheduled inspections carried out manually by technicians or automatically by inspection trains or vehicles. Manual inspections are time consuming, labor intensive and costly to carry out. Instrumented inspection trains perform well in detecting obvious geometrical and large surface defects but not small surface or internal cracks. The speed of train-based inspection is slow when conventional non-destructive testing (NDT) methods are utilized to detect local defects (Clark 2004). Moreover, scheduled inspections are infrequent and may miss potentially dangerous defects prior to the next inspection. As a result, there is a need to change from scheduled inspection to condition monitoring using effective techniques with instruments installed on the track (Goodall and Roberts 2006; Ostachowicz and Güemes 2013; Thakkar et al. 2010). Condition monitoring of rail tracks helps to identify defects in advance allowing early repair to be carried out to ensure a smooth and safe operation of the railway system.

Fatigue cracks are the primary defects in rail track. Rail crack monitoring is complex for a number of reasons. The rail track could extend for thousands of kilometers in length, which require that the technique deployed is capable of detecting cracks over long distances. As the cross-section of the rail track is

D. Li, *Rail Crack Monitoring Using Acoustic Emission Technique*,
Springer Theses, https://doi.org/10.1007/978-981-10-8348-8_1

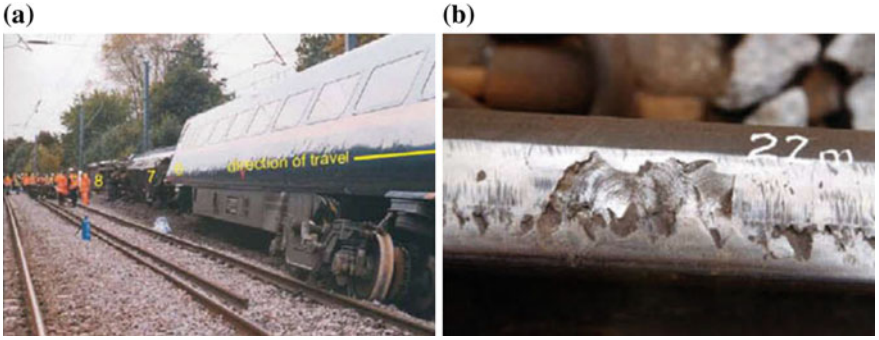

Fig. 1.1 Hatfield rail crash: **a** derailed train **b** rail head condition (Office of Rail Regulation 2006)

irregular, the use of traditional ultrasonic techniques are less efficient. More significantly, the crack conditions of rail track in the field are very complex. Small cracks at their early stages or shallow-angle cracks are not easily identified even by existing advanced NDT techniques (Esveld 2001; Grassie et al. 2011).

To achieve a more efficient rail crack detection process for in-service rail condition monitoring, various ultrasonic and electromagnetic NDT techniques are being researched, which include the use of acoustic emission (AE) technique (Papaelias et al. 2008; Pohl et al. 2004). AE refers to the generation of transient stress waves due to the sudden release of elastic strain energy in a structure during processes of plastic deformation, crack initiation and propagation, fracture, impact, etc. With frequencies ranging from 20 kHz to 1 MHz, AE waves contain valuable information related to the microstructural changes in the material and therefore can be used to detect structural defects without any external ultrasonic inputs. Compared with other NDT approaches, AE technique is known to be more sensitive to crack initiation and propagation, less susceptible to complex structural geometry, capable of crack detection over longer distances and suitable for in-service condition monitoring (Ono 2007). It would hence be an ideal candidate for rail crack monitoring.

AE technique has demonstrated excellent performances in identifying the presence of cracks and their locations in various types of structures. However, it is still a challenge to accurately quantify the size of a fatigue crack using the AE signals (Gagar et al. 2014). Moreover, although AE technique has been successfully used for condition monitoring of roller bearings, tanks and bridges (Nair and Cai 2010; Pandya et al. 2013; Zárate et al. 2014), its application to rail tracks is still limited to laboratory studies, such as fatigue tests on rail steel specimens (Bassim et al. 1994; Kostryzhev et al. 2013) and small-scale test rigs simulating the wheel-rail interaction (Bruzelius and Mba 2004; Thakkar et al. 2010; Zhang et al. 2015a). There is still limited attention given to the propagation features and source location of AE waves in the rail track over long distances, and the AE crack detection in rail track under field condition with complex crack formations, varying train loads and noisy environment.

1.2 Objectives and Scope of Research

This thesis is focused on the study of AE technique applied to rail crack monitoring. Specifically, methodologies for crack identification, location and sizing are investigated and proposed under laboratory and field environments. The detailed objectives of this research are summarized as follows:

(1) To investigate the time-frequency characteristics of AE waves induced by different mechanisms related to rail crack and operational noise.
(2) To explore the propagation characteristics and source location method of AE waves along the rail.
(3) To quantify the size of the crack based on AE signals of rail steel specimens recorded during laboratory fatigue tests.
(4) To study the crack identification, location and noise cancellation methods for field rail track with complex crack conditions and noisy operational environment.

It is expected the proposed algorithms and the results of experimental tests will offer further insights and recommendations into the application of AE technique for rail crack monitoring. The methods proposed for crack detection, crack location and noise cancellation were developed based on field tests carried out in this study and was demonstrated to be practical for field application. The crack sizing method proposed here however was limited to laboratory fatigue specimens in view of the difficulty in obtaining good quality field data. Future study with repeated testing conditions is needed in order to extend the proposed crack sizing to field applications.

1.3 Research Significance

This research makes several contributions towards realizing the practical application of AE technique in rail crack monitoring. Several new approaches to interpret AE signals are investigated to identify the rail cracks. A rail crack monitoring strategy is proposed, comprising of a noise cancellation method, an AE wave classification method, a crack sizing method, and a crack identification and location method. More specifically, the original contributions of this thesis are summarized as follows:

(1) AE waves induced by different mechanisms related to rail cracks, respectively crack propagation (CP), crack closure (CC), impact and field rolling noise, are obtained. It is found that the energy distribution of different AE waves varies in the time-frequency domain.
(2) The study of dispersion and attenuation features of AE waves propagating along rail track provides the fundamental understanding of the identification and location of AE sources in rail track.
(3) A novel crack sizing method is developed by taking advantage of the CC-induced AE waves. The method proposed is shown to be able to evaluate

the size of fatigue crack without prior knowledge of the initial crack status, integration of AE data and load amplitudes.

(4) The Tsallis synchrosqueezed wavelet entropy (TSWE) with time is put forward as a method which is able to identify the existence and location of cracks in the field rail track with complex crack conditions and noisy environment. Its performance is validated by the results of field tests conducted in this study.

(5) The classification of different types of AE waves is made based on their time-frequency characteristics. A wavelet power (WP)-based classification index is proposed to distinguish between AE waves induced by CP and CC respectively. Furthermore, the enhanced SWT scalogram is suggested leading to a more accurate classification of AE waves induced by several different mechanisms related to rail cracks occurring under field condition.

1.4 Thesis Outline

Chapter 1 describes the rationale and motivation behind this study, listing the research objectives, and the new contributions made to existing body of knowledge and practice.

Chapter 2 reviews published works relevant to the thesis topic, including an overview of common defects in rail track, a summary of existing rail condition monitoring techniques, an introduction of the AE technique and its potential in rail crack monitoring, and discussions of the way forward.

Chapter 3 presents the propagation features and source location of AE waves in rail track based on field tests, where AE sources, i.e. cracks, are simulated by the pencil lead break (PLB). Wavelet transform (WT) is introduced to explore the dispersion phenomena of AE waves propagating in the rail head. Two source location methods, respectively time-of-arrival (TOA) method and wavelet transform based modal analysis location (WTMAL) method, were compared. The influence of operational noise on the crack location is also studied.

Chapter 4 studies the fatigue crack sizing in rail steel using AE waves, recorded during laboratory fatigue tests on specimens cut from rail head. As a pre-processing step, a classification index based on WP is established to distinguish between the CP-induced AE waves and the CC-induced AE waves. Following the AE wave classification, a novel method to quantify fatigue crack size is developed.

Chapter 5 studies the crack monitoring of field rail track using AE signals recorded through field tests on operational railway. Synchrosqueezed wavelet transform (SWT) is introduced to analyze AE signals to achieve a clearer time-frequency representation. The Tsallis synchrosqueezed wavelet entropy (TSWE) with time is put forward to identify and locate the crack in rail track. The enhanced SWT scalogram is proposed to classify different types of AE waves related to the crack.

Chapter 6 concludes the thesis with highlights of the main findings and recommendations for future work.

An overview of the thesis structure is given in Fig. 1.2. Chapters 3 and 4 which outlines controlled laboratory and field experimental work set the basis for field implementation described in Chap. 5 involving detection of actual rail cracks under field loading conditions.

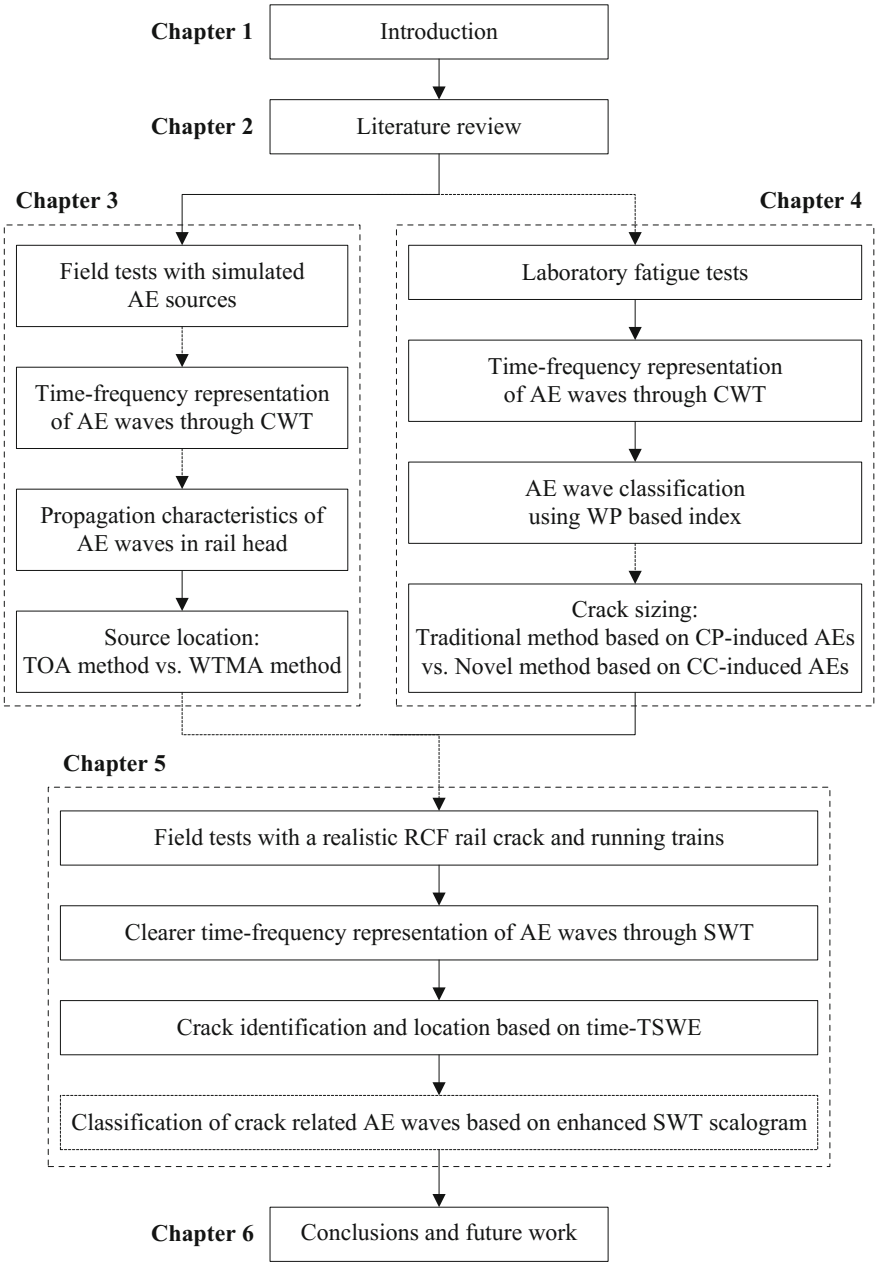

Fig. 1.2 Thesis structure overview

References

AsiaOne Transport. (2013). SMRT in talks with LTA for complete rail overhaul. Retrieved from http://transport.asiaone.com/news/general/story/smrt-talks-lta-complete-rail-overhaul.

Bassim, M. N., Lawrence, S. S., & Liu, C. D. (1994). Detection of the onset of fatigue crack growth in rail steels using acoustic emission. *Engineering Fracture Mechanics, 47*(2), 207–214.

Bruzelius, K., & Mba, D. (2004). An initial investigation on the potential applicability of acoustic emission to rail track fault detection. *NDT and E International, 37*(7), 507–516.

Clark, R. (2004). Rail flaw detection: Overview and needs for future developments. *NDT and E International, 37*(2), 111–118.

Esveld, C. (2001). *Modern railway track* (2nd ed.). Zaltbommel: MRT-Productions.

Gagar, D., Foote, P., & Irving, P. (2014). A novel closure based approach for fatigue crack length estimation using the acoustic emission technique in structural health monitoring applications. *Smart Materials and Structures, 23*(10), 105033.

Goodall, R. M., & Roberts, C. (2006). Concepts and techniques for railway condition monitoring. In *IET International Conference on Railway Condition Monitoring*. Birmingham, UK, 90–95.

Grassie, S. L., Fletcher, D. I., Hernandez, E. G., & Summers, P. (2011). Studs: A squat-type defect in rails. *Proceedings of the Institution of Mechanical Engineers, Part F: Journal of Rail and Rapid Transit, 226,* 243–256.

Kostryzhev, A. G., Davis, C. L., & Roberts, C. (2013). Detection of crack growth in rail steel using acoustic emission. *Ironmaking and Steelmaking, 40*(2), 98–102.

Liu, X., Saat, M., & Barkan, C. (2012). Analysis of causes of major train derailment and their effect on accident rates. *Transportation Research Record: Journal of the Transportation Research Board, 2289*, 154–163.

Nair, A., & Cai, C. S. (2010). Acoustic emission monitoring of bridges: Review and case studies. *Engineering Structures, 32*(6), 1704–1714.

Office of Rail Regulation. (2006). *Train derailment at hatfield: A final report by the independent investigation board*.

Ono, K. (2007). Structural integrity evaluation using acoustic emission. *Journal of Acoustic Emission, 25,* 1–20.

Ostachowicz, W., & Güemes, J. A. (Eds.). (2013). *New trends in structural health monitoring*. Udine, Italy: Springer.

Pandya, D. H., Upadhyay, S. H., & Harsha, S. P. (2013). Fault diagnosis of rolling element bearing with intrinsic mode function of acoustic emission data using APF-KNN. *Expert Systems with Applications, 40*(10), 4137–4145.

Papaelias, M. P., Roberts, C., & Davis, C. L. (2008). A review on non-destructive evaluation of rails: State-of-the-art and future development. *Proceedings of the Institution of Mechanical Engineers, Part F: Journal of Rail and Rapid Transit, 222*(4), 367–384.

Pohl, R., Erhard, A., Montag, H. J., Thomas, H. M., & Wüstenberg, H. (2004). NDT techniques for railroad wheel and gauge corner inspection. *NDT and E International, 37*(2), 89–94.

Thakkar, N. A., Steel, J. A., & Reuben, R. L. (2010). Rail-wheel interaction monitoring using Acoustic Emission: A laboratory study of normal rolling signals with natural rail defects. *Mechanical Systems and Signal Processing, 24*(1), 256–266.

Zárate, B. A., Pollock, A., Momeni, S., & Ley, O. (2014). Structural health monitoring of liquid-filled tanks: A Bayesian approach for location of acoustic emission sources. *Smart Materials and Structures, 24*(1), 015017.

Zhang, X., Feng, N., Wang, Y., & Shen, Y. (2015). Acoustic emission detection of rail defect based on wavelet transform and Shannon entropy. *Journal of Sound and Vibration, 339,* 419–432.

Chapter 2
Literature Review

This chapter reviews literature relevant to rail crack monitoring, which includes an overview of common defects in rail track, a summary of current rail condition monitoring techniques, an introduction of AE technique and its potential in rail crack monitoring, and discussions of the way forward.

2.1 Common Defects of Rail Track

Due to the complicated wheel-rail interaction under repeated traffic load, rail track is subjected to physical and chemical reactions, resulting in various types of defects. Based on the review of information from literature and railway manuals (ARTC 2006; Cannon et al. 2003; Esveld 2001; Jeong and Orringer 1989; Thakkar 2009; UIC 2002), common defects rail track could be divided roughly into six categories: cracks, wears, geometrical deflections, squeezing out of edge, bad welds and other defects (Table 2.1), according to their initiation mechanisms and physical manifestations. It is commonly acknowledged that fatigue cracks are the primary defects in rail track. The rail head is the most vulnerable part of the rail track where surface and internal cracks are frequently found. As this work focuses mainly on surface and internal cracks, a more in-depth review of such types of defects will be given here. Details of other defects can be found in the references (ARTC 2006; Esveld 2001).

2.1.1 Surface Cracks

Rolling contact fatigue (RCF) is associated with plastic deformation under wheel-rail contact forces. Cracks could be then initiated as a result of the unidirectional accumulation of strain and propagate under successive application of high

D. Li, *Rail Crack Monitoring Using Acoustic Emission Technique*,
Springer Theses, https://doi.org/10.1007/978-981-10-8348-8_2

Table 2.1 Categories of normal rail track defects

No	Categories	Subcategories	
1	Cracks	RCF-induced surface cracks	Head checks
			Gauge corner cracks
			Squats
		Internal cracks	Tache ovale
			Split heads
			Split webs
			Cracks in rail foot
		Cracks at web-head fillet radius	
		Cracks emanating from bolt holes	
		Shellings	
2	Wears	Corrugations	Short pitch corrugations
			Long pitch corrugations
		Wheel burns	
3	Geometrical deflections	Vertical deflections	
		Horizontal deflections	
4	Squeezing out of edge	–	
5	Bad welds	–	
6	Other defects	–	

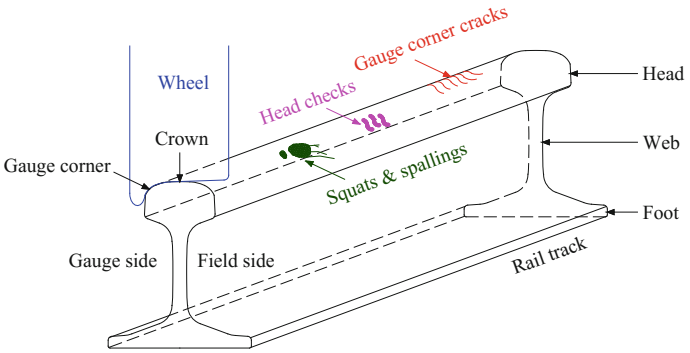

Fig. 2.1 Schematic of the positions of RCF-induced surface cracks

and complicated stresses (Thakkar 2009). RCF is known to cause damages in curve sections of rail tracks (even including relatively new ones of about a year old), as well as at tangent sections where wheel hunting behavior is common. RCF-induced surface cracks include three types and there are gauge corner cracks, head checks and squats. Figure 2.1 shows a schematic of their positions on the cross-section of the rail.

Gauge corner cracks appear within the region of up to 10 mm from the gauge face. They are initiated at or very close to the track surface, and typically occur at

intervals of several millimeters to centimeters along the rail track and at angles of 30°–90° relative to the longitudinal direction (Fig. 2.2). In addition, they can grow to 2–5 mm in depth at a downward angle of about 10°–30° to the surface, and then gradually spread across the rail head if remedial action is not taken in time (Fig. 2.3).

Head checks typically occur on the crown of the rail head as shown in Fig. 2.4. Similar to gauge corner cracks, they are initiated from mosaic or snakeskin-like patterns covering several decimeters to meters along the rail track, and subsequently propagate deeper into the rail producing spallings up to 10–15 mm wide and 3 mm deep. As the radius of curve reduces, the position of cracks moves from the rail crown towards the gauge corner (Thakkar 2009).

Squats (Fig. 2.5) are generally initiated from hard and brittle "white etching" layers, which forms on the crown surface of rail head under adiabatic shear stresses. Micro cracks on the other hand arise from the running surface of track, and propagate slowly through the heavily deformed surface layers, in a shallow plain of 10°–25° angle. After reaching a depth of 3–5 mm, cracks will branch either

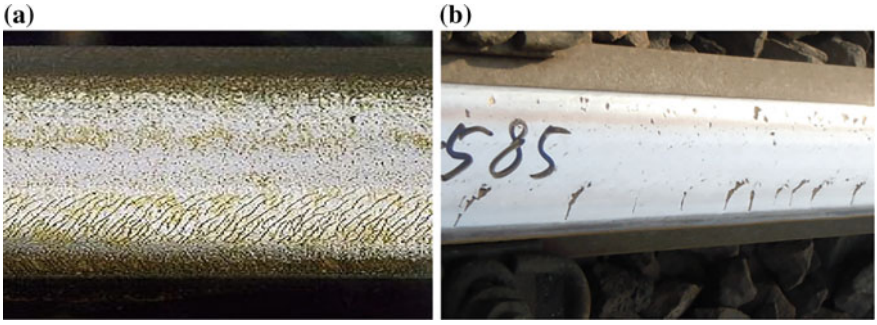

Fig. 2.2 Gauge corner cracks: **a** minor ones (ARTC 2006) and **b** severe ones with spallings

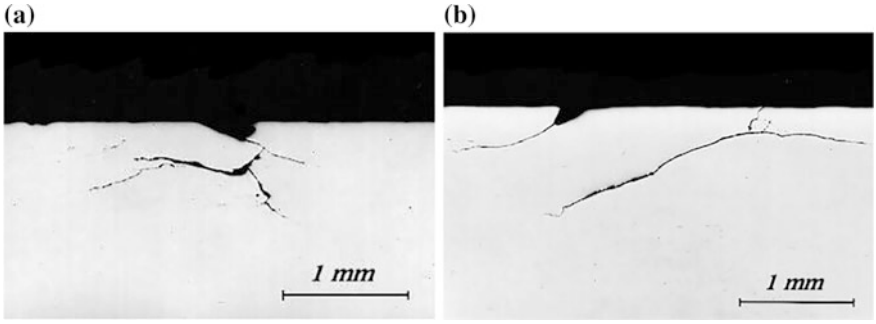

Fig. 2.3 Sections of rail head showing the initial stage of gauge corner cracks (ARTC 2006): **a** transverse and **b** longitudinal

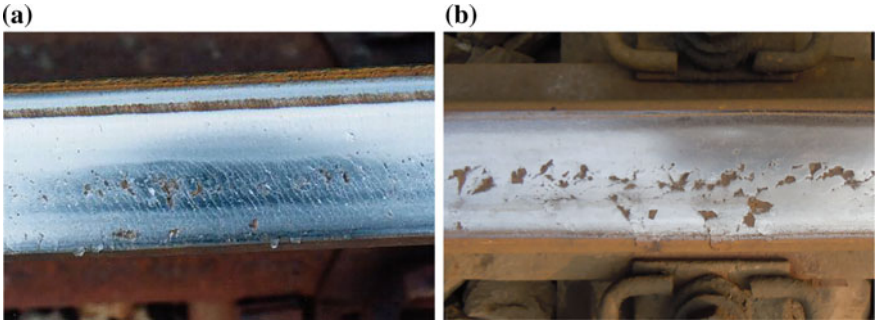

Fig. 2.4 Head checks: **a** minor ones (ARTC 2006) and **b** severe ones with spallings

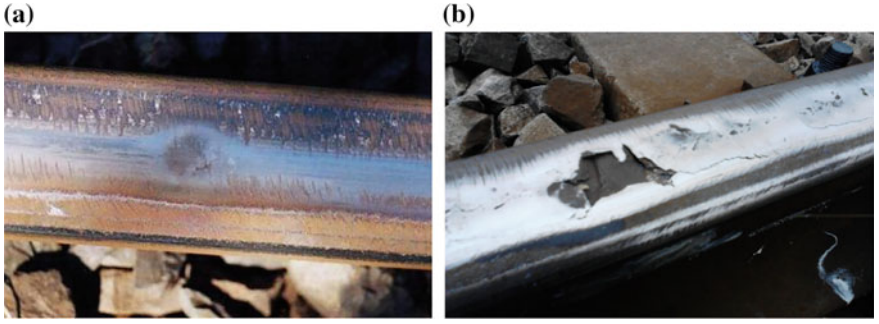

Fig. 2.5 Squats: **a** minor one (ARTC 2006) and **b** severe one with spallings

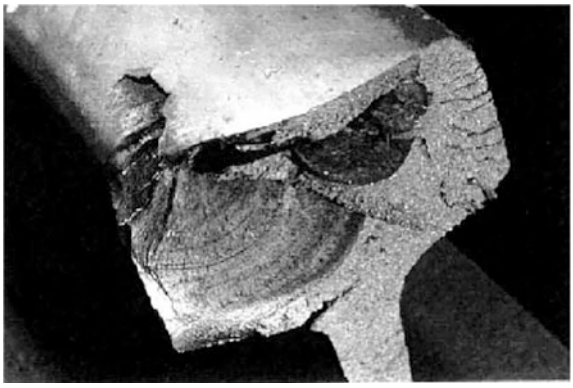

Fig. 2.6 A broken rail caused by head checks (Czichos et al. 2006)

upwards to form spallings or downwards to form transverse cracks (Cannon et al. 2003; Vidaud and Zwanenburg 2009).

RCF-induced cracks are not only found on the surface but could penetrate deeper into the rail, resulting in the possibility of rail break, an example of which is presented in Fig. 2.6. Moreover, depressions and spallings coupled with cracks

would cause higher dynamic contact force, and that in turn accelerates the crack propagation. Various cracks may intersect each other, making them difficult to detect.

2.1.2 Internal Cracks

Internal cracks include tache ovales, split heads, split webs and cracks in rail foot. They form mostly at initial imperfections due to stress concentration, and would propagate under continuously repeated axle loads (Ekberg and Kabo 2005). For instance, a tache ovale (Fig. 2.7) defect is initiated because of the excessive hydrogen atoms which combine at the grain boundaries or inclusions, forming pockets of molecular hydrogen that markedly increases the internal pressure. Once develops, it may grow in the transverse direction under complex stresses imposed by trains (ARTC 2006). These cracks are internal and therefore hidden, and they are mainly detected using ultrasonic means.

2.2 Current Rail Monitoring Techniques

Based on the literature review, current NDT techniques for rail crack detection or monitoring are categorized into six groups, which are acceleration-based technique, automated visual technique, ultrasonic techniques, electromagnetic techniques, magnetic induction technique and others, respectively, as listed in Table 2.2 (Clark 2004; INNOTRACK 2008; Papaelias et al. 2008). Some of these, like the acceleration-based technique, visual technique and conventional ultrasonics, have already been applied in the railway industry, while the rest of the techniques are still

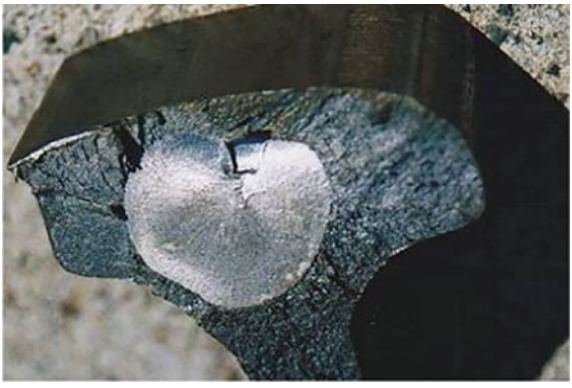

Fig. 2.7 A tache ovale (ARTC 2006)

Table 2.2 Categories of rail track monitoring techniques

No	Categories	Subcategories
1	Acceleration-based technique	–
2	Automated visual technique	–
3	Ultrasonic techniques	Conventional ultrasonics
		Long-range ultrasonics using guided wave
		Laser-based ultrasonics
		Electromagnetic acoustic transducers
		Acoustic emission
4	Electromagnetic techniques	Eddy current
		Alternating current field measurement
5	Magnetic induction technique	–
6	Other techniques	–

being studied and improved. A brief introduction of these techniques (except AE, which will be elaborated in Sects. 2.3 and 2.4) is given in this section.

2.2.1 Acceleration-Based Technique

Acceleration-based technique utilizes accelerometers installed on the inspection train to test running stability and to estimate the rail condition (Remennikov and Kaewunruen 2008). The recorded acceleration of bogie would change in frequency and amplitude if defects exist in the rail track. Using appropriate signal processing algorithms, this technique can detect surface rail defects with obvious geometrical deformation, like corrugations and abnormal deflections. Quantitative detection of rail defects, especially those of small sizes, based on this method is still under research and development (Cantero and Basu 2014; Molodova et al. 2014).

2.2.2 Automated Visual Technique

Automated visual technique employs high-speed and high-resolution cameras installed on the inspection train to capture images of rail track. It can measure rail profile, integrity of fish plate, missing bolts and even condition of sleepers and ballast at speeds up to 200 km/h (De Ruvo et al. 2008; Li and Ren 2012). However, when the resolution of images needs to be increased in order to identify wears and cracks, the large amount of data puts a constraint on the train speed. As Papaelias et al. (2008) stated, this technique cannot reliably detect surface breaking defects at speeds greater than 4 km/h. Furthermore, visual technique could not provide any information related to the depth of defects or detect the presence of internal defects.

2.2.3 *Ultrasonic Techniques*

(1) Conventional ultrasonics

Ultrasonic techniques are the primary means for crack detection in the railway industry. The conventional ultrasonics is widely applied in both manual inspections and automatic inspection trains. A beam of ultrasonic energy generated by a piezoelectric element is transmitted into the rail track, which is then reflected or scattered and finally detected by the receiving transducer. Defects, if any, could be identified and located according to the amplitude and time information embedded in the reflected signal. Several transducers can be arranged in different incident angles in order to cover various parts of the rail cross-section (Clark et al. 2002; Pearson 2002). Generally speaking, conventional ultrasonics performs well in detecting deep surface-breaking and internal defects in the rail head and web. However, RCF-induced surface cracks with depths of less than 3–5 mm at their early crack growth stages cannot usually be identified. Such surface cracks or shellings may even mask internal defects (Cannon et al. 2003). It is highly likely that defects at the rail foot could be missed since they can only be partially scanned. In addition, the speed of inspection trolley using conventional ultrasonic (shown in Fig. 2.8) is normally limited to 3 km/h, while that of inspection train (shown in Fig. 2.9) is less than 100 km/h, depending on the instruments and track quality (Esveld 2001).

(2) Long-range ultrasonics

Long-range ultrasonics utilizes guided waves propagating along rail track for crack detection, instead of body waves transmitting across the section (Bartoli et al. 2005; Fan et al. 2007; Rose et al. 2004). Guided waves travel over a given distance with less energy loss compared to body waves. The detecting range of this technique can go up to several hundred meters theoretically. However, various practical factors may adversely affect the ultrasonic wave and attenuate its energy significantly. In some cases, the effective range has been reported to be only a few meters. Recently, non-contact transducers have been proposed for generating and collecting guided

Fig. 2.8 Ultrasonic probe system on the JGT-10 portable rail detector provided by the Lu Chao Ltd (China)

Fig. 2.9 Ultrasonic probe system on the Multi Function Vehicle provided by the Plasser & Theurer (Austria)

ultrasonic waves in the rail track (Mariani et al. 2013). Overall, this technique is still immature and requires further research in order to improve its sensitivity, reliability and inspection speed.

(3) Laser-based ultrasonics

As a remote implementation of conventional ultrasonic inspection system, laser-based ultrasonics initially employs pulsed lasers to generate ultrasonic waves and laser ultrasonic receivers to collect the structural response (Scruby and Drain 1990). Recently, laser-air hybrid ultrasonic technique (LAHUT) (Kenderian et al. 2006) was proposed by combining laser-based generation of input ultrasound with air-coupled detection of output ultrasound. Laser-based ultrasonic generation apparatus could be located several meters away from the interrogated surface, while for the air-coupled acoustic transducers, this could be several centimeters away. Successful experimental results have proven its ability to detect vertical split head rail and base cracks. The inspection speed of a LAHUT system installed on a hi-rail vehicle was reported to be 8–15 km/h (INNOTRACK 2008). More research is still needed to improve its field applicability and test speed.

(4) EMATs-based ultrasonics

Electromagnetic acoustic transducers (EMATs) are devices with which ultrasonic waves can be generated and detected on metals in a non-contact manner. It is achieved by a flat coil inducing a dynamic current in the rail surface, where a strong static magnetic field is provided by a permanent magnet or electromagnet. The electromagnetic energy can be transferred to mechanical energy and vice versa via an air gap of a few millimeters. Similar to laser-based ultrasonics, EMATs-based techniques could utilize various ultrasonic wave modes to meet a wide range of applications (Hirao and Ogi 2003). The commercial hi-rail inspection vehicle carrying an EMAT system is able to inspect the whole rail section at speeds up to 15 km/h (Chabhaz et al. 2000). However, this technique in principle cannot detect any defects less than 2 mm deep. Further research is in progress to improve the lift-off tolerance using EMATs skimming over structural surface (Petcher et al. 2014).

2.2.4 Electromagnetic Techniques

(1) Eddy current

Eddy current technique centers on electromagnetic induction, and is good at detecting surface or near-surface defects of rail head (Thomas et al. 2000, 2007). It comprises one exciting and one sensing coil, and the rail becomes a part of the circuit. Using an alternating current, the exciting coil generates a magnetic field near the surface of rail head, and induces eddy current below. The presence of defects would disturb the circumferential eddy current distributions, and cause fluctuations in the secondary magnetic field, which will give rise to changes in the impedance. It has been reported that high-speed rail surface inspection up to 100 km/h may be achievable guaranteed by eddy current based systems. Unfortunately, the sensors require a close distance of less than 2 mm from inspected surface to work, and are sensitive to the lift-off variation, which needs special guidance and adjustment.

(2) Alternating current field measurement

Alternating current field measurement (ACFM) is also an advanced electromagnetic technique for inspecting surface or near surface defects of rail head (Papaelias et al. 2009; Rowshandel et al. 2011). Based on the principle that an alternating current can be induced to flow in a thin skin near the surface of conductive material, a remote uniform current is introduced into the structural area detected and a magnetic field sensor is used to monitor the surface magnetic field variations. If cracks or other surface defects are present, the uniform electrical current would be disturbed. This technique is unaffected by the overall geometry of detected structure, and capable of detecting RCF-induced surface defects of less than 2 mm in depth. ACFM probes can accept a maximum operating lift-off of 5 mm. And ACFM arrays incorporate field inducers in various directions in order to detect potential defects in variable orientations. The main disadvantage of this technique is also its sensitivity to lift-off variations. Although the inspection speed of this technique has been reported to be 48 km/h, the quality of signal obtained is affected by lift-off variations.

2.2.5 Magnetic Induction Technique

For magnetic induction technique, permanent magnets or DC electromagnets are used to generate a strong magnetic field normal to the rail head, which essentially forms part of an electrical circuit. Sensing coils are then positioned at a constant distance from the rail surface to inspect any changes in the magnetic field (Fitzgerald 1995; Papaelias et al. 2008). When a near-surface or surface transverse defect is present, the current will travel around the defect, and hence magnetic distortion and flux leakage will be detected. This technique is also suitable for the detection of near surface or surface transverse defects, but deeper internal cracks

and rail foot defects which are too far away from the sensing coils or parallel to magnetic flux lines could not be successfully detected. It could achieve a maximum inspection speed of 35 km/h, and is regarded as complementary technique to ultrasonic inspection method (INNOTRACK 2008).

2.3 AE Technique and Its Applications

The AE technique identifies structural defects by utilizing ultrasonic waves released during degradation processes, such as crack initiation and propagation. In view of its successful applications in crack detection of roller bearings and other structures, it is of interest to apply AE technique for real-time crack monitoring of rail tracks. The AE technique and its relevant applications are reviewed and presented in this section.

2.3.1 Introduction to AE Technique

AE refers to the generation of transient stress waves produced by the sudden release of elastic strain energy within a material (Burnett 2011; Kishi et al. 2000; Miller et al. 2005). Sources of AE vary from natural events like earthquakes and rock bursts to structural behaviors such as plastic deformation, crack initiation and propagation, fracture, impact, friction and others. AE signals are ultrasonic waves with frequencies typically ranging from 20 kHz to 1 MHz. They contain valuable information of microstructural changes, which are related to discontinuities and defects in the material, and therefore can be used to detect defects in structures. AE technique has been successfully applied for structural integrity assessment of pressure vessels, composite materials, bridges and for condition monitoring of roller bearings, metal cutting, milling, grinding and others. (Al Jumaili et al. 2014; Ono 2007; Pandya et al. 2013; Schumacher et al. 2011).

Figure 2.10 presents the schematic of typical AE detection process. The sensor employed to collect AE signals is able to identify motions in the order of picometers. Since the AE signals are very weak, a preamplifier is connected right after the AE sensor to minimize the noise interference and prevent the signal loss (Huang et al. 1998). Then, the signals pass through an analog or digital filter to denoise. After that, the AE signals will be acquired and analyzed for damage detection.

Although AE technique makes use of ultrasonic waves, it is different from conventional ultrasonics in two ways. The first difference is the source of the signal. In conventional ultrasonics, an ultrasound input generated externally is required for transmission through the structure examined. In contrast, in AE technique, ultrasonic waves are released within the structure itself as a result of plastic deformation, crack propagation and other processes resulting in microstructural changes. Without the need of an external ultrasonic input, AE technique is thus regarded as a passive

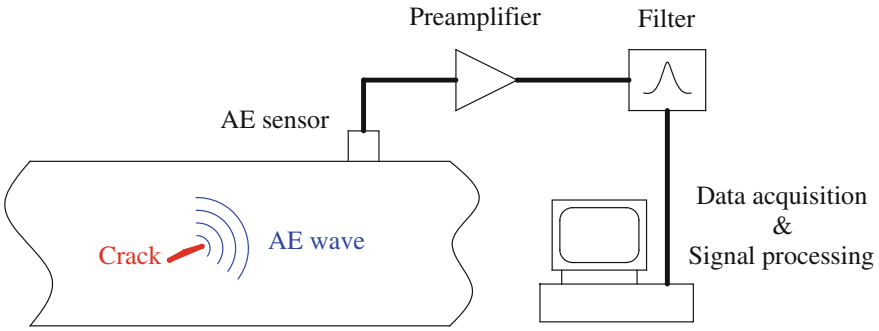

Fig. 2.10 Schematic of typical AE detection process

NDT. AE measurement can be made in real time when the host structure is in service, where normal operating load levels are sufficient to cause the emission of acoustic signals from defect sites.

The second difference pertains to the physical principle of defect detection. Conventional ultrasonics relies fully on the changes of wave propagation features, e.g. attenuation, reflection and dispersion, due to the presence of defects in the structure. AE technique however relies on the detection of elastic stress waves produced by degradation processes in the host material. For localization of defects, the wave propagation features need to be also taken into account in the analyses. AE technique is generally less influenced by the structural geometry of the host compared to its ultrasonic counterparts.

As the initiation and growth of defects could be directly monitored, the AE signal analyzed with advanced signal processing algorithms could provide an immediate diagnosis of the integrity of the structure at early stages of damage. More significantly, using AE technique it is possible to distinguish crack growth from stagnant ones automatically.

A summary of the advantages and disadvantages of AE technique is given in Table 2.3. Compared with other ultrasonic NDTs, AE technique is generally more sensitive to crack initiation and propagation, less influenced by the geometry of the

Table 2.3 Advantages and disadvantages of AE technique

Advantages
(1) No need of artificial input
(2) High sensitivity, which helps to identify defects at early stage
(3) Fast test process and real-time prediction
(4) In-service monitoring, which does not influence normal operation of structure inspected
(5) Less influenced by the structural geometry
(6) Defect detection possible over long distances
Disadvantages
(1) Large amount of data
(2) Low signal-to-noise ratio
(3) Difficulty in quantification of defect size

structure and more capable of long-distance detection of cracks. However, the low signal-to-noise ratio (SNR) of AE acquired in certain environments (e.g. field measurements) would require the use of advanced noise cancellation and signal processing algorithms to extract useful information. Further, it is also a challenge to obtain a quantitative assessment of size of the defect, highlighting the need for more research to advance this method of damage detection.

2.3.2 *Characterization of AE Waves*

AE waves generated by different processes (corresponding to different mechanisms) are likely to have different features. Characterization of the various features is important to be able to meaningfully distinguish and identify the sources of AE waves as well as for signal extraction in noisy raw data. The raw AE signal obtained from field measurements is a complex combination of waves contributed by various processes such as crack initiation, propagation and wheel-rail interaction, embedded within a noisy environment. It is therefore important to understand their respective characteristics in order to be able to identify the signatures as associated with each AE source.

AE waves are typically analyzed from the aspects of waveform parameters, frequency components, and time-frequency and non-stationary characteristics. These characteristics will be introduced below.

(1) Waveform parameters in the time domain

Waveform parameters of AE signal in the time domain typically include hits, counts, amplitude, duration, energy, root mean square (RMS), as illustrated in Table 2.4 and Fig. 2.11. It should be noted that amplitude, duration, and energy are generally consistent with each other, that is, a high energy usually corresponds to a large amplitude and a long duration. Because of the potentially large volume of data, which could accumulate over time, AE signals are normally recorded in the trigger mode. An acoustic wave acquired will be considered as an AE hit only when certain criteria, e.g. amplitude threshold, peak definition time (PDT), hit definition time (HDT) and hit lockout time (HLT), are satisfied. The thresholds for these criteria need to be pre-determined for each application taking into consideration the variabilities in the signal strength and operating environment of different situations (Physical Acoustics Corporation 2007).

Conventionally, parametric analysis of the AE waveform is the main approach used to detect the existence and extent of defects due to its simplicity and ease of realization. Significant efforts have been made to establish the relationships between these parameters and the associated AE activities, which are used to develop a variety of defect diagnosis methods (Roberts and Talebzadeh 2003b; Yu et al. 2011). However, parametric analysis has its limitations. For instance, the AE count rate is significantly affected by the frequency band of interest of the AE signal to be

Table 2.4 Terminology of AE waves

Terminology	Interpretation
Hits	Number of times the envelope of signal crosses the detection threshold
Counts	Number of times the signal crosses the detection threshold
Amplitude	Highest voltage in the AE waveform of one hit, in dB scale
Duration	Time for every hit, from fist to last threshold crossing
Energy	Time integral of the absolute signal voltage for every hit
RMS	Root mean square voltage during the timeframe of hit, referred to the input of signal processing board. Normally used for continuous AE monitoring

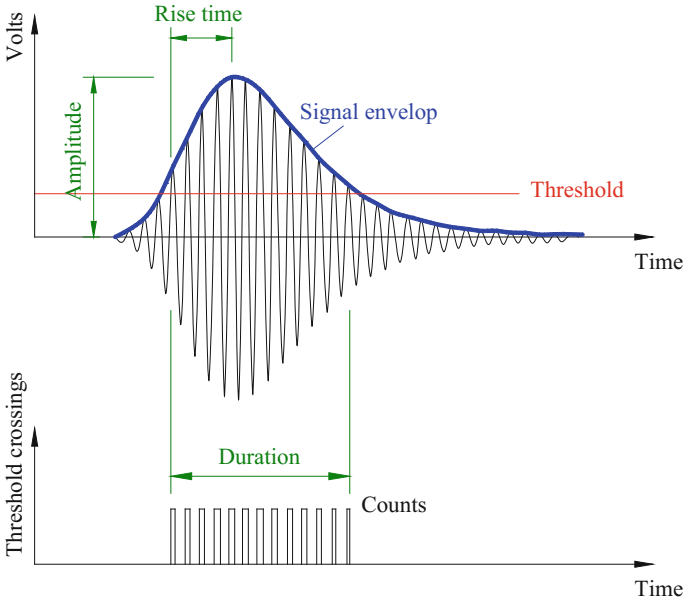

Fig. 2.11 Schemetic of definitions in an AE wave

acquired; the choice of the amplitude threshold of the AE signal depends on the operator's experience and it is not possible to prescribe a fixed value due to the great variation of loading conditions and operational noise, especially in field applications like rail track monitoring.

Overall, parametric analysis in the time domain could give a gross or general evaluation of the AE signal, but not provide the variety of details needed to characterize the AE wave fully (Zhang et al. 2015a).

(2) Frequency, time-frequency and non-stationary characteristics

With improvements in the performance of AE hardware and signal processing technologies, wideband AE transducers are now widely used to collect AE

waveforms with high fidelity, allowing advanced analysis of waveform in the frequency, time-frequency and other domains to be carried out to achieve more efficient damage detection algorithms. For practical applications in rail tracks, analyses based on these frequency characteristics are more reliable than the waveform parameters in the time domain, which unfortunately may vary dramatically as a result of the changes in the loading conditions. AE waves generated by different processes are normally expected to comprise different frequency components.

AE waves are non-stationary signals, i.e. their power spectra change with time. Time-frequency analysis is able to reveal more clearly the frequency components and non-stationary characteristics of AE waves in both time and frequency domains. Such time-frequency characteristics further help to identify the existence of structural degradations even in noisy environments and could be used to analyze the dispersion and scatter of AE waves propagating in complex structures. Many advanced signal processing algorithms have been proposed for the time-frequency analysis of AE waves, including short-time Fourier transform (STFT), wavelet transform (WT) (Ni and Iwamoto 2002), wavelet packet transform (WPT) (Khamedi et al. 2010) and Hilbert-Huang transform (HHT) (Lin and Chu 2012). Also, through non-stationary signal processing algorithms, such as fractal dimension (Biancolini et al. 2006), approximate entropy (ApEn) (Lin and Chu 2011) and correlation dimension (CD) (Rolo Naranjo and Montesino Otero 2005), the non-stationarity of AE signals could be described in the time and other domains.

With the use of appropriate signal processing algorithms, the transient disturbances in AE signals produced by structural defects could be efficiently distinguished from background noise, and the mechanisms corresponding to various AE phenomena could be understood deeply. Some applications of these characteristics will be given in the next section.

2.3.3 Relevant Applications of AE Technique

As a versatile NDT approach, the AE technique has been widely applied for defect detection in mechanical, aerospace and civil engineering materials and structures. Some relevant studies are reviewed below.

(1) Steel materials

AE monitoring of fatigue crack growth in metals has been investigated since the 1960s. Direct correlations were obtained between the AE count rate or energy rate and the applied stress intensity factor range or crack growth rate for various specimens subjected to laboratory fatigue loading, where compact tension specimens (Lindley et al. 1978; Moorthy et al. 1994; Morton et al. 1973), bending specimens (Sinclair et al. 1977; Zain et al. 2010), tensile specimens (Kohn et al. 1992; Murav'ev et al. 2002) and specially designed steel and welded steel T-section

girder specimens (Roberts and Talebzadeh 2003a) were used. The AE data were successfully implemented for crack size estimation and fatigue life prediction (Roberts and Talebzadeh 2003b; Yu et al. 2011).

On the other hand, the mechanisms behind degradations in steel were studied in terms of their frequency, time-frequency and non-stationary characteristics of AE waves. Through fast Fourier transform (FFT), Chaswal et al. (2005) found similar frequency behavior of AE signals from the threshold and Paris regimes of aged 9Cr-1Mo steel samples, which validated that the basic fatigue crack growth mechanism in both regimes is transgranular quasi-cleavage. Biancolini et al. (2006) suggested that the fractal dimension of AE signals could be used as an indicator of nucleation and crack propagation in steel, allowing the identification of the initiation of crack with a large advance. Khamedi et al. (2010) related different frequency ranges to the various micromechanisms of failure in dual-phase steels, i.e. ferrite-martensite interface decohesion, ferrite deformation and martensite-phase fracture, through wavelet packet analysis. Asamene and Sundaresan (2012) distinguished between AE signals arising from the friction of two flat steel surfaces and those from fatigue crack growth in steel through wavelet analysis. The frequency components were found to increase with surface roughness and sliding velocity. Piotrkowski et al. (2009) reported the evaluation of different corrosion levels of galvanized steel through wavelet power, entropy and bispectrum analysis of AE waves.

(2) Roller bearings

AE technique has been used for condition monitoring of roller bearings for decades. Relevant research is still conducted to achieve a more accurate defect identification and size quantification. Li and Li (1995) successfully demonstrated AE signal processing and pattern recognition algorithms to detect localized defects in the outer race and rollers of the bearing. Recently, Al-Dossary et al. (2009) reported that the AE energy level could provide indication of the severity of both outer and inner race defects on a radially loaded bearing, however, a correlation between the duration and amplitude of AE bursts and geometrical size of defects was obtained successfully only for the outer race. Widodo et al. (2009) performed principal component analysis (PCA) to extract valuable defect features, and utilized the multi-class relevance vector machine (RVM) to classify different types of defects, including outer and inner race defects. Promising results showed the potential of multi-class RVM proposed in fault diagnosis of low speed roller bearings. Subsequently, He and Zhang (2012) introduced approximate entropy (ApEn) analysis for AE measurements, which was demonstrated to be an effective feature parameter of AE signal in damage detection of rolling element bearings. Additionally, by means of time-frequency approach (HHT) and data mining tool (asymmetric proximity function with K nearest neighbor), Pandya et al. (2013) identified and classified AE signals related to healthy bearing, bearing with outer race, inner race, ball and combined defect. Since the contact mechanics of roller bearing is similar to that of wheel-rail interaction, these studies have great relevance and significance in the application of AE technique for rail condition monitoring.

(3) Other engineering structures

Besides roller bearings, AE technique has found applications in defect detection of various mechanical structures. Elforjani and Mba (2009) reported that AE technology could detect the initiation and growth of natural cracks on slow speed shafts. Lin and Chu (2012) extracted AE feature of natural fatigue cracks in rotating shafts using Hilbert-Huang transform (HHT) algorithm, which provides an energy-frequency-time distribution with adaptable precision. They (Lin and Chu 2011) also investigated AE signals from cracks in a steel tube loading test, and pointed out that AE time series containing many repetitive patterns have lower approximate entropy values relative to the background noise.

For aerospace structures, AE sensors can be attached in easily accessible areas to monitor remote damage prone sites. The shuttle wing leading edge impact detection system (WLEIDS) developed by NASA adopted AE technique. Impact events with a wide range of conditions were successfully detected and located on both the leading edge as well as the lower wing surface (Champaigne and Sumners 2005; Prosser et al. 2005).

AE technique is also increasingly applied to structural health monitoring in civil engineering (Grosse and Ohtsu 2008). Nair and Cai (2010) gave a brief review of the applications of AE in bridge health monitoring, and illustrated the statistical quantitative and intensity analyses of AE data for two case studies: a prestressed concrete slab-on-girder bridge and a steel bridge with a concrete deck. It was concluded that AE technique has a promising future into be an integral part of any structural health monitoring system in spite of the practical challenges expected in field measurements.

2.4 State-of-Art of Rail Condition Monitoring Using AE

To date, the research of rail condition monitoring using AE technique is mainly limited to laboratory studies. On the one hand, fatigue and static loading tests were carried out on rail steel specimens to investigate AE waves related to fatigue cracks. Bassim et al. (1994) derived the correlation between AE count rate and stress intensity factor based on fatigue test of four-point bending fatigue specimens. AE was demonstrated to be able to detect the onset of crack, corresponding to very low values of stress intensity factor range. Kostryzhev et al. (2013) characterized the frequency spectra of different AE waves related to plastic deformation, brittle crack growth and ductile crack growth in three-point bending fatigue specimens. Using AE data recorded during static tensile tests, Zhang et al. (2015b) established detection criteria to detect the safe status of rail based on the Chebyshev's inequality and the variation rate of AE hits.

On the other hand, several small-scale laboratory test rigs were set up to simulate wheel-rail interaction and to examine the performance of AE technique. Bruzelius and Mba (2004) validated the transmissibility of AE wave from the track to the AE

sensor, positioned on the wheel, by employing the pencil lead break (PLB) as AE sources. The AE activity observed, attributed to progressive wear of the track, demonstrated the potential of AE technique for rail defect detection. Based on the wheel speed and wave damping coefficients, Thakkar et al. (2010) derived a simplified analytical model to describe the expected AE waves of wheel-rail interaction recorded by a track-mounted sensor. By identifying AE peaks above the normal rolling background noise, they (Thakkar et al. 2013) developed methods to detect natural rail defects, simulated wheel defects and lateral rattling. The wheel test rig they used is shown in Fig. 2.12. Yılmazer et al. (2012) studied the wheel-rail rolling noise using a track-mounted sensor and a trolley running at a speed of 3 km/h. It was concluded that wheel-related rolling noise might not be a barrier for the crack detection. However, the noise level generated by such a slow and light trolley was too weak compared to that caused by a fast heavy train. Recently, by means of a track-mounted AE sensor, Zhang et al. (2015a) found that the operational noise resulting from the test rig at wheel speed above 78 km/h was extremely high, and reported that the defects, simulated by PLB sources, can be detected using the time-Shannon entropy of wavelet coefficients. The wheel-rail test rig they used is displayed in Fig. 2.13. They (Zhang et al. 2014) also studied the features of simulated AE sources with different propagation distances, types and depths on a short segment of steel rail (30 cm).

Additionally, Thakkar et al. (2006) and Bollas et al. (2010) reported AE signals of wheel-rail interaction recorded during field tests with trains passing at speeds up to 40 km/h, in which sensors were attached to the rail base and rail web, respectively. AE waves induced by the normal wheel-rail interaction showed high energies and should be considered as strong background noise for both of wheel flat detection and rail crack monitoring. Liu et al. (2015b) proposed a pattern recognition method to identify the damage state of rail turnouts by making use of AE signals acquired under field environment.

Overall, AE technique has been demonstrated to be a promising and effective tool for rail condition monitoring. Many studies have shown that AE technique is well suited for inspecting rail cracks, rail corrugations, rail wears and wheel flats.

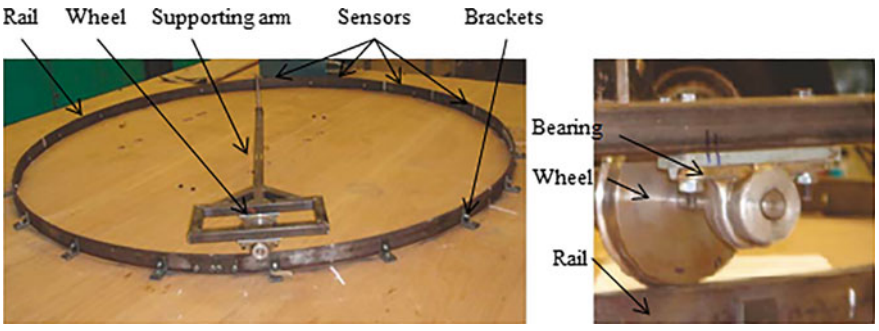

Fig. 2.12 Wheel-rail test rig of reference (Thakkar et al. 2010)

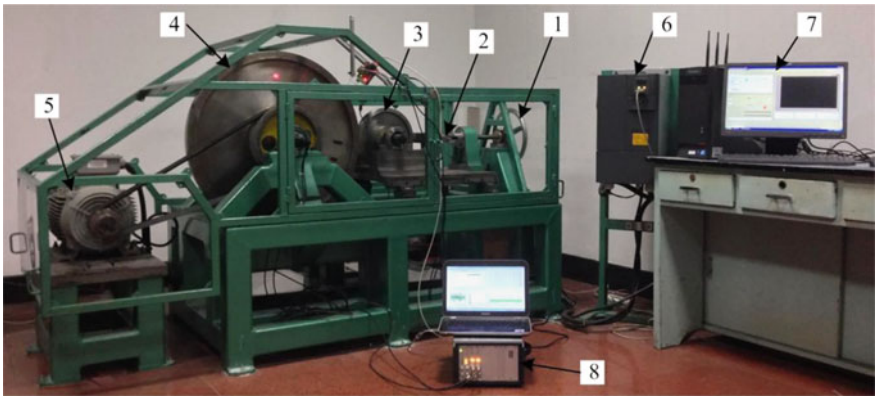

Fig. 2.13 Wheel-rail test rig of the reference (Zhang et al. 2015a) (*Note* 1. Pressure device; 2. Pressure sensor; 3. Simulated wheel; 4. Simulated rail where AE sensor attached; 5. Electric motor; 6. Frequency converter; 7. Control console; 8. AE data acquisition equipment.)

However, for the use of AE technique for rail crack detection and monitoring, more experimental work needs to be performed on actual rail tracks considering the fact that the actual rail profile has a strong impact on the propagation features of the AE waves. More significantly, the actual rail crack conditions in the field are much more complicated than those in the laboratory fatigue tests, in addition to the high operational noise which could markedly reduce the performance of the crack detection algorithms developed based only on experimental test rigs carried out in the laboratory. In view of this, the work carried out in this thesis also includes field verification in addition to the series of studies conducted under controlled environment in the laboratory.

References

Al-Dossary, S., Hamzah, R., & Mba, D. (2009). Observations of changes in acoustic emission waveform for varying seeded defect sizes in a rolling element bearing. *Applied Acoustics, 70* (1), 58–81.

Al Jumaili, S. K., Holford, K. M., Eaton, M. J., McCrory, J. P., Pearson, M. R., & Pullin, R. (2014). Classification of acoustic emission data from buckling test of carbon fibre panel using unsupervised clustering techniques. *Structural Health Monitoring, 14,* 241–251.

ARTC. (2006). *Rail defects handbook: Some rail defects, their characteristics, causes and control*. Australia: Australian Rail Track Corporation Ltd.

Asamene, K., & Sundaresan, M. (2012). Analysis of experimentally generated friction related acoustic emission signals. *Wear, 296*(1), 607–618.

Bartoli, I., Lanza di Scalea, F., Fateh, M., & Viola, E. (2005). Modeling guided wave propagation with application to the long-range defect detection in railroad tracks. *NDT and E International, 38*(5), 325–334.

Bassim, M. N., Lawrence, S. S., & Liu, C. D. (1994). Detection of the onset of fatigue crack growth in rail steels using acoustic emission. *Engineering Fracture Mechanics, 47*(2), 207–214.

Biancolini, M., Brutti, C., Paparo, G., & Zanini, A. (2006). Fatigue cracks nucleation on steel, acoustic emission and fractal analysis. *International Journal of Fatigue, 28*(12), 1820–1825.

Bollas, K., Papasalouros, D., Kourousis, D., & Anastasopoulos, A. (2010). Acoustic emission inspection of rail wheels. *Journal of Acoustic Emission, 28,* 215–228.

Bruzelius, K., & Mba, D. (2004). An initial investigation on the potential applicability of acoustic emission to rail track fault detection. *NDT and E International, 37*(7), 507–516.

Burnett, J. K. (2011). *Theory and uses of acoustic emissions*. New York: Nova Science Publishers.

Cannon, D. F., Edel, K. O., Grassie, S. L., & Sawley, K. (2003). Rail defects: An overview. *Fatigue and Fracture of Engineering Materials and Structures, 26*(10), 865–886.

Cantero, D., & Basu, B. (2014). Railway infrastructure damage detection using wavelet transformed acceleration response of traversing vehicle. *Structural Control and Health Monitoring, 22,* 62–70.

Chabhaz, A., Brassard, M., & Pelletier, A. (2000). Mobile inspection system for rail integrity assessment. In *The 15th World Conference of Non-destructive Testing*, Roma, Italy.

Champaigne, K. D., & Sumners, J. (2005). Wireless impact and leak detection and location systems for the ISS and shuttle wing leading edge. In *2005 IEEE Aerospace Conference*. Big Sky, MT, USA, 1–8.

Chaswal, V., Sasikala, G., Ray, S. K., Mannan, S. L., & Raj, B. (2005). Fatigue crack growth mechanism in aged 9Cr–1Mo steel: Threshold and Paris regimes. *Materials Science and Engineering A, 395*(1), 251–264.

Clark, R. (2004). Rail flaw detection: Overview and needs for future developments. *NDT and E International, 37*(2), 111–118.

Clark, R., Singh, S., & Haist, C. (2002). Ultrasonic characterisation of defects in rails. *Insight—Non-destructive Testing and Condition Monitoring, 44*(6), 341–347.

Czichos, H., Saito, T., & Smith, L. (2006). *Springer handbook of materials measurement methods*. Würzburg, Germany: Springer.

De Ruvo, P., De Ruvo, G., Distante, A., Nitti, M., Stella, E., & Marino, F. (2008). A visual inspection system for rail detection and tracking in real time railway maintenance. *The Open Cybernetics & Systemics Journal, 2*.

Ekberg, A., & Kabo, E. (2005). Fatigue of railway wheels and rails under rolling contact and thermal loading-an overview. *Wear, 258*(7–8), 1288–1300.

Elforjani, M., & Mba, D. (2009). Detecting natural crack initiation and growth in slow speed shafts with the acoustic emission technology. *Engineering Failure Analysis, 16*(7), 2121–2129.

Esveld, C. (2001). *Modern railway track* (2nd ed.). Zaltbommel: MRT-Productions.

Fan, Y., Dixon, S., Edwards, R. S., & Jian, X. (2007). Ultrasonic surface wave propagation and interaction with surface defects on rail track head. *NDT and E International, 40*(6), 471–477.

Fitzgerald, C. S. (1995). Inspection for rail defects by magnetic induction. In *Proceedings of SPIE 2458, Nondestructive Evaluation of Aging Infrastructure*, 40–44.

Grosse, C. U., & Ohtsu, M. (2008). *Acoustic emission testing, basics for research—Applications in civil engineering*. Heidelberg: Springer.

He, Y. Y., & Zhang, X. M. (2012). Approximate entropy analysis of the acoustic emission from defects in rolling element bearings. *Journal of Vibration and Acoustics, 134*(6), 061012.

Hirao, M., & Ogi, H. (2003). *EMATs for science and industry: Noncontacting ultrasonic measurements*. Springer.

Huang, M., Jiang, L., Liaw, P. K., Brooks, C. R., Seeley, R., & Klarstrom, D. L. (1998). Using acoustic emission in fatigue and fracture materials research. *JOM Journal of the Minerals Metals and Materials Society, 50*(11), 1–14.

INNOTRACK. (2008). *Rail inspection technologies* (TIP5-CT-2006-031415).

Jeong, D. Y., & Orringer, O. (1989). Fatigue crack growth of surface cracks in the rail web. *Theoretical and Applied Fracture Mechanics, 12*(1), 45–58.

Kenderian, S., Djordjevic, B. B., Cerniglia, D., & Garcia, G. (2006). Dynamic railroad inspection using the laser-air hybrid ultrasonic technique. *Insight—Non-destructive Testing and Condition Monitoring, 48*(6), 336–341.

Khamedi, R., Fallahi, A., & Refahi Oskouei, A. (2010). Effect of martensite phase volume fraction on acoustic emission signals using wavelet packet analysis during tensile loading of dual phase steels. *Materials and Design, 31*(6), 2752–2759.

Kishi, T., Ohtsu, M., & Yuyama, S. (2000). *Acoustic emission—Beyond the millennium*. Oxford: Elsevier.

Kohn, D. H., Ducheyne, P., & Awerbuch, J. (1992). Acoustic emission during fatigue of Ti-6Al-4 V: Incipient fatigue crack detection limits and generalized data analysis methodology. *Journal of Materials Science, 27*(12), 3133–3142.

Kostryzhev, A. G., Davis, C. L., & Roberts, C. (2013). Detection of crack growth in rail steel using acoustic emission. *Ironmaking and Steelmaking, 40*(2), 98–102.

Li, C. J., & Li, S. Y. (1995). Acoustic emission analysis for bearing condition monitoring. *Wear, 185*(1), 67–74.

Li, Q. Y., & Ren, S. W. (2012). A real-time visual inspection system for discrete surface defects of rail heads. *IEEE Transactions on Instrumentation and Measurement, 61*(8), 2189–2199.

Lin, L., & Chu, F. (2011). Approximate entropy as acoustic emission feature parametric data for crack detection. *Nondestructive Testing and Evaluation, 26*(02), 119–128.

Lin, L., & Chu, F. (2012). HHT-based AE characteristics of natural fatigue cracks in rotating shafts. *Mechanical Systems and Signal Processing, 26,* 181–189.

Lindley, T. C., Palmer, I. G., & Richards, C. E. (1978). Acoustic emission monitoring of fatigue crack growth. *Materials Science and Engineering, 32*(1), 1–15.

Liu, X. Z., Ni, Y. Q., Wu, W. L., Pei, Y. F., Hou, Y. H., & Qin, D. Y. (2015b). AET-based Pattern Recognition Technique for Rail Defect Detection. In *Proceedings of the 10th International Workshop on Structural Health Monitoring*. CA, USA: Stanford, 2021–2027.

Mariani, S., Nguyen, T., Phillips, R. R., Kijanka, P., Lanza di Scalea, F., Staszewski, W. J., et al. (2013). Noncontact ultrasonic guided wave inspection of rails. *Structural Health Monitoring, 12*(5–6), 539–548.

Miller, R. K., Moore, P. O., & Hill, E. V. K. (2005). *Nondestructive testing handbook vol. 6, acoustic emission testing* (3rd ed.). Columbus: American Society for Nondestructive Testing.

Molodova, M., Li, Z., Núñez, A., & Dollevoet, R. (2014). Automatic detection of squats in railway infrastructure. *IEEE Transactions on Intelligent Transportation Systems, PP*(99), 1–11.

Moorthy, V., Jayakumar, T., & Baldev, R. (1994). Acoustic emission behaviour during stage II fatigue crack growth in an AISI type 316 austenitic stainless steel. *Bulletin of Materials Science, 17*(6), 699–715.

Morton, T. M., Harrington, R. M., & Bjeletich, J. G. (1973). Acoustic emissions of fatigue crack growth. *Engineering Fracture Mechanics, 5*(3), 691–697.

Murav'ev, V. V., Murav'ev, M. V., & Bekher, S. A. (2002). Effect of loading conditions on informative parameters and signal spectra of acoustic emission in samples of carbon steels. *Russian Journal of Nondestructive Testing, 38*(7), 483–492.

Nair, A., & Cai, C. S. (2010). Acoustic emission monitoring of bridges: Review and case studies. *Engineering Structures, 32*(6), 1704–1714.

Ni, Q. Q., & Iwamoto, M. (2002). Wavelet transform of acoustic emission signals in failure of model composites. *Engineering Fracture Mechanics, 69*(6), 717–728.

Ono, K. (2007). Structural integrity evaluation using acoustic emission. *Journal of Acoustic Emission, 25,* 1–20.

Pandya, D. H., Upadhyay, S. H., & Harsha, S. P. (2013). Fault diagnosis of rolling element bearing with intrinsic mode function of acoustic emission data using APF-KNN. *Expert Systems with Applications, 40*(10), 4137–4145.

Papaelias, M. P., Lugg, M. C., Roberts, C., & Davis, C. L. (2009). High-speed inspection of rails using ACFM techniques. *NDT and E International, 42*(4), 328–335.

Papaelias, M. P., Roberts, C., & Davis, C. L. (2008). A review on non-destructive evaluation of rails: State-of-the-art and future development. *Proceedings of the Institution of Mechanical Engineers, Part F: Journal of Rail and Rapid Transit, 222*(4), 367–384.

Pearson, G. (2002). Rail testing in the Wessex region. *Insight—Non-destructive Testing and Condition Monitoring, 44*(6), 375–378.

Petcher, P. A., Potter, M. D. G., & Dixon, S. (2014). A new electromagnetic acoustic transducer (EMAT) design for operation on rail. *NDT and E International, 65,* 1–7.

Physical Acoustics Corporation. (2007). *PCI-2 based AE system user's manual*.

Piotrkowski, R., Castro, E., & Gallego, A. (2009). Wavelet power, entropy and bispectrum applied to AE signals for damage identification and evaluation of corroded galvanized steel. *Mechanical Systems and Signal Processing, 23*(2), 432–445.

Prosser, W., Madaras, E., Studor, G., & Gorman, M. (2005). Acoustic emission detection of impact damage on space shuttle structures. *Journal of Acoustic Emission, 23,* 37–46.

Remennikov, A. M., & Kaewunruen, S. (2008). A review of loading conditions for railway track structures due to train and track vertical interaction. *Structural Control and Health Monitoring, 15*(2), 207–234.

Roberts, T. M., & Talebzadeh, M. (2003a). Acoustic emission monitoring of fatigue crack propagation. *Journal of Constructional Steel Research, 59*(6), 695–712.

Roberts, T. M., & Talebzadeh, M. (2003b). Fatigue life prediction based on crack propagation and acoustic emission count rates. *Journal of Constructional Steel Research, 59*(6), 679–694.

Rolo Naranjo, A., & Montesino Otero, M. E. (2005). A method for the correlation dimension estimation for on-line condition monitoring of large rotating machinery. *Mechanical Systems and Signal Processing, 19*(5), 939–954.

Rose, J. L., Avioli, M. J., Mudge, P., & Sanderson, R. (2004). Guided wave inspection potential of defects in rail. *NDT and E International, 37*(2), 153–161.

Rowshandel, H., Nicholson, G. L., Davis, C. L., & Roberts, C. (2011). A robotic approach for NDT of RCF cracks in rails using an ACFM sensor. *Insight—Non-destructive Testing and Condition Monitoring, 53*(7), 368–376.

Schumacher, T., Higgins, C. C., & Lovejoy, S. C. (2011). Estimating operating load conditions on reinforced concrete highway bridges with b-value analysis from acoustic emission monitoring. *Structural Health Monitoring, 10*(1), 17–32.

Scruby, C. B., & Drain, L. E. (1990). *Laser ultrasonics techniques and applications*. New York: CRC Press.

Sinclair, A. C. E., Connors, D. C., & Formby, C. L. (1977). Acoustic emission analysis during fatigue crack growth in steel. *Materials Science and Engineering, 28*(2), 263–273.

Thakkar, N. A. (2009). *Monitoring of Rail/Wheel Interaction Using Acoustic Emission.* (Ph.D.). UK: Heriot-Watt University.

Thakkar, N. A., Steel, J. A., & Reuben, R. L. (2010). Rail-wheel interaction monitoring using acoustic emission: A laboratory study of normal rolling signals with natural rail defects. *Mechanical Systems and Signal Processing, 24*(1), 256–266.

Thakkar, N. A., Steel, J. A., & Reuben, R. L. (2013). A laboratory study of rail-wheel interaction monitoring using acoustic emission: Effect of rolling conditions with and without lateral rattling. *Proceedings of the Institution of Mechanical Engineers, Part F: Journal of Rail and Rapid Transit, 227*(2), 161–175.

Thakkar, N. A., Steel, J. A., Reuben, R., Knabe, G., Dixon, D., & Shanks, R. (2006). Monitoring of rail-wheel interaction using acoustic emission (AE). *Advanced Materials Research, 13,* 161–168.

Thomas, H. M., Heckel, T., & Hanspach, G. (2007). Advantage of a combined ultrasonic and eddy current examination for railway inspection trains. *Insight—Non-destructive Testing and Condition Monitoring, 49*(6), 341–344.

Thomas, H. M., Junger, M., Hintze, H., Krull, R., & Rühe, S. (2000). Pioneering inspection of railroad rails with eddy currents. In *The 15th World Conference on Non-destructive Testing*. Rome, Italy.

UIC. (2002). *Rail defects* (4th ed.). Paris: International Union of Railways.

Vidaud, M., & Zwanenburg, W. J. (2009). Current situation on rolling contact fatigue–a rail wear phenomenon. In *9th Swiss Transport Research Conference*, 9–11.

Widodo, A., Kim, E. Y., Son, J. D., Yang, B. S., Tan, A. C. C., Gu, D. S., et al. (2009). Fault diagnosis of low speed bearing based on relevance vector machine and support vector machine. *Expert Systems with Applications, 36*(3), 7252–7261.

Yılmazer, P., Amini, A., & Papaelias, M. (2012). The structural health condition monitoring of rail steel using acoustic emission techniques. In *51st Annual Conference of the British Institute of Non-destructive Testing 2012 (NDT 2012)*. Northamptonshire, UK, 51–62.

Yu, J. G., Ziehl, P., Zrate, B., & Caicedo, J. (2011). Prediction of fatigue crack growth in steel bridge components using acoustic emission. *Journal of Constructional Steel Research, 67*(8), 1254–1260.

Zain, M. S. M., Jamaludin, N., Sajuri, Z., Yusof, M. F. M., & Hanafi, Z. H. (2010). Acoustic emission study of fatigue crack growth in rail track material. In *National Conference in Mechanical Engineering Research and Postgraduate Studies (2nd NCMER)*, 82–90.

Zhang, X., Feng, N., Wang, Y., & Shen, Y. (2014). An analysis of the simulated acoustic emission sources with different propagation distances, types and depths for rail defect detection. *Applied Acoustics, 86,* 80–88.

Zhang, X., Feng, N., Wang, Y., & Shen, Y. (2015a). Acoustic emission detection of rail defect based on wavelet transform and Shannon entropy. *Journal of Sound and Vibration, 339,* 419–432.

Zhang, X., Feng, N., Zou, Z., Wang, Y., & Shen, Y. (2015b). An investigation on rail health monitoring using acoustic emission technique by tensile test. In *Proceedings of 2015 IEEE International Instrumentation and Measurement Technology Conference (I2MTC)*, 1046–1051.

Chapter 3
Propagation Features and Source Location

As highlighted in the previous chapter, research on rail crack monitoring using AE technique to date is limited to mainly laboratory studies, such as fatigue tests and small-scale test rigs. Little attention has been paid to the propagation features and source location of crack-induced AE waves in the real rail track as well as the influence of operational noise on robustness and reliability of the technique for crack detection under field environment, which are important considerations for implementation of rail crack monitoring in practice. In ultrasonic techniques, the irregular rail cross-section is treated as three parts: the head, web and foot (as shown in Fig. 2.1). This research is primarily focused on the detection of cracks in the rail head, which is one of the most vulnerable parts of the rail track (Esveld 2001). In view of this, this chapter will focus on the wave propagation features and crack location method in the rail head using PLB-simulated AE sources, and the noise cancellation method by taking into account the operational noise encountered in the field.

3.1 Introduction

Locating the AE source (i.e. crack) in rail head can be considered as a one-dimensional problem in a homogeneous material. Nonetheless, due to the complicated geometry of the track and high operational noise encountered in the field, it is not easy to determine precisely the arriving time and propagation velocity of AE wave. In particular, the AE waves propagating along the rail head should be treated as guided waves (Coccia et al. 2011), of which the key feature is velocity dispersion. The dispersion phenomena of AE wave, if not taken into consideration, would contribute errors in the source location results. There has been much research on AE source location in plate structures using the dispersive Lamb wave modes through modal analysis (Ciampa and Meo 2010; Hamstad et al. 2002; Holford et al. 2001). Zhang et al. (2014) studied the features of simulated AE sources with

D. Li, *Rail Crack Monitoring Using Acoustic Emission Technique*,
Springer Theses, https://doi.org/10.1007/978-981-10-8348-8_3

different propagation distances, types and depths in the rail web using a short rail segment of 30 cm. However, further study is needed for crack detection over long distances in rail head, where the Rayleigh-Lamb equation used would be invalid due to the complex shape of rail and where the frequency characteristics of crack-induced AE wave as well as operational noise are unknown.

There are two main approaches of AE source location: (1) time-of-arrival (TOA) method, which relies on the difference between arrival times of an AE event at two adjacent sensors, and (2) single sensor modal analysis location (SSMAL) method, which makes use of the time delay between two dispersive wave modes at one sensor for the analysis (Ernst and Dual 2014). When the wavelet transform (WT) is applied to analyze the dispersive wave modes (Jiao et al. 2008; Mikio et al. 2000), the SSMAL method can be conveniently named as wavelet transform-based modal analysis location (WTMAL) method. The WTMAL method is proposed in this work to locate rail head cracks for two reasons. First, AE waves exhibit obvious dispersion when they propagate along the rail head. Exploiting the wave dispersion phenomena, the WTMAL method is potentially more accurate than the TOA method. In TOA method, the wave velocity used is actually the average velocity of various dispersive wave modes, which introduce added variability to the computation. Second, when a wheel is too close to the sensor, the operational noise caused by wheel-rail interaction may obscure the crack-induced AE signal generated by other wheels. The WTMAL method requires only one sensor to determine the distance between AE source and sensor, and is thus less susceptible to the operational noise compared to the TOA method where two sensors are needed.

In this chapter, a crack location method and a noise cancellation method are proposed based on a series of field tests. Pencil lead break (PLB) was applied to simulate the AE of rail head cracks. Field tests were carried out to acquire the AE waves generated by PLBs at various source-sensor distances and the operational noise caused by passing trains, respectively. WT was first used to investigate the time-frequency characteristics of different AE sources and to gain an insight into the dispersion phenomena of AE waves propagating along the rail head. The TOA method and the WTMAL method were then applied to locate the AE sources (i.e. simulated cracks) for the PLB-induced AE signals with and without operational noise, respectively. The group velocities of the two prominent dispersive wave modes used were experimentally determined. For those AE signals inundated with operational noise, the Hilbert transform (HT)-based noise cancellation method was employed to improve the SNR. Finally, the results of source location and noise cancellation will be discussed. A flowchart of the proposed crack detection strategy, including data acquisition, AE source location and noise cancellation, is summarized in Fig. 3.1.

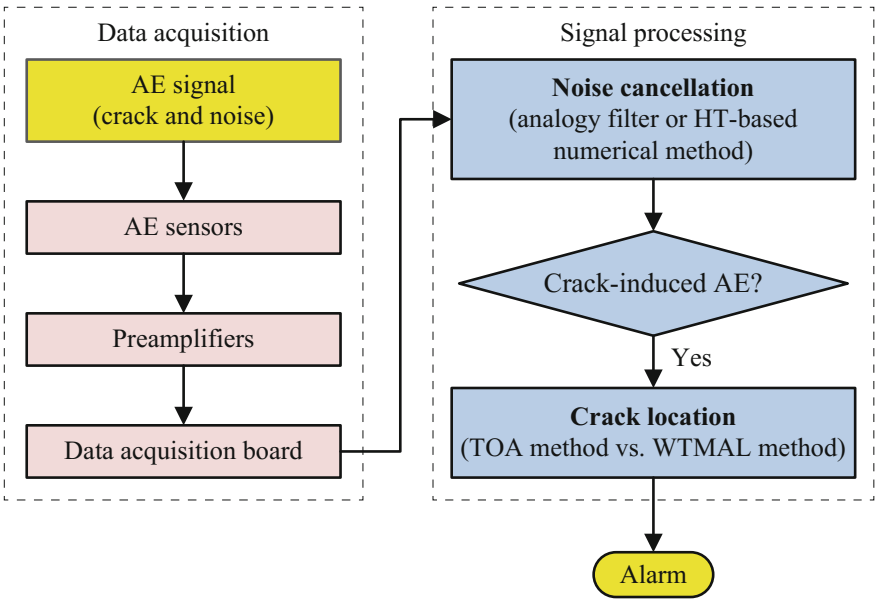

Fig. 3.1 Flowchart of the crack detection strategy proposed in this chapter

3.2 Experimental Procedure

As a preliminary quantitative study, the widely used PLB (Zhang et al. 2014, 2015a) was adopted to simulate the AE signals of rail cracks. PLB can produce uniform and stable AE sources, which have similar frequency components as the crack-induced AE waves in metallic material. In order to explore the propagation features and sources location of AE waves in the rail head, the PLB test was conducted to acquire the AE waves generated by PLBs at various source-sensor distances. In order to study the influence of operational noise on the AE source location and the noise cancellation method, the train pass-by test was done to record the operational noise caused by passing trains. Here, the two kinds of AE signals (i.e. PLB signals and noise) were combined to simulate the actual AE events of rail head cracks in a typical noisy environment. Such a way of signal synthesis with random phase angles is commonly adopted by researchers to simulate actual cases under limited experimental conditions (Audoin et al. 2006; Hamstad and O'Gallagher 2005). The experimental setup and data acquisition procedure are introduced in this section.

3.2.1 Pencil Lead Break (PLB)

PLB source, also named as Hsu-Nielsen source, was used to simulate crack-induced AE signals by carefully pressing and breaking lead tip against the surface of the structure. The fracture of brittle graphite lead assembled in a suitable fitting generated an elastic wave due to a sudden release of stress. According to the ASTM E976-10 (ASTM 2010), a mechanical pencil with 2H leads of 0.5 mm diameter (as shown in Fig. 3.2) is recommended to produce as the AE source in a reasonably repeatable way. The length of lead to be broken was 3 mm each time. A Nielsen shoe was utilized to ensure that the leads broke consistently at 30° angle. Generally, the lead break could register amplitudes of at least 80 dB referring to 1 μV at the sensor and a total system gain of 40 dB. PLB is widely used by researchers to check whether AE sensors are well contacted with structural surface, and to investigate the propagation features of acoustic wave in the object being monitored.

3.2.2 Field PLB Test

The PLB test was conducted on a rail track located in China during its non-operation period (i.e. when no train was running). The setup is shown in Fig. 3.2. The rail track was Chinese 60 kg/m U71Mn rail, the cross-section and material of which are similar to UIC 60 used worldwide. The rail track was supported by concrete sleepers and ballast. The distance between two rails was 1435 mm, and the distance between two adjacent sleepers was about 600 mm.

As shown in Fig. 3.2, the two AE sensors, numbered as S1 and S2, were installed at 30.0 m apart. The pencil leads were broken on the running surface of rail head at fourteen locations along the rail in order to record AE waves at various

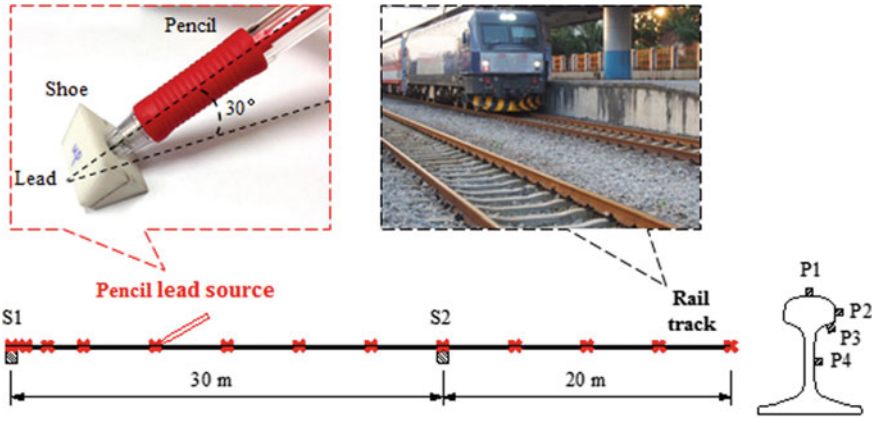

Fig. 3.2 Setup of PLB test

propagation (source-sensor) distances. These locations, measured from S1, were 0.0, 0.5, 1.0, 2.5, 5.0, 10.0, 15.0, 20.0, 25.0, 30.0, 35.0, 40.0, 45.0 and 50.0 m, as indicated by the symbol "x". Four different sensor mounting positions on the rail cross-section were tested: top of rail head (P1), field side of rail head (P2), underside of rail head (P3), and middle of rail web (P4). For each sensor mounting position, PLBs were carried out successively at all the locations. At each location, a series of ten PLBs were done.

The amplitudes of PLB-induced AE waves at the four different mounting positions, P1–P4, were compared. For example, after the AE waves propagated 20.0 m along the rail head, the average amplitudes recorded by S1 at P1–P4 were respectively 0.52, 0.29, 0.073, and 0.052 V. It can be concluded that the energy of AE waves arising from the rail head is mainly guided in the rail head when they propagate along the rail. Excluding the top of the rail head (P1), which is not practicable for continuous monitoring of operational railway, the field side of rail head (P2), which has less attenuation than the underside of rail head (P3) and the middle of rail web (P4), is thus the optimal position for sensors to collect AE waves. More importantly, the dispersion phenomena of AE waves in the rail head could be clearly observed by sensors at P2. If an AE source arose from the rail web or foot, the signals received by sensors at P2 would not contain any obvious dispersive wave modes. Thus, AE sensors are recommended to be mounted at P2 for the crack detection of rail head. The AE waves discussed in the following sections are all obtained by sensors mounted at P2.

3.2.3 Field Train Pass-by Test

The train pass-by test was carried out on the same rail track during its operation periods with trains operating in full service. The setup is shown in Fig. 3.3. Sensors were installed on the field side of rail head (P2) (as results from the PLB test showed P2 to be the optimal position for rail head crack detection). The operational noise was recorded during the passing of two trains: (1) a fully loaded passenger train with axial load of about 17,000 kg which ran at a speed of approximately 120 km/h and (2) an empty passenger train with axial load of about 12,000 kg which ran at a speed of approximately 80 km/h.

The energy of the operational noise depends significantly on the speed and axle load of the train. Figure 3.4a shows a 10-s segment of operational noise recorded continuously (by an AE sensor at P2) during the passing of a fully loaded passenger train. Figure 3.4b on the other hand shows a sample of AE wave recorded during the passing of an empty passenger train. Due to the higher train speed and axle load, the operational noise in Fig. 3.4a as indicated by the peak amplitude of about 1.86 V is much higher than that observed in Fig. 3.4b with peak amplitude of only about 0.57 V. To test the robustness of the proposed crack detection strategy, the higher operational noise (i.e. the worse condition) will be used in the analysis that follows.

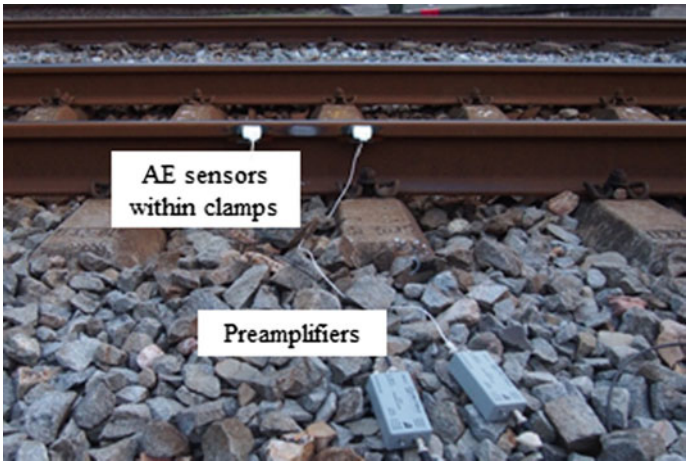

Fig. 3.3 Setup of train pass-by test

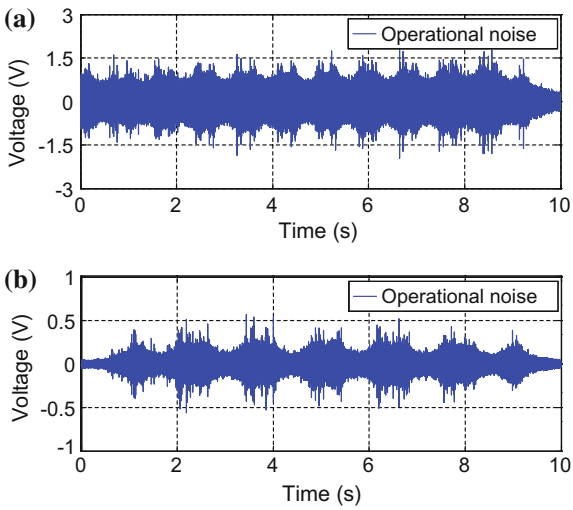

Fig. 3.4 Operational noise in train pass-by test: **a** a full loaded train and **b** an empty train

3.2.4 AE Data Acquisition

The AE signals were collected by a multi-channel Physical Acoustics (PAC) AE system. Micro80D sensors were employed, which are of small dimensions and hence could be installed on the rail head for crack detection with minimal intrusiveness. Micro80D sensor (Physical Acoustics Corporation 2016a) has a wide operating bandwidth of 175–900 kHz with a resonant frequency of approximately 325 kHz. It is a differential sensor designed to isolate the sensing terminals electrically from the cavity. This electrical isolation makes the sensor particularly useful

for applications where high background electrical noise is a concern. Besides, the sensor has a very high sensitivity, making it well-suited for structural health monitoring of large structures like storage tanks, pipelines, etc.

Adhesive couplant was applied to ensure good contact between the sensor and the rail surface. Magnetic clamps were utilized to fix them in place. AE signals acquired by the sensors were amplified via preamplifiers (PAC 2/4/6) and finally recorded by the data acquisition board. For all the tests, the gain of preamplifier was set to 40 dB (referring to 1 μV at the sensor), the sampling rate was 5 MHz, and the analog band-pass filter was 100–1000 kHz.

3.3 Time-Frequency Representation of AE Waves

AE waves are non-stationary signals whose power spectra change with time, therefore the time-frequency analysis is necessary in order to represent the frequency components of the AE waves and their variation with time. Wavelet analysis is the most powerful and commonly-used tool that has been applied to characterize AE signals in the time-frequency domain (Marec et al. 2008; Suzuki et al. 1996; Zhang et al. 2015a). Instead of discrete wavelet transform (DWT), continuous wavelet transform (CWT) is implemented in this study as it operates in more detailed scales, provides a more powerful multi-resolution capability, and performs better in noisy environments for singularity detection. The analysis is applied to only small segments of AE waves of interest to reduce computational work involved. The theory of CWT and the selection of the mother wavelet is briefly introduced in this section.

3.3.1 Continuous Wavelet Transform (CWT)

CWT is defined as the convolution of signal $x(t)$ to be analyzed and a series of wavelet functions $\psi_{a,b}(t)$, which are simply dilated and translated from a unique admissible mother wavelet $\psi(t)$ (Daubechies 1992; Teolis 1998).

$$WT(a,b) = \int_{-\infty}^{\infty} x(t)\psi_{a,b}^{*}(t)dt \tag{3.1}$$

where

$$\psi_{a,b}(t) = \frac{1}{\sqrt{a}}\psi\left(\frac{t-b}{a}\right) \quad (a,b \in R, \text{ and } a > 0) \tag{3.2}$$

Here, $(\cdot)^*$ denotes the complex conjugate, a is the scale parameter, b is the translation parameter, t is the time, and $WT(a,b)$ is the corresponding wavelet coefficient. The wavelet function $\psi_{a,b}(t)$ is centered at b with a spread proportional to a, and could be regarded as a window function in both of the time and frequency domains. During the transform, a series of $\psi_{a,b}(t)$ is generated according to variable values of a and b. By such an approach, time-frequency localization analysis is realized. The squared modulus of the wavelet coefficient $|WT(a,b)|^2$, also known as wavelet power (WP), represents the energy density of the signal at particular time and frequency scales. The local WP maxima are achieved at the dominant instantaneous frequencies with high energy concentration (Mallat 1999).

3.3.2 Optimal Mother Wavelet Selection

The choice of the mother wavelet has a significant influence on the results of WT. A suitable mother wavelet needs to be selected by taking into account the properties of both the wavelets (e.g. symmetry, orthogonality, and support size) and the AE waves of interest. The complex Morlet wavelet is adopted in this study as it provides excellent resolution in both of the time and frequency domains (Ciampa and Meo 2010; Niri and Salamone 2012; Teolis 1998). Its function and corresponding Fourier transform are, respectively,

$$\psi(t) = \frac{1}{\sqrt{\pi f_b}} \exp(i2\pi f_c t) \exp\left(-\frac{t^2}{f_b}\right) \tag{3.3}$$

$$\hat{\psi}(f) = \exp\left\{-\pi^2 f_b (f - f_c)^2\right\} \tag{3.4}$$

where f_b is the non-dimensional bandwidth parameter, f_c is the wavelet central frequency in Hz, and i is the imaginary unit. f_b and f_c should be appropriately determined for the signals analyzed.

An example of the complex Morlet wavelet function with $f_b = 0.5$ and $f_c = 4$ is shown in Fig. 3.5. For practical applications, the complex Morlet wavelet is considered admissible if $2\pi f_c \geq 5$ because of the fast decay of its envelope towards zero. In addition, there is a unique relation between the scale parameter a and the Fourier frequency f at which the wavelet is focused (Ciampa and Meo 2010; Kijewski and Kareem 2003):

$$f = \frac{f_c}{a} \tag{3.5}$$

Next, Shannon entropy (Piotrkowski et al. 2009) is introduced as a quantitative criterion to select the optimal mother wavelet with appropriate parameters, f_b and f_c. According to the information theory, entropy indicates the complexity or

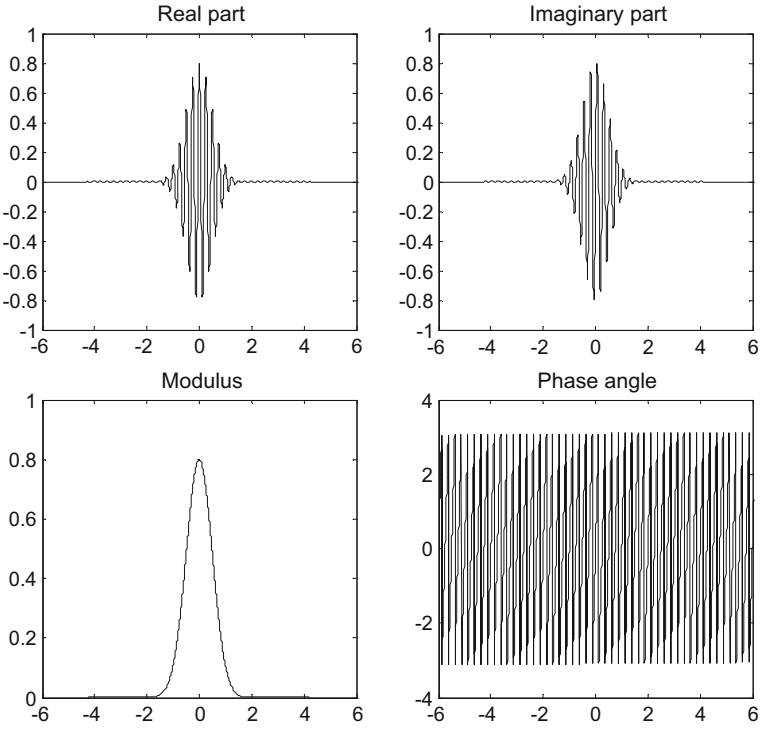

Fig. 3.5 An example of complex Morlet wavelet function with $f_b = 0.5$ and $f_c = 4$

uncertainty information of the signal or system (Cover and Thomas 2012). If the wavelet coefficient matrix of the wavelet transform is transformed into a series of probability distribution, the calculated entropy from this series reflects the sparseness degree of this wavelet coefficient matrix. Such entropy is called wavelet entropy, which indicates the similarity between the basis function and the analyzed signal. The smaller the entropy, the bigger the similarity, and thus used to select the basis function for the wavelet transform (He et al. 2008).

Considering a set of wavelet coefficients $\{wt(i,j)|i = 1,2,\ldots,I; \quad j = 1,2,\ldots,J\}$, where I is the total number of frequency scales and J is that of time instants. Its Shannon entropy is calculated as

$$E_{WT}^{S} = -\sum_{i=1}^{I}\sum_{j=1}^{J} p(i,j)\log p(i,j) \tag{3.6}$$

where $p(i,j)$ is the energy probability distribution of wavelet coefficients, defined as

$$p(i,j) = \frac{|wt(i,j)|^2}{\sum_{i=1}^{I}\sum_{j=1}^{J}|wt(i,j)|^2} \tag{3.7}$$

It is noted that $\sum_{i=1}^{I}\sum_{j=1}^{J} p_i = 1$, and $p_{ij}\log p_{ij} = 0$ if $p_{ij} = 0$. Low Shannon entropy indicates high diversity of the wavelet matrix, corresponding to high energy concentration. Thus, an optimal mother wavelet would produce a wavelet matrix of the minimum Shannon entropy:

$$\min\left\{E_{WT}^{S}(f_b,f_c)\right\} \tag{3.8}$$

Using AE signals obtained through the tests, the optimal mother wavelet was determined to be the complex Morlet wavelet with f_b = 0.5 and f_c = 4. As an illustration, the entropy calculation results of a crack-induced AE wave with various f_b and f_c are listed in Table 3.1. It can be seen shown that the optimal mother wavelet results in the lowest wavelet entropy value 4.416.

3.3.3 Time-Frequency Characteristics of AE Waves

The time-frequency characteristics of AE waves induced by PLB and operational noise were analyzed through WT. Figure 3.6 presents the waveform and WT of a PLB-induced AE wave. The wave energy is distributed mainly in the range of [100–400] kHz. There is also a notable portion of energy in the high frequency range of [500–700] kHz. Figure 3.7 presents the waveform and WT of a segment of operational noise. Markedly different from the PLB-induced AE wave, the operational noise caused by passing trains has energy contents clustering predominantly below 200 kHz. In view of these observations, the influence of noise can be greatly reduced by filtering out the lower frequency components of AE signal.

Table 3.1 Entropy calculation results of various mother wavelets

Complex Morlet f_b	Complex Morlet f_c						
	1	2	3	4	5	6	7
0.1	5.061	4.786	4.613	4.525	4.475	4.446	4.431
0.5	4.732	4.496	4.429	4.416	4.428	4.447	4.467
1	4.594	4.435	4.417	4.437	4.466	4.495	4.518
3	4.454	4.423	4.469	4.512	4.546	4.573	4.594
5	4.423	4.448	4.507	4.549	4.581	4.606	4.627
10	4.417	4.497	4.557	4.595	4.625	4.652	4.674

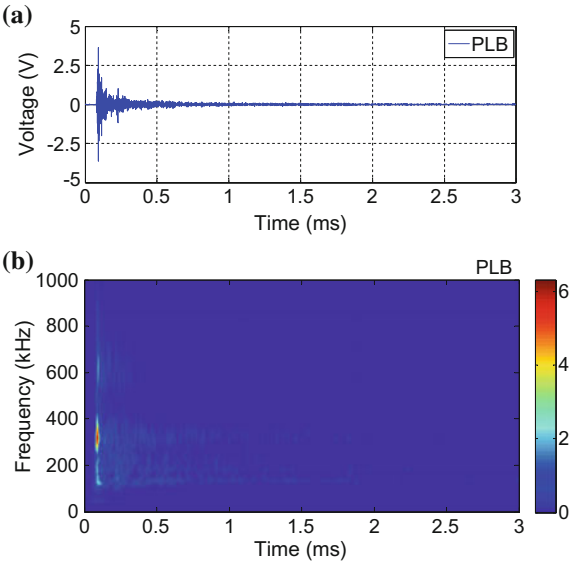

Fig. 3.6 A PLB-induced AE wave: **a** waveform and **b** WT

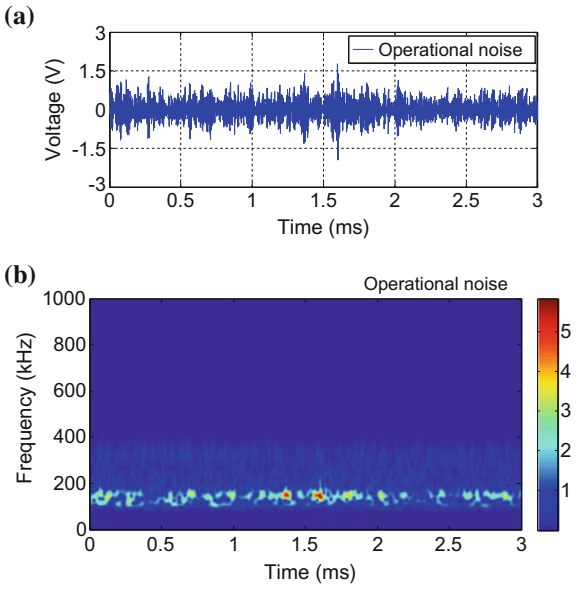

Fig. 3.7 Operational noise: **a** waveform and **b** WT

3.4 Propagation Features of AE Waves

The complexity of an AE signal depends on two aspects, its source and propagation path. Source features are related to the types of defect and material, and propagation path is mostly determined by the geometry of structure. In an application of AE

technique, sensors are typically expected to detect potential defects in the structure at several meters to tens of meters away. It is therefore necessary in this study to investigate the propagation features of AE waves in the rail head, including the energy attenuation and wave dispersion.

3.4.1 Theory of Ultrasonic Propagation

(1) Energy attenuation of ultrasonic waves

The energy of ultrasonic waves would dissipate as they propagate, and this occurs mainly in four ways, i.e. geometrical spreading, internal friction, scattering and diffraction, and dispersion (Nivesrangsan 2004).

Firstly, according to the law of energy conservation, geometrical spreading necessarily causes attenuation when waves emanate from a point source and spread over a larger wavefront. The wave amplitude (A_w) decreases inversely with distance (r) in three dimensional solids ($A_w \propto 1/r$), and inversely as square root of distance in two dimensional solids ($A_w \propto 1/\sqrt{r}$). As in one dimension bodies, like pipelines, I-beams and rail tracks, this effect is only visible in the near field.

Secondly, some of the mechanical energy associated with particle motion is converted into thermal energy during wave propagation in non-conservative media through various material-dependent mechanisms collectively known as internal friction. It usually causes wave amplitude to fall off exponentially with distance ($A_w \propto \exp(-kr)$ where k is an attenuation factor) (Finlayson et al. 2003).

Thirdly, when encountering complex boundaries and discontinuities like holes, slots, inclusions and cracks, AE waves are subjected to scattering and diffraction. Scattering occurs when waves propagate through a finite void or inclusion while diffraction occurs when waves propagate and encounter a sharp edge such as a crack. These effects result in a decrease in the amplitude of wave with increasing distance.

Fourthly, dispersion phenomena, commonly found in Lamb and Rayleigh waves, cause a decrease in the amplitude of wave although the total energy may remain constant. The details of dispersion phenomena will be described in the next section.

Generally speaking, steep attenuation happens in the near field of source which is dominated by geometry spreading. However, in the far field, internal friction dominates and leads to an exponential relationship of attenuation with distance, while wave dispersion has limited effects on the attenuation (Pollock 1986). The AE wave attenuation in real structures can be studied empirically, essentially by acquiring AE signals at various source-sensor distances (Miller et al. 2005).

(2) Propagation modes of ultrasonic waves

According to the propagation modes which depends on the types of confinement, ultrasonic waves can be divided into body waves, surface waves, plate waves, guided waves and others (Ensminger and Bond 2011; Ostachowicz et al. 2013).

Firstly, body waves occur ideally in infinite media, and include longitudinal waves and transverse waves. In longitudinal waves, also known as compression waves, the displacement of medium is parallel to the direction of wave propagation. This type of waves has the highest velocity and is therefore the first to be recorded if present. In transverse waves, also known as shear waves, the displacement of medium is perpendicular to the direction of wave propagation.

Secondly, surface waves (mainly the Rayleigh waves) travel along surface of semi-infinite media or a relatively thick solid material penetrating to a depth of about one wavelength. They combine both longitudinal and transverse modes to create elliptical motions, travel at a speed slightly lower than shear waves by a factor which is dependent on the elastic constant of the material, and may exhibit velocity dispersion in actual structures. More importantly, Rayleigh waves decay more slowly with distance than body waves, and are sensitive to surface defects when used for NDT.

Thirdly, plate waves (mainly the Lamb waves) only propagate in thin structures like plates and consist of numerous modes. These modes can be categorized into two families, i.e. symmetric modes and anti-symmetric modes. In symmetric modes, also known as extensional modes, particles mainly stretch and compress in the in-plane direction and the two surfaces of plate move in opposite directions. In antisymmetric modes, also known as flexural modes, particles mainly move out-of-plane, and the plate body bends as its two surfaces move in the same direction. However, it should be noted that these characteristics are not maintained at higher frequencies.

Fourthly, guided waves are stress waves that propagate along elongated structures while guided by their boundaries, such as finite plates, cylindrical pipes and rail tracks (Wandowski et al. 2011). In practice, the conditions of semi-infinite media and infinite plate for Rayleigh waves and Lamb waves cannot be satisfied most of time, and hence "guided Rayleigh waves" and "guided Lamb waves" would be more accurate. Similar to Lamb waves, guided Lamb waves consist of various modes, which may be more complicated than those of Lamb waves. However, such guided modes allow the waves to travel a long distance with little loss of energy. Long-range ultrasonics using guided wave has already been studied in the rail condition monitoring (Fan et al. 2007).

One of the key characteristics of Lamb waves (and some Rayleigh waves) is velocity dispersion, i.e. different frequency components travel through a media at different velocities, depending on the material density and elastic constant, structural thickness and wave frequency (or wavelength). Figures 3.8 and 3.9 show the dispersion curves of phase velocity and group velocity for two 347 steel plates of 10 and 38 mm thick, which are calculated according to the Rayleigh-Lamb equations (Viktorov 1967):

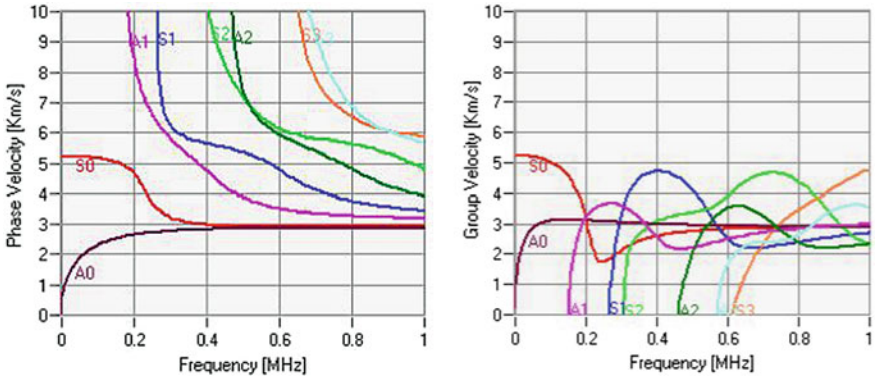

Fig. 3.8 Dispersion curves for a steel 347 plate of 10 mm thick

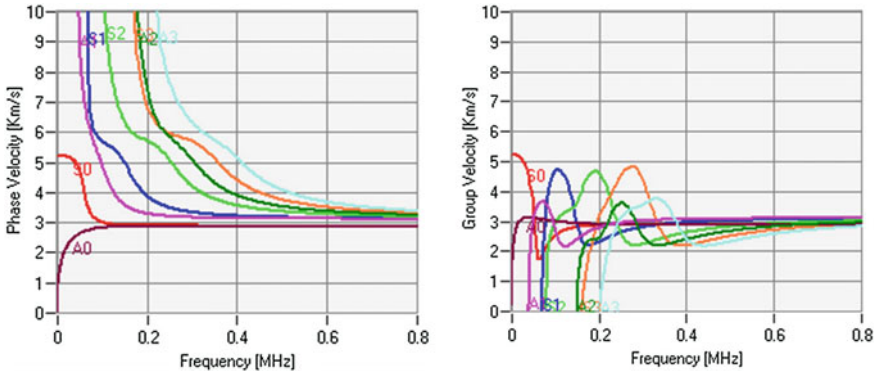

Fig. 3.9 Dispersion curves for a steel 347 plate of 38 mm thick

$$\begin{cases} \frac{\tan(qh)}{\tan(ph)} = -\frac{4k^2pq}{(k^2-q^2)^2} & \textit{for symmetric modes} \\ \frac{\tan(qh)}{\tan(ph)} = -\frac{(k^2-q^2)^2}{4k^2pq} & \textit{for anti-symmetric modes} \\ p^2 = \frac{\omega^2}{c_l^2} - k^2 \quad \textit{and} \quad q^2 = \frac{\omega^2}{c_t^2} - k^2 \end{cases} \tag{3.9}$$

where h is the half plate thickness, k is the wave number, ω is the angular frequency, c_l is the longitudinal wave velocity and c_t is the shear wave velocity. Then, the phase velocity c_p and group velocity c_g are calculated as $c_p = \omega/k$ and $c_g = d\omega/dk$. It is the group velocity but phase velocity that determines the waveform of AE signals. Here, S0–S4 are symmetric modes, and A0–A4 are anti-symmetric modes. The dispersion phenomena lead to a rich variety of experimentally observed waveforms which could help to locate defects in NDTs.

Table 3.2 Speeds of different AE wave modes in various materials

Materials	Wave speed (m/s)				Acoustic impedance (10^6 kg/m^{2}s)
	Compression wave	Shear wave	Rayleigh wave	Lamb wave	
Steel	5900	3200	3000	5100	46
Cast iron	5000	3000	2700	4700	36
Aluminum	6300	3100	2900	5100	17
Copper	4700	2300	2100	3800	42

Furthermore, examples of wave speeds for the longitudinal waves, transverse waves, and surface waves in metallic media are listed in Table 3.2. And the acoustic impedances of these materials are also included.

3.4.2 Attenuation of AE Waves in Rail Head

To obtain a more extensive coverage of crack monitoring, the sensing distance of AE sensors should be as long as possible. It was therefore of interest to examine the attenuation features of the AE waves travelling down the rail head. Figure 3.10 displays the attenuation trends of both PLB-induced AE waves and operational noise propagating along the rail head. As the propagation distance increased from 0.0 to 50.0 m, the peak amplitudes of PLB-induced AE waves was reduced from 4.05 to 0.016 V, while those of operational noise generated by the passing train varied from 1.95 to 0.12 V. In general, the AE wave induced by PLB exhibits a steeper attenuation compared to the operational noise. This is not surprising since

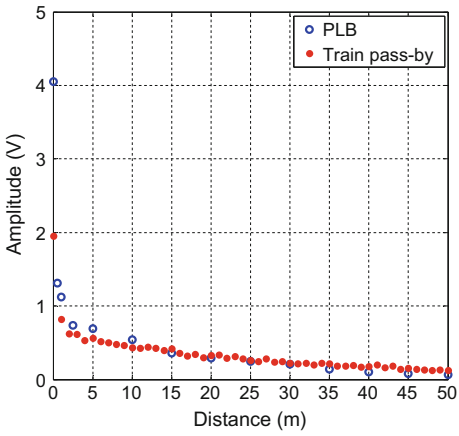

Fig. 3.10 Amplitude attenuation of PLB-induced AE waves and operational noise

PLB is a single-hit event, while a passing train is a continuously moving source. However, both types of the AE waves undergo steep decays initially followed by more gradual decreases with increasing distance.

3.4.3 Dispersion of AE Waves in Rail Head

The AE waves should be regarded as guided waves when propagating along the rail head, which can be assumed to be a beam-like structure. Because of the irregular cross-section of rail track, it is difficult to apply the Rayleigh-Lamb equation to determine the dispersive wave modes and their group velocities in rail head (Coccia et al. 2011; Zhang et al. 2014). This is further complicated by the frequency components of AE source, modulation effect of AE sensor and multiple reflections from structural boundaries. Thus, the dispersion phenomena of the AE waves propagating in the rail head were experimentally examined in this study. As an example, Fig. 3.11 shows the WT spectrum of an AE wave with propagation distance of 20.0 m. Three dispersive wave modes, named M1, M2, and M3, respectively, are clearly observed. However, if the propagation path is too short, it would be difficult for the wave modes to be distinguished from one another due to the time resolution limit of data acquisition and the effect of local wave reflection. This is illustrated in Fig. 3.12 which shows the WT spectrum of another AE wave with propagation distance of less than 0.1 m. The concentrated wave energy shows no distinct dispersion indicating that the AE source and the sensor are very near each other.

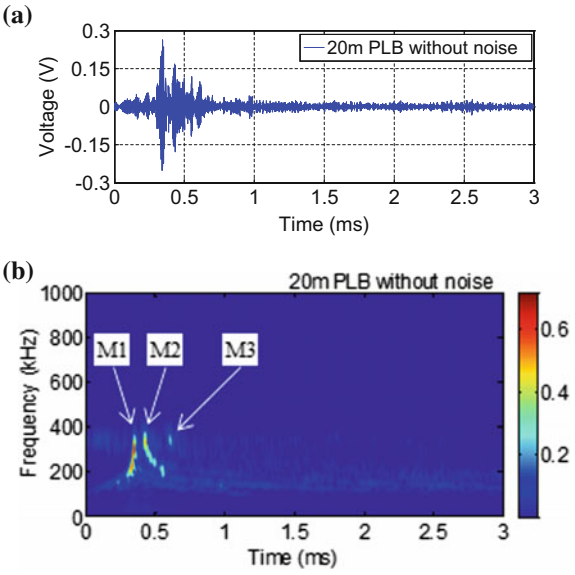

Fig. 3.11 Dispersive modes of an AE wave in rail head with propagation distance of 20.0 m: **a** waveform and **b** WT

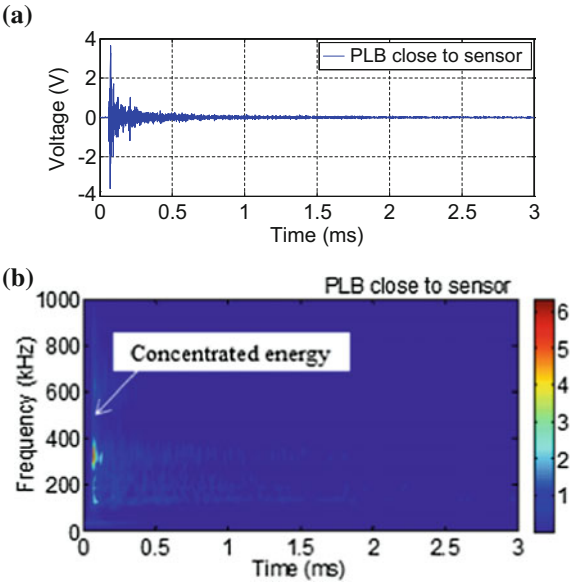

Fig. 3.12 An AE wave in rail head with source close to the sensor: **a** waveform and **b** WT

In addition, the dispersion phenomena of AE waves were also observed in the rail web and the rail foot respectively when PLB sources were done and AE sensor were installed on the these parts of the rail. Since the focus of this study is on crack detection in the rail head, details of these observations made for the rail web and rail foot will not be reported here.

3.5 Source Location Methods

The details of traditionally-used TOA method and advanced WTMA method will be introduced in this section.

3.5.1 Time-of-Arrival (TOA) Method

TOA method is based on the difference between arrival times of an AE event at different sensor locations. For one-dimensional structures like rail track, at least two sensors, labelled as S1 and S2 as shown in Fig. 3.13, are needed to locate the AE source. The distance between two sensors d_0 and velocity of AE wave V are pre-calibrated, and are known values which are used for source location computation. After the arrival times of AE wave at two sensors, t_1 and t_2, are captured, the distances between AE source and two sensors, d_1 and d_2, could be calculated

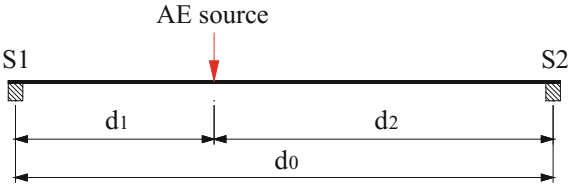

Fig. 3.13 Principle of AE source location on one-dimensional structures

according to Eq. (3.10) to estimate the location of the AE source. In practice, the arrival time of AE wave at the sensor is normally considered to be its first crossing of preset threshold.

$$\begin{cases} d_1 + d_2 = d_0 \\ d_2 - d_1 = (t_2 - t_1)V \end{cases} \tag{3.10}$$

This method is widely used in most commercial AE systems due to its simple working principle. The propagation velocity of AE wave in a structure is assumed to be constant, and the propagation path of the wave is assumed to be direct (i.e. the shortest path between source and sensor). Statistical algorithms could be introduced to improve the accuracy of the location prediction in conjunction with the use of more sensors or multiple AE hits. However, propagation velocity and path may vary for different parts of the structure, which may lead to errors in source location calculation. Furthermore, time delay between the arrival of the AE hit and threshold crossing could fluctuate resulting in increasing uncertainty and errors. These errors may be considerable when wave dispersion is significant.

3.5.2 *Wavelet Transform-Based Modal Analysis Location (WTMAL) Method*

(1) Preparatory work of WTMAL method

Before applying the WTMAL method to locate an AE source, the following three steps of preparatory work should be done: wave modes selection, scale selection and group velocity determination of wave modes. Firstly, two appropriate wave modes are selected as the objectives. WT is performed on AE wave as shown in Fig. 3.11, whereby M1 and M2 are proposed because their prominent magnitudes make them easily identified. Here, the complex Morlet wavelet with f_b = 0.5 and f_c = 4 Hz was selected as the optimal mother wavelet by minimizing the Shannon entropy of wavelet coefficients (see Sect. 3.3).

Secondly, the wavelet coefficients corresponding to a certain scale, i.e. frequency, are extracted, where the peaks would indicate the arrival times of selected wave modes travelling with different group velocities. An appropriate scale is selected where the wave modes concerned are typically present with high energy and clearly separated with each other. In this study, wavelet coefficients of the scale

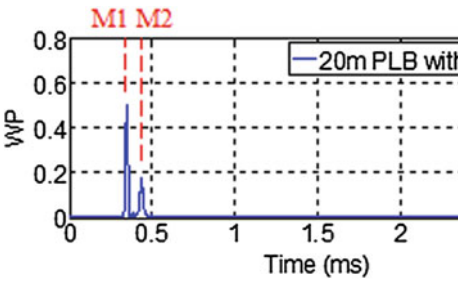

Fig. 3.14 WP at 300 kHz of an AE wave in rail head with propagation distance of 20.0 m

nearest to 300 kHz are extracted, and their WP (squared modulus) are plotted in order to accentuate the divergence (Fig. 3.14). The two main peaks having the highest amplitudes are identified as M1 and M2 respectively.

Thirdly, the group velocities of selected wave modes are experimentally determined using a pair of sensors attached to the host structure. The principle is similar to that of TOA method, as shown in Fig. 3.13. The distance between the two sensors is denoted by d_0, and the distances between AE source and the sensors are respectively d_1 and d_2. Let the arrival times of M1 at the two sensors be $t_{1,1}$ and $t_{1,2}$, and those of M2 be $t_{2,1}$ and $t_{2,2}$. Then their group velocities, V_1 and V_2, are obtained

$$V_1 = \frac{d_2 - d_1}{t_{1,2} - t_{1,1}} \quad \text{and} \quad V_2 = \frac{d_2 - d_1}{t_{2,2} - t_{2,1}} \tag{3.11}$$

(2) Application of WTMAL method

Following the preparatory work done as above, the cracks, i.e. AE sources, can be located using the WTMAL method. The distance d from AE source to a sensor, named target sensor, is calculated based on the temporal separation of the two selected wave modes and their group velocities:

$$d = (t_2 - t_1)\left(\frac{V_1 V_2}{V_1 - V_2}\right) \tag{3.12}$$

where t_1 and t_2 are the arrival times of M1 and M2 at the target sensor. It is worth noting that only the target sensor is needed for the purpose of distance calculation. The final location will then be identified with the help of its two neighbouring sensors on both sides. If the upstream sensor records the same AE event as the target sensor, the detected AE source should be on the upstream side of target sensor, and vice versa. A flowchart for the field application of WTMAL method is summarized in Fig. 3.15.

(3) Blind zone and working range of AE sensors

As highlighted earlier, if the distance between AE source and sensor is too short, the dispersion of wave modes would not be sufficiently large to be individually detected. Thus, in the WTMAL method, a minimum distance measured from the

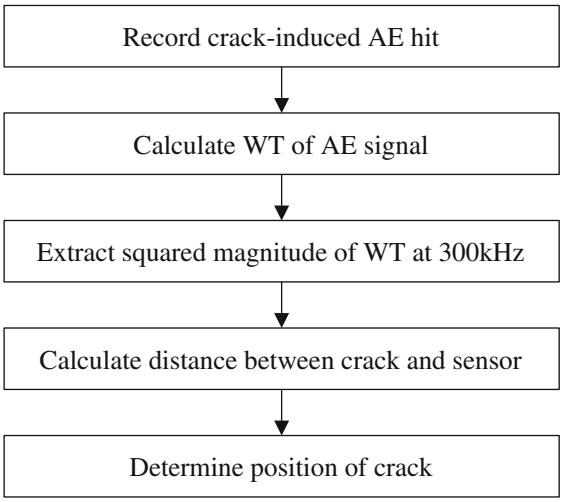

Fig. 3.15 Flowchart of crack location in rail head using WTMAL method

AE sensor is considered to be the blind zone, beyond which lies its working range. Another cause for the blind zone is that high operational noise would render source location more difficult, especially in the case of field rail track. Based on the field tests conducted, it is found that when a train wheel passes nearby, the target sensor could not identify a crack-induced AE wave generated from a long distance away, because the wave energy has been significantly attenuated and has become too weak relative to the train wheel-induced noise. Even the use of an analog filter with a very high high-pass cutoff frequency was not able to extract the signal from the noisy data. The sensor becomes ineffective when there is a train wheel running in its blind zone. However, this blind zone problem can be overcome by analyzing the data acquired through neighbouring sensors. Sensors could be arranged along the rail in such a way that the blind zone of a sensor could be monitored by its neighbouring sensors and vice versa. The working ranges of a network of AE sensors collectively could then cover the entire rail length of interest without any blind zone. The distance between neighbouring sensors could be determined finally depending on the experimental results.

3.6 Hilbert Transform-Based Noise Cancellation Method

AE signal in the field contains the information of both crack and operational noise. Due to the high operational noise encountered in the railway system, noise cancellation is necessary in order to improve the SNR and to detect crack-induced AE hits of interest by imposing a waveform amplitude threshold. The operating frequency ranges of AE sensor and analog filter could be properly selected during data acquisition. However, digital denoising is still valuable in view of its convenience

in post-processing of AE signal. In this section, a new noise cancellation method based on HT is employed to filter out those noise-related frequency components so as to determine the appropriate cutoff frequency value for field application.

Recently, (Chen and Wang 2012; Wang et al. 2015) formulated a signal decomposition theorem based on HT to accurately separate a finite bandwidth signal into a series of narrow band components. Feldman (2011b) further proposed to apply it as a zero-phase digital filter. The HT of a signal $x(t)$ is defined as the convolution integral of $x(t)$ with $(\pi t)^{-1}$:

$$HT[x(t)] = \tilde{x}(t) = \frac{1}{\pi} \int_{-\infty}^{\infty} \frac{x(\tau)}{t-\tau} d\tau \tag{3.13}$$

Physically, the HT is equivalent to a special kind of linear filter, where all the amplitudes of spectral components are left unchanged, but their phases are shifted by $-\pi/2$ (Feldman 2011a). The signal $x(t)$ is assumed to comprise relative slow components $s(t)$ and fast components $f(t)$ with non-overlapping spectra. A complex function $Y(t) = y(t) + i\tilde{y}(t)$ is introduced that has an intermediate spectrum between the spectra of $s(t)$ and $f(t)$. Here $\tilde{y}(t)$ is the HT of $y(t)$, and $y^2(t) + \tilde{y}^2(t) = 1$. For a constant cutoff frequency ω_c, $Y(t) = \cos \omega_c t + i \sin \omega_c t$. Then the low frequency components $s(t)$ and high frequency components $f(t)$ could be obtained through

$$\begin{cases} s(t) = HT[x(t) \cos \omega_c t] \sin \omega_c t - HT[x(t) \sin \omega_c t] \cos \omega_c t \\ f(t) = x(t) - s(t) \end{cases} \tag{3.14}$$

Equation (3.14) is regarded as a zero-phase digital filter that preserves the initial amplitude, frequency and phase relations of extracted components. The cutoff frequency could even be a function of time. More significantly, based only on the forward Hilbert transform, it is easier to be implemented than the filtering techniques based on wavelet packet and wavelet transform, and hence provides a new noise cancellation approach for AE signals of high non-stationarity. Figure 3.16 reveals the concept of HT-based noise cancellation method for rail crack detection, where the block diagram of digital filter is included. The energy of rail operational noise, considered as $s(t)$, is predominantly focused in relatively lower frequency range than that of crack-induced AE signal, considered as $f(t)$. A two-stage filtering process is designed in order to eliminate the aliasing and phase reversal due to discretization of signal. Through an appropriate cutoff frequency ω_c, the SNR of AE signals inundated with noise will be greatly improved.

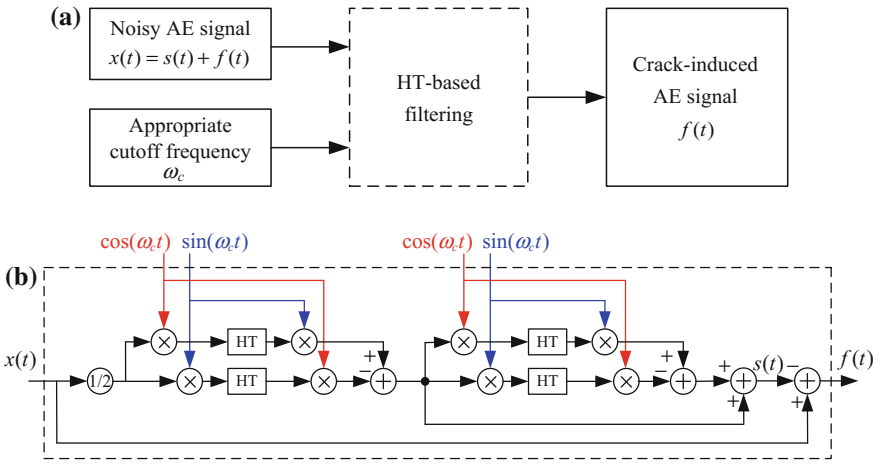

Fig. 3.16 HT-based noise cancellation method: **a** flowchart of concept and **b** block diagram of HT-based digital filter

3.7 Results and Discussion

3.7.1 Influence of Operational Noise on Crack Detection

The PLB-induced AE waves and operational noise were combined to simulate the actual events of rail head cracks in a typical noisy environment. It was of interest to first investigate the influence of operational noise on the capability of the proposed noise cancellation and source location methods. After taking into account the blind zone of 2.5 m, a segment of operational noise that was collected at 2.5 m away from wheel-rail contact point (a small segment from Fig. 3.4a with peak amplitude of 0.62 V) was selected and combined with those PLB-induced AE waves. Based on the previous time-frequency analysis, the HT-based noise cancellation method was applied to filter out the lower frequency components associated with the operational noise using a high-pass cutoff of 250 kHz. Figures 3.17 and 3.18 show the combined AE signals of 30.0 m case before and after denoising, respectively. From Fig. 3.17, it is evident that the combined signal was inundated with operational noise before denoising. The PLB-related features in both the time and time-frequency domains only became prominent after denoising, where lower frequency components were completely removed. The HT-based filter was thus demonstrated to be an effective noise cancellation method that significantly improves the SNR of AE signals. For a practical condition monitoring system, a 250 kHz high-pass analog filter could be used to detect the crack-induced AE hits easily through an amplitude threshold in time domain. However, even after denoising, the energies of PLB-induced AE waves after propagating more than 30.0 m and the energy of noise at 2.5 m away from the wheel-rail contact point

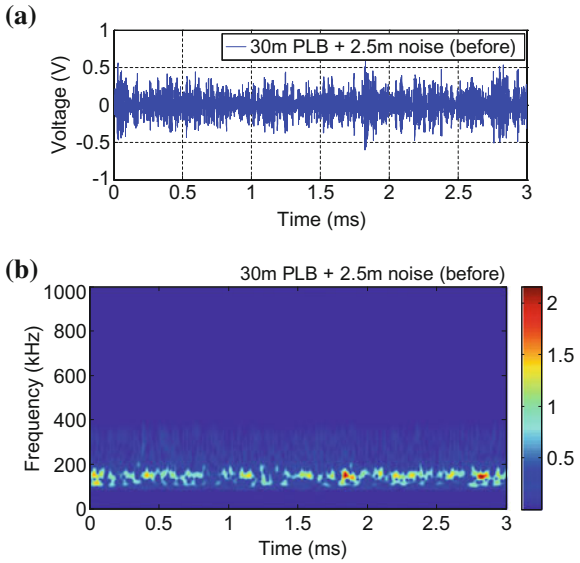

Fig. 3.17 AE signal combined by PLB-induced AE wave after propagating 30.0 m and operational noise at 2.5 m away from the wheel-rail contact point (before denoising): **a** waveform and **b** WT

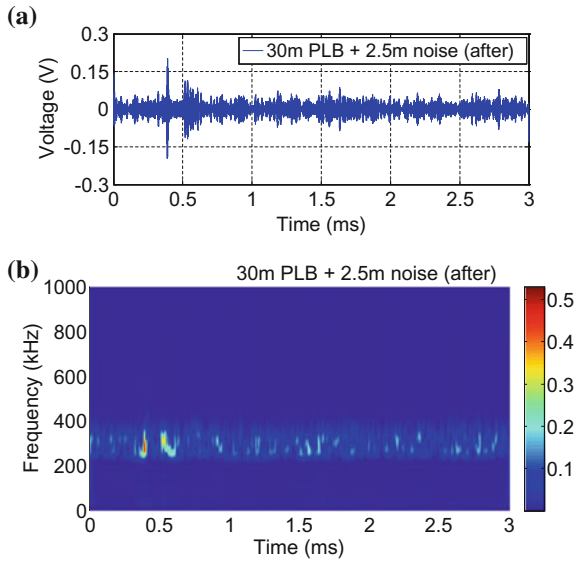

Fig. 3.18 AE signal combined by PLB-induced AE wave after propagating 30.0 m and operational noise at 2.5 m away from the wheel-rail contact point (after denoising): **a** waveform and **b** WT

were comparative. The average working range of each AE sensor would reduce from 40.0 to 30.0 m due to the influence of operational noise.

In addition, besides the wave dispersion, another reason for defining such a long blind zone of 2.5 m is the high operational noise (as shown in Sect. 3.2). It is further illustrated here by experimental results. Due to the small portion of wave energy of operational noise in the frequency range above 250 kHz overlapping with that of PLB-induced AE wave, the SNR of denoised AE signal may still be low

when the crack-induced AE wave is too weak relative to the operational noise (which is relatively high at the wheel-rail contact point). One example is the situation when a wheel is passing near the sensor and at which time a crack generates an AE wave at 30.0 m away stimulated by another wheel. The combined signals of the PLB-induced AE wave after propagating 30.0 m and the operational noise at the wheel-rail contact point (a small segment from Fig. 3.4a with peak amplitude of 1.95 V), are shown in Figs. 3.19 and 3.20, before and after denoising respectively. Unfortunately, even after denoising, it is still difficult to distinguish the PLB-induced AE wave from such high operational noise in either the time domain or time-frequency domain. It indicates that the sensor would become ineffective when there is a train wheel running in its blind zone even when a 250 kHz high-pass digital or analog filter is applied. Therefore, from the perspectives of both amplitude-threshold-trigger data acquisition of crack-induced AE hits and source location using WTMAL method, a blind zone for a single AE sensor does exist in its adjacent distance.

For the TOA method that requires a pair of sensors to locate the AE source, the concept of blind zone is not applicable. From Figs. 3.19a and 3.20a, it can be concluded that the average working range of each AE sensor in the TOA method would be much less than 30.0 m after considering the operational noise. Thus, only the source location results without noise are presented in this chapter for TOA method.

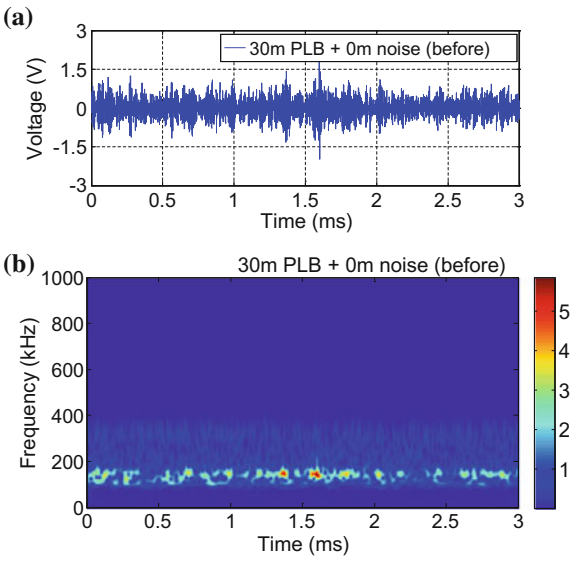

Fig. 3.19 AE signal combined by PLB-induced AE wave after propagating 30.0 m and operational noise at the wheel-rail contact point (before denoising): **a** waveform and **b** WT

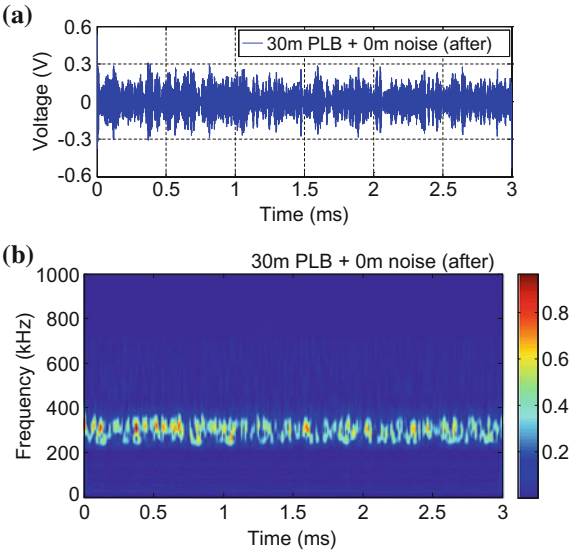

Fig. 3.20 AE signal combined by PLB-induced AE wave after propagating 30.0 m and operational noise at the wheel-rail contact point (after denoising): **a** waveform and **b** WT

3.7.2 Source Location Without Noise Using TOA Method

In the TOA method, each AE hit was detected by both sensors, and their corresponding arrival times recorded respectively. The wave velocity was calibrated to be 3029.13 m/s by taking the mean value of the velocities obtained from all the AE hits with various propagation distances. It is obvious that the calculated velocities of different AE waves are highly scattered with a large standard deviation of 63.48 m/s due to wave dispersion. It is expected to be even worse when noises generated by train operation introduce more random fluctuations on the threshold-crossing times of AE waves.

AE source could then be located based on the calibrated velocity. The results are listed in Table 3.3. It should be noted that TOA method is not able to identify AE sources which are located outside the distance between the two sensors. Overall, the results show the TOA method could locate the AE source with absolute errors of not more than 0.2 m. However, the average working range of sensors will be much less than 30 m after introducing the operational noise (of which the detailed results are thus not presented here).

3.7.3 Source Location Without Noise Using WTMAL Method

The WT of PLB-induced AE waves without operational noise were computed, and the wavelet coefficients of 300 kHz were extracted. The plots of waveform, WT and WP at 300 kHz for AE waves recorded by S1 with propagation distances 2.5, 10.0, 30.0 and 40.0 m are shown in Figs. 3.21, 3.22, 3.23, 3.24. Those for the case of

Table 3.3 Source location of PLB simulated AE waves without operational noise using TOA method

Propagation distance (m)	$d_2 - d_1$ (m)	$t_2 - t_1$ (μs)	Calibrated velocity (m/s)	Identified d_1 (m)	Absolute error (m)
1.0	28.0	−9114.5	3029.13	1.20	0.20
2.5	25.0	−8146.5		2.66	0.16
5.0	20.0	−6487		5.18	0.18
10.0	10.0	−3230		10.11	0.11
15.0	0.0	77.6		15.12	0.12
20.0	−10.0	3307.5		20.01	0.01
25.0	−20.0	6492		24.83	0.17
30.0	−30.0	10,012.1		30.16	0.16

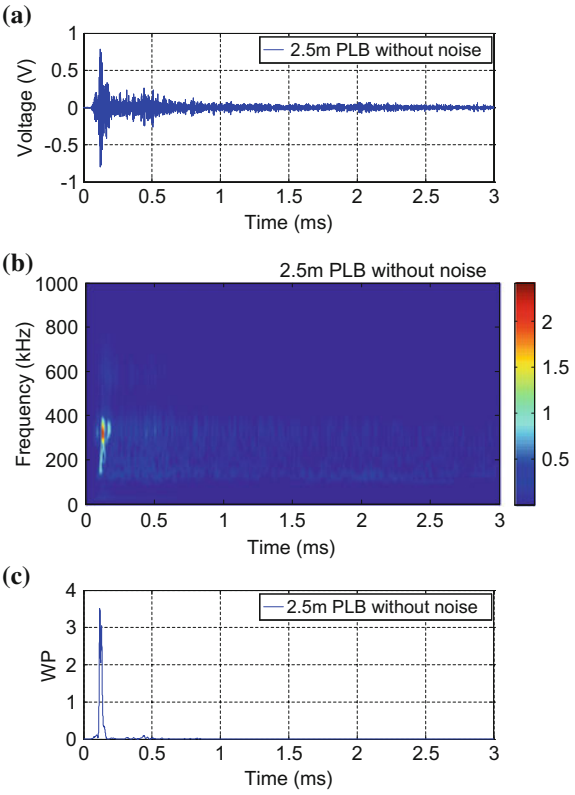

Fig. 3.21 PLB at 2.5 m without operational noise: **a** waveform, **b** WT and **c** WP at 300 kHz

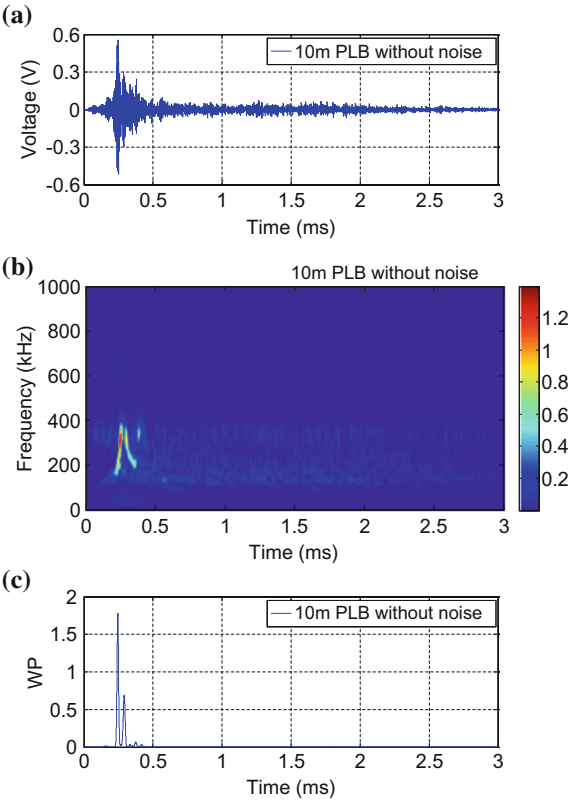

Fig. 3.22 PLB at 10.0 m without operational noise: **a** denoised waveform, **b** WT and **c** WP at 300 kHz

propagation distance 20.0 m has already been displayed in Figs. 3.11 and 3.14. As can be seen in the WP plots, the two selected wave modes produce two main distinct peaks. The highest peak is induced by M1, and the second highest peak is by M2, of which the amplitude is generally above 20% of that of M1.

As an preparatory step, the group velocities of dispersive wave modes M1 and M2 in rail head were determined according to Eq. (3.11) using the PLBs data of S1 and S2, as shown in Table 3.4. The velocities in each case of propagation distance are the average results of ten PLBs. The results of all the cases are further averaged to obtain the final two group velocities at 300 kHz, respectively 2960.15 and 2920.50 m/s with standard deviations below 2.00 m/s. As indicated previously, due to the short propagation distance, the two wave modes could not be identified at 0.0, 0.5 and 1.0 m. In the case of 15.0 m, Eq. (3.11) did not yield a solution because $d_2 - d_1 = 0$. Besides, when the propagation distance was longer than 40.0 m, the energies of wave modes, especially M2, became too weak to be clearly identified in the WT.

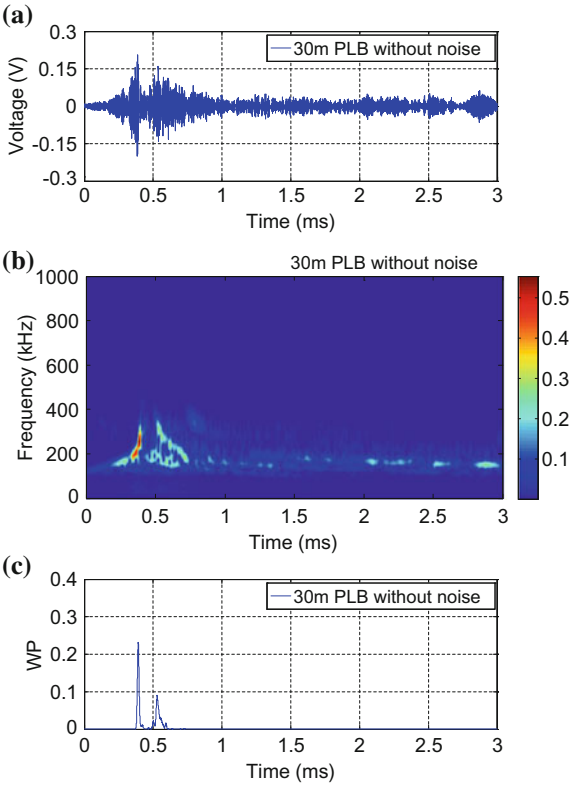

Fig. 3.23 PLB at 30.0 m without operational noise: **a** denoised waveform, **b** WT and **c** WP at 300 kHz

Based on the dispersion observations above, the blind zone of a single AE sensor was preliminarily defined to be within 2.5 m when using WTMAL method, and the working range of the sensor alone was then to be from 2.5 to 40.0 m on each side of the sensor. Taking S1 as the target sensor, the PLB-induced AE waves in its working range were investigated. The time differences of wave modes, $t_2 - t_1$, were then extracted. Based on the experimentally determined group velocities, the distances between various AE sources and the sensor were computed according to Eq. (3.12). As tabulated in Table 3.5, the proposed source location method successfully located the AE sources with errors of less than 0.3 m along the rail head when there was no operational noise. Through the cooperation between neighbouring sensors, the average working range of 40.0 m was possible for each sensor.

3.7.4 Source Location with Noise Using WTMAL Method

The source location ability of the WTMAL method was further studied using AE signals with operational background noise. Here, a series of cases with PLB locations in the working range of the target AE sensor, i.e. 2.5–30.0 m, were

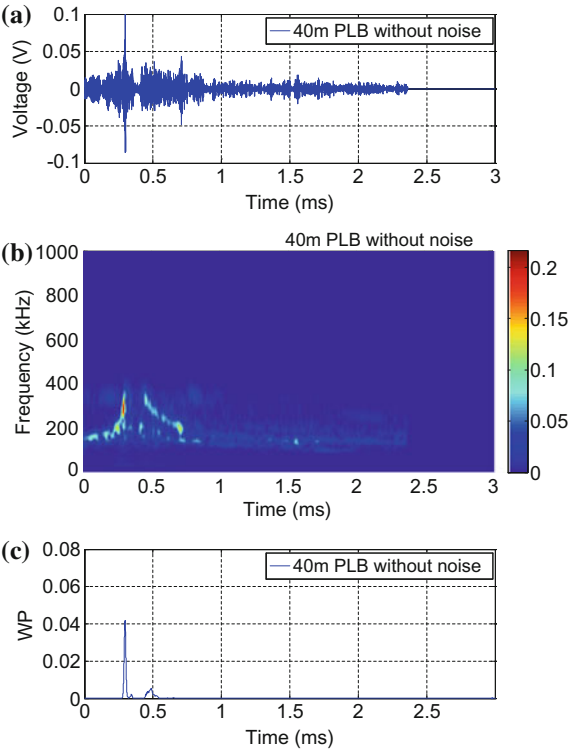

Fig. 3.24 PLB at 40.0 m without operational noise: **a** waveform, **b** WT and **c** WP at 300 kHz

Table 3.4 Group velocity determination results for WTMAL method

Propagation distance (m)	V_1 (m/s)	Mean (m/s)	Standard deviation (m/s)	V_2 (m/s)	Mean (m/s)	Standard deviation (m/s)
2.5	2958.25	2960.15	1.23	2919.42	2920.50	1.50
5.0	2959.81			2919.95		
10.0	2960.95			2921.56		
20.0	2961.24			2919.88		
25.0	2958.97			2918.43		
30.0	2961.57			2922.50		
35.0	2959.32			2919.79		
40.0	2961.12			2922.47		

investigated. After applying the HT-based filter with a high-pass cutoff frequency of 250 kHz, a set of denoised AE waves were obtained. The waveforms, WTs and WPs at 300 kHz for AE waves for cases of 2.5, 10.0, 20.0 and 30.0 m are respectively shown in Figs. 3.25, 3.26, 3.27, 3.28. The source location results of all

Table 3.5 Source location of PLB simulated AE waves with and without operational noise using WTMAL method

Propagation distance (m)	Without noise			With noise		
	$t_2 - t_1$ (μs)	Identified d (m)	Absolute error (m)	$t_2 - t_1$ (μs)	Identified d (m)	Absolute error (m)
2.5	11.7	2.62	0.12	11.7	2.62	0.12
5.0	23.4	5.10	0.10	23.4	5.10	0.10
10.0	47.0	10.25	0.25	47.2	10.29	0.29
15.0	67.8	14.78	0.22	67.6	14.73	0.27
20.0	90.6	19.75	0.25	90.6	19.75	0.25
25.0	113.8	24.81	0.19	113.8	24.80	0.20
30.0	138.6	30.22	0.22	138.8	30.25	0.25
35.0	161.8	35.28	0.28	–	–	–
40.0	184.8	40.29	0.29	–	–	–

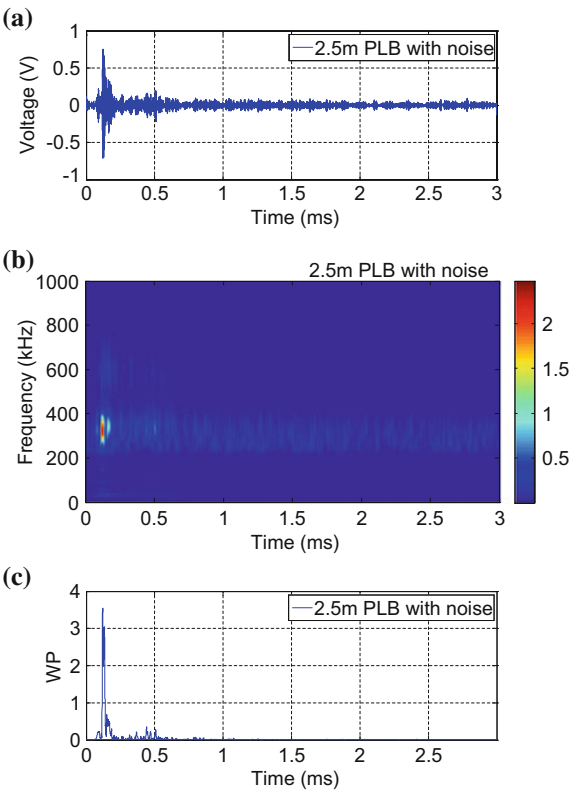

Fig. 3.25 PLB at 2.5 m with operational noise: **a** denoised waveform, **b** WT and **c** WP at 300 kHz

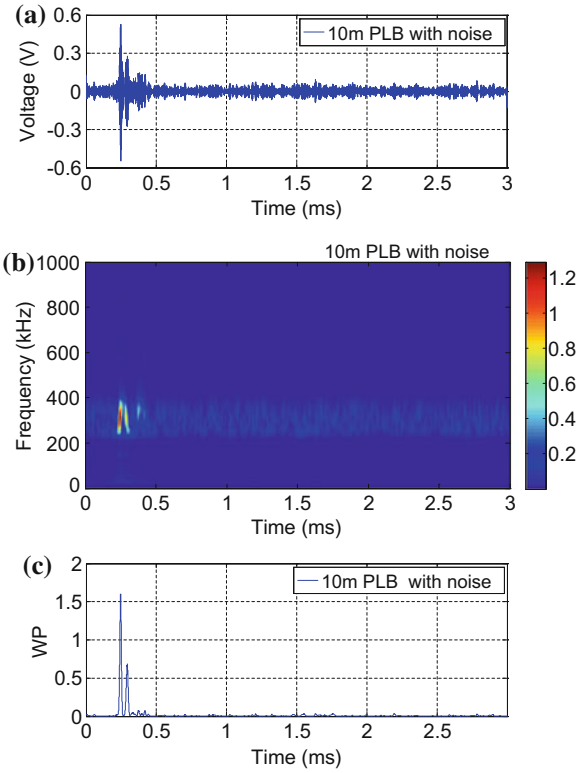

Fig. 3.26 PLB at 10.0 m with operational noise: **a** denoised waveform, **b** WT and **c** WP at 300 kHz

the PLB-induced AE signals with operational noise are listed in Table 3.5 for comparison with those of PLB-induced AE signals without operational noise. It is evident that even at high operational noise level the proposed source location method was still able to locate the AE sources with errors of less than 0.3 m along the rail head.

3.8 Concluding Remarks

This chapter focuses on the AE crack detection in rail head, which is one of the most vulnerable parts of rail track. A crack detection strategy, comprising of a source location method and a noise cancellation method, is proposed for application on the actual rail profile and material in the presence of operational noise. The main findings are summarized below.

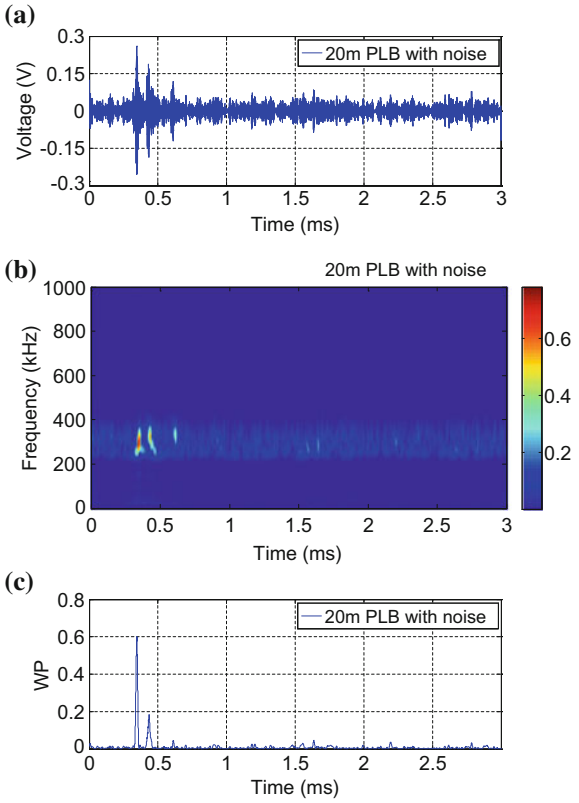

Fig. 3.27 PLB at 20.0 m with operational noise: **a** denoised waveform, **b** WT and **c** WP at 300 kHz

(1) The AE waves generated by PLBs at various source-sensor distances and the operational noise caused by passing trains were acquired separately through field tests. These two kinds of measured AE waves were combined to simulate the actual AE events of cracks in the rail head with field captured operational noise. AE waves arising from the rail head was found to be mainly guided in the rail head when propagating along the rail. The dominant wave velocity is approximately 3000 m/s.

(2) WT was utilized to investigate the time-frequency characteristics of the AE waves. Here, the complex Morlet wavelet with $f_b = 0.5$ and $f_c = 4$ Hz was selected as the optimal mother wavelet by minimizing the Shannon entropy of wavelet coefficients. Through WT, the PLB-induced AE waves were observed to behave with obvious dispersion when propagating along the rail head. The operational noise was found to have energy mainly concentrated in a relatively lower frequency range than where the PLB-induced AE waves operate.

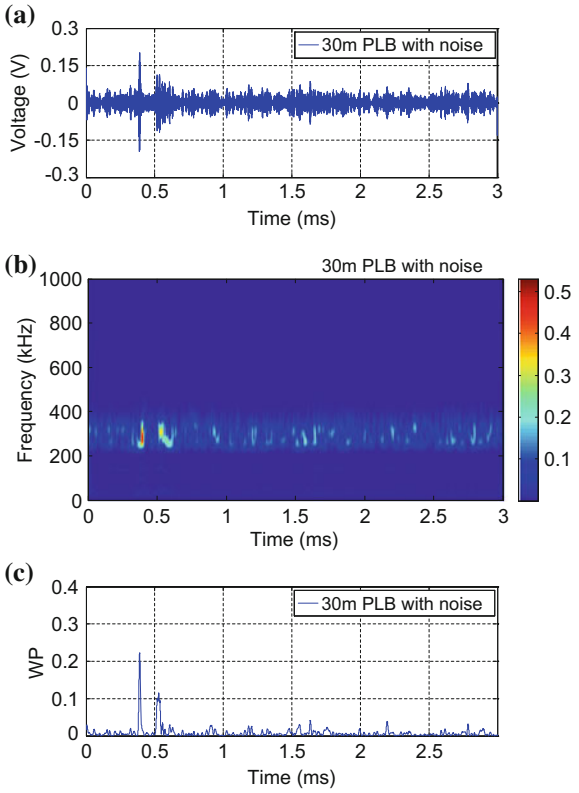

Fig. 3.28 PLB at 30.0 m with operational noise: **a** denoised waveform, **b** WT and **c** WP at 300 kHz

(3) In order to locate the AE sources (i.e. simulated cracks), the WTMAL method was proposed, which makes use of the dispersion phenomena of AE waves in rail head and requires only one sensor to determine the distance between AE source and sensor. The group velocities of the two dispersive wave modes used at a selected scale (nearest to 300 kHz) were experimentally determined to be 2960.15 and 2920.50 m/s respectively. For both the PLB-induced AE signals with and without operational noise, the AE sources could be located successfully with errors of less than 0.3 m along the rail head. Given the prevailing operational noise level detected and the WTMAL source location method used, the average working range of each AE sensor could reach 30.0 m, which is further than that obtained using the TOA method.

(4) A high-pass cutoff frequency of 250 kHz was recommended in order to identify crack-induced AE hits through an amplitude threshold in the presence of high operational noise. Although this denoising process could be achieved by an analog filter in a practical monitoring system, the HT-based noise cancellation method employed provides a new easy-to-use approach to improve the SNR in post-processing of AE signal.

References

ASTM. (2010). *E976-15 Standard Guide for Determining the Reproducibility of Acoustic Emission Sensor Response*. West Conshohocken, PA: ASTM International.

Audoin, B., Pan, Y., Rossignol, C., & Chigarev, N. (2006). On the use of laser-ultrasonics technique to excite selectively cylinder acoustic resonances. *Ultrasonics, 44,* e1195–e1198.

Chen, G., & Wang, Z. (2012). A signal decomposition theorem with Hilbert transform and its application to narrowband time series with closely spaced frequency components. *Mechanical Systems and Signal Processing, 28,* 258–279.

Ciampa, F., & Meo, M. (2010). Acoustic emission source localization and velocity determination of the fundamental mode A0 using wavelet analysis and a Newton-based optimization technique. *Smart Materials and Structures, 19*(4), 045027.

Coccia, S., Bartoli, I., Marzani, A., Lanza di Scalea, F., Salamone, S., & Fateh, M. (2011). Numerical and experimental study of guided waves for detection of defects in the rail head. *NDT and E International, 44*(1), 93–100.

Cover, T. M., & Thomas, J. A. (2012). *Elements of information theory*. US: Wiley.

Daubechies, I. (1992). *Ten lectures on wavelets* (Vol. 61). Philadelphia: Society for Industrial and Applied Mathematics (SIAM).

Ensminger, D., & Bond, L. J. (2011). *Ultrasonics: Fundamentals, technologies, and applications* (3rd ed.). Boca Raton: CRC Press.

Ernst, R., & Dual, J. (2014). Acoustic emission localization in beams based on time reversed dispersion. *Ultrasonics, 54*(6), 1522–1533.

Esveld, C. (2001). *Modern railway track* (2nd ed.). Zaltbommel: MRT-Productions.

Fan, Y., Dixon, S., Edwards, R. S., & Jian, X. (2007). Ultrasonic surface wave propagation and interaction with surface defects on rail track head. *NDT and E International, 40*(6), 471–477.

Feldman, M. (2011a). Hilbert transform in vibration analysis. *Mechanical Systems and Signal Processing, 25*(3), 735–802.

Feldman, M. (2011b). A signal decomposition or lowpass filtering with Hilbert transform? *Mechanical Systems and Signal Processing, 25*(8), 3205–3208.

Finlayson, R. D., Luzio, M. A., Miller, R. K., & Pollock, A. A. (2003). Continuous health monitoring of graphite epoxy motorcases (GEM). In *Proceedings of SPIE 5046, Nondestructive Evaluation and Health Monitoring of Aerospace Materials and Composites II*, San Diego, CA, USA, pp. 272–283.

Hamstad, M. A., O'gallagher, A., & Gary, J. (2002). A wavelet transform applied to acoustic emission signals: Part 2: Source location. *Journal of Acoustic Emission, 20*, 62–82.

Hamstad, M., & O'Gallagher, A. (2005). Effects of noise on Lamb-mode acoustic-emission arrival times determined by wavelet transform. *Journal of Acoustic Emission, 23,* 1–24.

He, Y., Yin, X., & Chu, F. (2008). Modal analysis of rubbing acoustic emission for rotor-bearing system based on reassigned wavelet scalogram. *Journal of Vibration and Acoustics, 130*(6), 061009.

Holford, K. M., Davies, A. W., Pullin, R., & Carter, D. C. (2001). Damage location in steel bridges by acoustic emission. *Journal of Intelligent Material Systems and Structures, 12*(8), 567–576.

Jiao, J., Wu, B., & He, C. (2008). Acoustic emission source location methods using mode and frequency analysis. *Structural control and Health monitoring, 15*(4), 642–651.

Kijewski, T., & Kareem, A. (2003). Wavelet transforms for system identification in civil engineering. *Computer-Aided Civil and Infrastructure Engineering, 18*(5), 339–355.

Mallat, S. (1999). *A wavelet tour of signal processing* (2nd ed.). London, UK: Academic press.

Marec, A., Thomas, J. H., & El Guerjouma, R. (2008). Damage characterization of polymer-based composite materials: Multivariable analysis and wavelet transform for clustering acoustic emission data. *Mechanical Systems and Signal Processing, 22*(6), 1441–1464.

Mikio, T., Hideon, I., & Kanji, O. (2000). Wavelet transform applications to AE signal analysis. In T. Kishi, M. Ohtsu, & S. Yuyama (Eds.), *Acoustic Emission-Beyond the Millennium* (pp. 35–56). Oxford: Elsevier.

Miller, R. K., Moore, P. O., & Hill, E. V. K. (2005). *Nondestructive Testing Handbook: Vol. 6, Acoustic Emission Testing* (3rd ed.). Columbus: American Society for Nondestructive Testing.

Niri, E. D., & Salamone, S. (2012). A probabilistic framework for acoustic emission source localization in plate-like structures. *Smart Materials and Structures, 21*(3), 035009.

Nivesrangsan, P. (2004). *Multi-source, multi-sensor approaches to diesel engine monitoring using acoustic emission* (Ph.D., Heriot-Watt University, UK).

Ostachowicz, W., Malinowski, P., & Wandowski, T. (2013). Damage localisation using elastic waves propagation method experimental techniques. In W. Ostachowicz & J. A. Güemes (Eds.), *New trends in structural health monitoring*. Udine, Italy: Springer.

Physical Acoustics Corporation. (2016a). Micro80D miniature differential sensor. Retrieved from http://www.mistrasgroup.com/products/solutions/acousticemission/sensors/Micro80D.aspx.

Piotrkowski, R., Castro, E., & Gallego, A. (2009). Wavelet power, entropy and bispectrum applied to AE signals for damage identification and evaluation of corroded galvanized steel. *Mechanical Systems and Signal Processing, 23*(2), 432–445.

Pollock, A. A. (1986). Classical wave theory in practical AE testing. In *Progress in Acoustic Emission III, The 8th International Acoustic Emission Symposium*, pp. 708–721.

Suzuki, H., Kinjo, T., Hayashi, Y., Takemoto, M., Ono, K., & Hayashi, Y. (1996). Wavelet transform of acoustic emission signals. *Journal of Acoustic Emission, 14*(2), 69–84.

Teolis, A. (1998). *Computational Signal Processing with Wavelets*. Boston: Birkhäuser.

Viktorov, I. A. (1967). *Rayleigh and lamb waves: Physical theory and applications*. New York: Springer.

Wandowski, T., Malinowski, P., Kudela, P., & Ostachowicz, W. (2011). Guided wave-based detection of delamination and matrix cracking in composite laminates. *Proceedings of the Institution of Mechanical Engineers, Part C: Journal of Mechanical Engineering Science, 225* (1), 123–131.

Wang, Z. C., Geng, D., Ren, W. X., Chen, G. D., & Zhang, G. F. (2015). Damage detection of nonlinear structures with analytical mode decomposition and Hilbert transform. *Smart Structures and Systems, 15*(1), 1–13.

Zhang, X., Feng, N., Wang, Y., & Shen, Y. (2014). An analysis of the simulated acoustic emission sources with different propagation distances, types and depths for rail defect detection. *Applied Acoustics, 86,* 80–88.

Zhang, X., Feng, N., Wang, Y., & Shen, Y. (2015). Acoustic emission detection of rail defect based on wavelet transform and Shannon entropy. *Journal of Sound and Vibration, 339,* 419–432.

Chapter 4
Sizing of Fatigue Cracks

AE technique has been widely applied to detect and locate fatigue cracks in metallic structures. However, it is still a challenging task to accurately quantify the size of a fatigue crack using AE technique (Gagar et al. 2014). The prospects of AE technique in rail crack monitoring would be significantly improved if it could be demonstrated not only as a means for identifying the existence of cracks but also for estimating their sizes. This chapter thus investigates the crack sizing method based on fatigue tests in the laboratory.

4.1 Introduction

When a fatigue crack grows in the metallic structure, AE waves are basically generated by two processes, namely, crack propagation (CP) and crack closure (CC), which are regarded as the primary and secondary AE sources respectively (Daniel et al. 1998; Lindley et al. 1978; Scruby 1987). The CP process involves plastic deformation, crack extension and fracture events within the plastic zone around the crack tip. This occurs mostly near the peak load where new crack surfaces are formed. The widely-used traditional method of crack sizing relies only on the CP-induced AE waves, which are extracted from approximately the top 20% of the fatigue load range (Rabiei and Modarres 2013; Roberts and Talebzadeh 2003a; Yu et al. 2011). Distinct correlations between the crack growth rate and corresponding AE count rate (or energy rate) have been established for various metallic materials through laboratory fatigue tests. The crack length could then be estimated by integration of the corresponding AE count rate (or energy rate) from an initial state of known crack length to the present state.

On the other hand, the CC process means that the two crack surfaces can come into contact each other at the lower ranges of fatigue load. This happens due to several mechanisms, including plastic deformation, accumulation of oxide debris and fretting of crack surfaces (Chang et al. 2009; Ritchie and Suresh 1982).

D. Li, *Rail Crack Monitoring Using Acoustic Emission Technique*,
Springer Theses, https://doi.org/10.1007/978-981-10-8348-8_4

Generally, the obvious phenomenon of CC can be observed when the load ratio is below 0.45 (Newman 1984; Singh et al. 2007), which is the case for many types of structures including rail tracks. Few studies to date have made use of the CC-induced AE waves. Singh et al. (2007) and Chang et al. (2009) utilized them to measure the closure loads to determine the effective stress intensity factor range. Gagar et al. (2014) suggested a new approach for crack length estimation by relating the applied cyclic load to the CC-induced AE signals.

For AE crack sizing in practical structures like rail tracks, there are two main limitations. Firstly, the load applied to the structures varies with time, and the exact load information traditionally used for classifying AE waves may not be readily available. Secondly, the initial crack length, which is required to estimate the present crack length in the traditional method, is difficult to determine in existing structures in view of their various deterioration states. In view of these limitations, this chapter attempts to develop a method that is able to evaluate the size of a fatigue crack without prior knowledge of initial crack length, integration of AE data or real-time load amplitude.

In this chapter, three-point bending fatigue tests of different loading conditions were carried out on rail steel specimens in the laboratory. For data pre-processing, a classification index based on wavelet power (WP) was initially established to distinguish between the CC-induced AE waves and their CP-induced counterparts. Following the AE wave classification, a novel method to quantify fatigue crack size was developed by taking advantage of the CC-induced AE waves, the count rate of which was found to be positively correlated with crack length. The results, advantages and disadvantages of both traditional and novel crack sizing methods will be presented and discussed in this chapter.

A flowchart of the proposed methodology for AE fatigue crack sizing is shown in Fig. 4.1, which includes two parts: AE wave classification using an index based on WP and crack sizing using a novel method based on CC-induced AE waves (together with the traditional method based on CP-induced AE waves). It is indicated that the AE wave classification index proposed for data pre-processing would benefit both the novel and the traditional crack sizing methods.

4.2 Experimental Procedure

4.2.1 Rail Steel Specimens

Three-point bending fatigue tests were carried out on rail steel specimens that were cut from the head of a Chinese 60 kg/m U71Mn rail (Fig. 4.2), similar to UIC 60 used worldwide. The chemical compositions and mechanical properties of the rail steel are listed in Tables 4.1 and 4.2. The dimensions of the specimens were 200 mm long, 40 mm high and 20 mm thick (Fig. 4.3). The support span was 160 mm. A notch of depth either 6 or 8 mm was machined at the bottom mid-span.

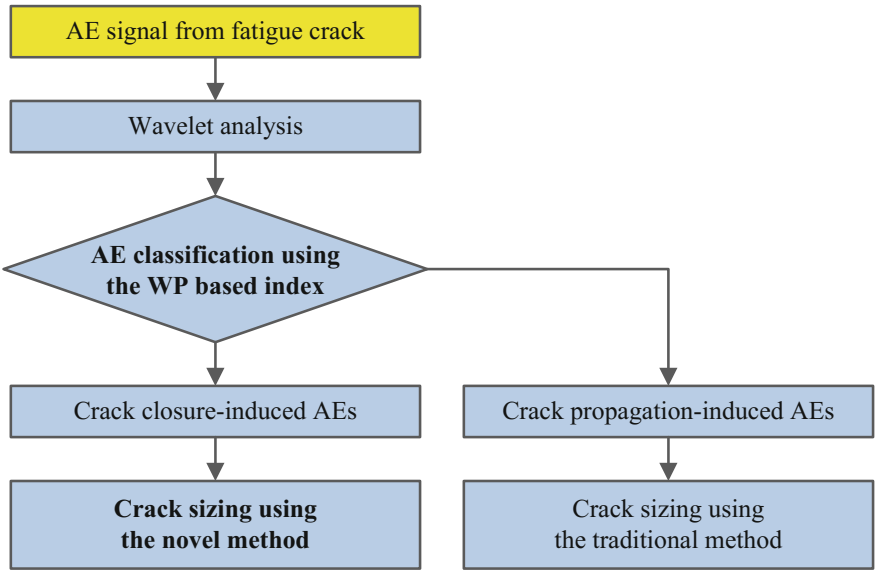

Fig. 4.1 Flowchart of fatigue crack sizing using AE waves

Fig. 4.2 Specimen cut from rail head (unit: mm)

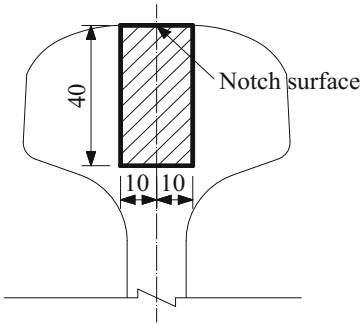

Six specimens of different notch depths and peak loads were tested, as illustrated in Table 4.3. They were categorized into three groups, each of which includes two specimens with the same test parameters (except a small variation of load ratio in Group 2).

4.2.2 Fatigue Tests

The universal testing machine (INSTRON MODEL 1334) was used to generate a sinusoidal load with load ratio of 0.1 or 0.2, load frequency of 5 Hz, and peak load

Table 4.1 Chemical compositions of rail steel used

C	Si	Mn	P	S	V	Ni	Cu	N
0.68	0.22	1.18	0.021	0.007	0.003	0.0068	0.0109	0.0064

Table 4.2 Mechanical properties of rail steel used

Tensile strength	Modulus of elasticity	Elongation rate	Brinell hardness
961 Mpa	206 GPa	14.5%	295 HBW

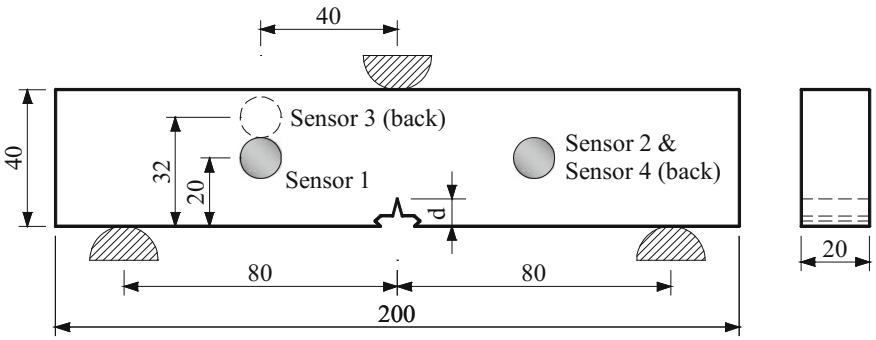

Fig. 4.3 Geometry and sensor layout of fatigue test specimen (unit: mm, d is the notch depth)

Table 4.3 Fatigue test parameters of rail steel specimens

Groups	Specimens	Notch depth (mm)	Peak load (kN)	Load ratio	Fatigue life (cycles)
Group 1	S1	8	25	0.1	40,713
	S2	8	25	0.1	42,976
Group 2	S3	6	25	0.1	78,394
	S4	6	25	0.2	83,200
Group 3	S5	6	20	0.1	139,926
	S6	6	20	0.1	146,649

of either 20 or 25 kN (as listed in Table 4.3). The reason for applying different loading parameters is to investigate the applicability of crack sizing methods among various stress levels and load ratios. A crack opening displacement (COD) gauge was installed to measure the crack length as the benchmark. The experimental setup is shown in Fig. 4.4.

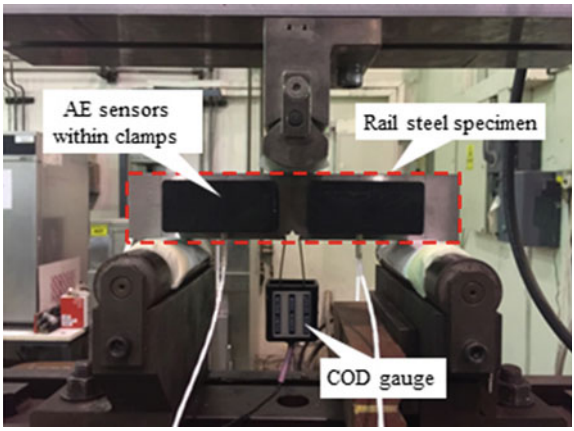

Fig. 4.4 Experimental setup

4.2.3 AE Data Acquisition

The AE signals were collected by a multi-channel Physical Acoustics (PAC) AE system. Four WD sensors were attached to the specimen surface using adhesive couplant and fixed in place with magnetic clamps. Preamplifiers (PAC 2/4/6) with a gain of 40 dB were used to amplify the voltage output from the sensors. AE signals were finally recorded by the data acquisition board at a sampling rate of 5 MHz.

WD sensor (Physical Acoustics Corporation 2016b) is a type of differential sensor which employed two sensing elements with opposite polarization directions to eliminate common-mode noise. It has a relative wide and flat operating bandwidth of 125–1000 kHz with a resonant frequency of approximately 450 kHz. This sensor is an ideal candidate for applications where high fidelity AE signal is critical. Accurate frequency analysis of the AE signal could then be carried out for noise discrimination and source identification. In addition, the sensor has a very high sensitivity, making it well-suited for structural health monitoring of large structures like storage tanks, pipelines, etc.

In order to suppress the influence of noise, several approaches were implemented. The analog band-pass filter was set to 100–1000 kHz, and the threshold for trigger-mode acquisition was determined to be 50 dB (referring to 1 μV at the sensor) to minimize the background noise after a series of trial-and-error. The loading and supporting pins were wrapped with cloth to eliminate the potential spurious AE hits induced by friction at the specimen surface. Furthermore, spatial filtering based on the time-of-arrival difference was performed by the four AE sensors shown in Fig. 4.3, to exclusively monitor the AE hits arising from area of the notch guided crack.

4.2.4 Crack Length Calculation

According to the ASTM standards E1820 and E647 (ASTM 2013a, b), crack lengths are calculated from the measurements of COD gauge:

$$\frac{a_i}{W} = 0.999748 - 3.9504u + 2.9821u^2 - 3.21408u^3 + 51.51564u^4 - 113.031u^5 \tag{4.1}$$

where

$$u = \frac{1}{\sqrt{\frac{BWEC_i}{S/4}} + 1} \quad \text{and} \quad C_i = \Delta v_m / \Delta P \tag{4.2}$$

Here, a_i is the crack length (including the notch) at the ith load cycle, v_m is the crack mouth opening displacement at notched edge, P is the applied load, and C_i is called experimental compliance. W is the specimen width, B is the specimen thickness, S is the support span, and E is the modulus of elasticity.

The plots of absolute crack length (excluding the notch) against elapsed load cycles for the three groups of specimens are displayed in Fig. 4.5. Their fatigue lives are approximately 45,000, 80,000 and 150,000 cycles, and final crack lengths before failure are close to 10, 12 and 14 mm, respectively. It can be observed that all the specimens successively experience the typical three stages of fatigue crack growth: initiation stage, stable propagation stage and fast propagation stage. Besides, the small variation of load ratios (from 0.1 to 0.2) does not bring significant influence on the fatigue life compared with the randomness induced by material property and other experimental conditions.

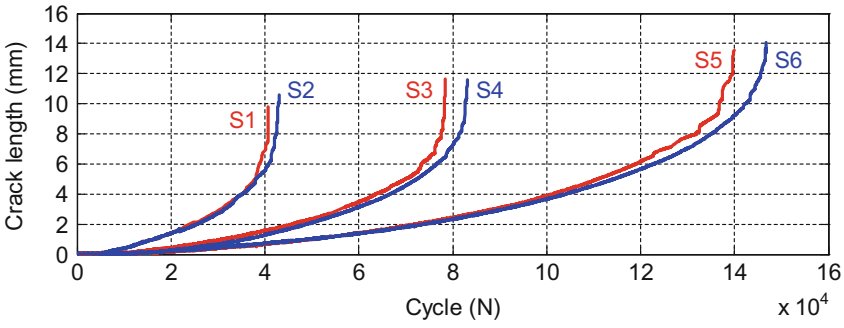

Fig. 4.5 Crack length against load cycles

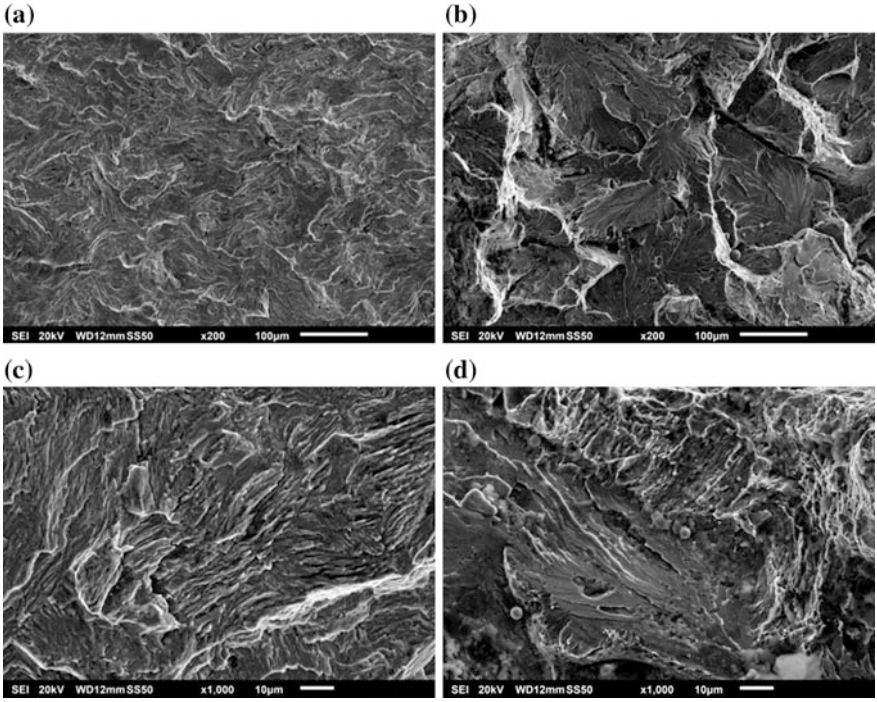

Fig. 4.6 SEM images of a crack surface of S6: **a** fatigue propagation at ×200; **b** final fracture at ×200; **c** fatigue propagation at ×1000; **d** final fracture at ×1000

4.2.5 Crack Surface Observation

Each of the specimens was loaded until failure, where a rapid fracture occurred as the crack reached a critical length. After testing, the crack surfaces were examined at 200× and 1000× magnifications respectively using a scanning electron microscope (SEM). The SEM images of S6 are shown in Fig. 4.6 for illustration. The fatigue propagation surfaces are characterized by flat facets and fatigue striations. These surfaces are relatively smooth due to the fretting between crack surfaces during the CC processes. In contrast, the final fracture surfaces exhibit predominantly micro-voids and micro-cracks.

4.3 AE Wave Classification

Since AE waves may be generated by either CP or CC processes during fatigue crack growth, the classification of these two types of AE waves is necessary as a pre-processing step to achieve more reliable crack sizing results. The two types of AE

waves were traditionally separated based on the corresponding load amplitudes. However, load amplitudes acting on structures could vary and are not readily available in field applications. In addition, the two types of AE waves could be induced under the same load levels as the crack grows (Kohn et al. 1992). There is no uniform load threshold that allows accurate AE separation even under controlled load conditions in the laboratory (Rabiei and Modarres 2013; Roberts and Talebzadeh 2003a; Yu et al. 2011). It is therefore highly desirable to be able to distinguish different types of AE waves depending solely on their intrinsic characteristics, i.e. information which is embedded within the AE signal itself. To achieve this, an index based on WP is hence established for the purpose of AE wave classification.

4.3.1 Wavelet Power (WP)-Based Classification Index

The AE waves associated with different mechanisms generally have different energy distribution in various frequency bands (Piotrkowski et al. 2009). For the wavelet analysis, a number of CP-induced AE waves were obtained from the top 5% of load ranges, while a number of CC-induced AE waves were obtained from the bottom 5% of load ranges in the fatigue tests. Figure 4.7 gives a 30-cycle snapshot of applied cyclic load (blue solid line) and recorded AE hits (red stars). The top and bottom 5% load ranges are highlighted by the dash line box.

Figures 4.8a–c and 4.9a–c show the waveforms, power spectral densities (PSDs) and CWTs of two examples of CP-induced AE hits respectively with higher and lower amplitudes. Figures 4.10a–c and 4.11a–c show two examples of CC-induced AE hits respectively exhibiting higher and lower amplitudes. The PSDs of these AE hits look very similar. However, it can be seen from the CWTs that the two types of AE waves are distinct from each other in the energy distribution.

A classification index based on WP is then expected to be able to distinguish between the two types of AE waves respectively induced by CP and CC. The maxima of WP with respect to various frequency scales, i.e. the projection of the wavelet ridges into the frequency domain, is an efficient way to quantitatively

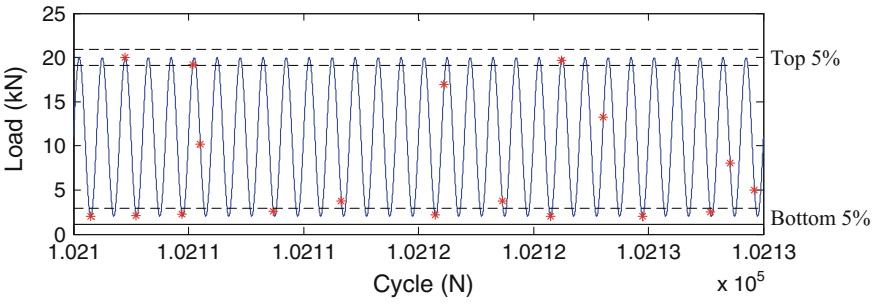

Fig. 4.7 A 30-cycle snapshot of applied cyclic load and recorded AE hits

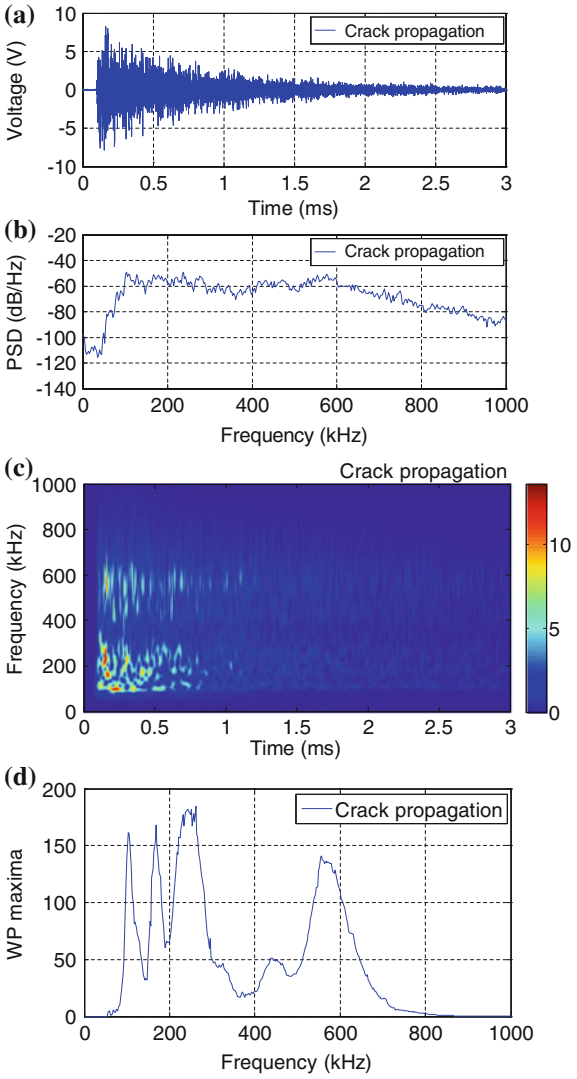

Fig. 4.8 CP-induced AE wave with a higher amplitude: **a** waveform, **b** PSD, **c** CWT and **d** WP maxima

analyze the energy distribution of AE signals (Niri and Salamone 2012). For the set of wavelet coefficients $\{wt(i,j)|i = 1,2,\ldots,I;\ j = 1,2,\ldots,J\}$, the maximum WP in each frequency scale i is

$$WP_i = \max\left\{|wt(i,j)|^2 \middle| j = 1,2,\ldots,J\right\} \tag{4.3}$$

As shown in Figs. 4.8d, 4.9d, 4.10d and 4.11d, the WP maxima plots of AE waves have peaks at various dominant frequency bands. The energies of CP-induced and CC-induced AE waves are concentrated mainly in the frequency

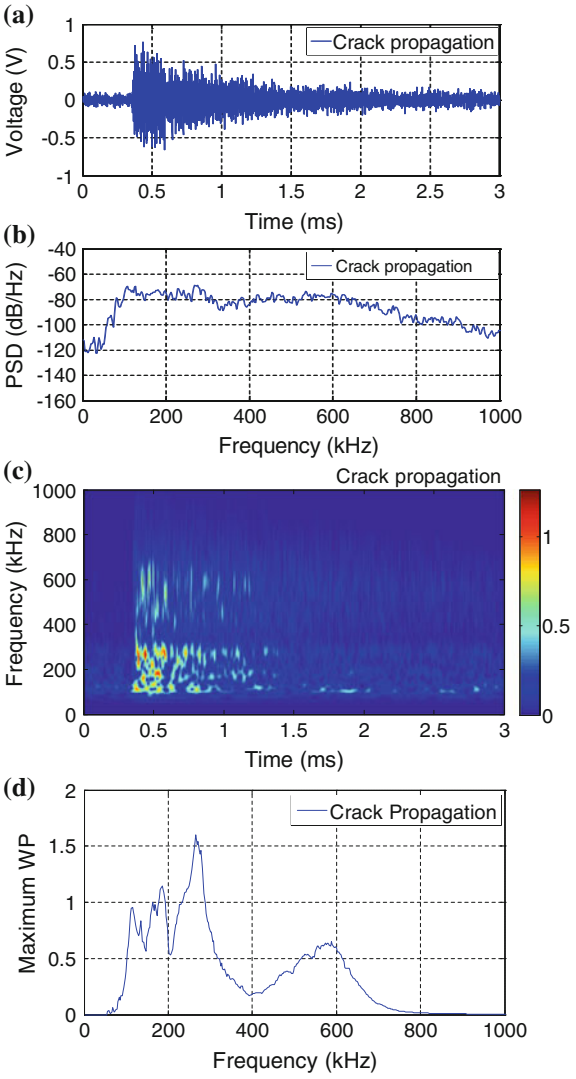

Fig. 4.9 CP-induced AE wave with a lower amplitude: **a** waveform, **b** PSD, **c** CWT and **d** WP maxima

band of [100–350] kHz. CP-induced AE waves also have a notable portion of energy in the higher frequency band of [400–650] kHz, whereas, the wave energy of CC-induced AE waves in the higher frequency band is almost negligible compared to that in the lower frequency band. In particular, this difference is clearly revealed by comparing Figs. 4.9d and 4.10d, WP maxima plots of two different types of AE waves with similar amplitudes in the time domain. Besides, the WP maxima plot of a background noise of fatigue tests (exhibiting amplitude less than

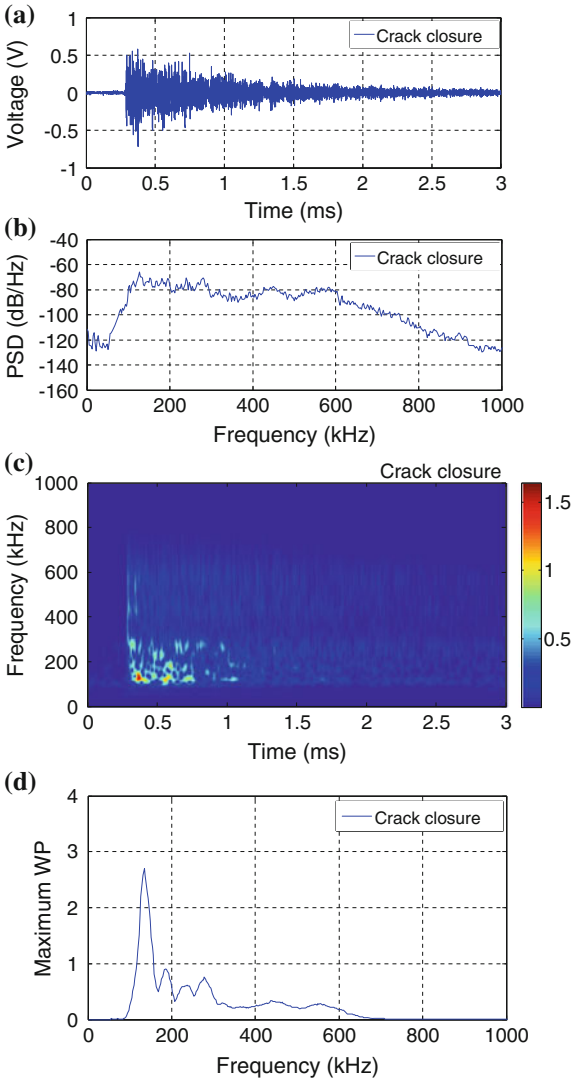

Fig. 4.10 CC-induced AE wave with a higher amplitude: **a** waveform, **b** PSD, **c** CWT and **d** WP maxima

0.03 V induced mainly by the Instron machine) is displayed in Fig. 4.12d. As can be seen, the energy of the noise in the higher frequency band of [400–650] kHz is weaker than that of CC-induced AE waves. The WP maxima plot is thus demonstrated to be an efficient quantitative tool which can be used to examine the energy distribution of AE waves in the frequency domain.

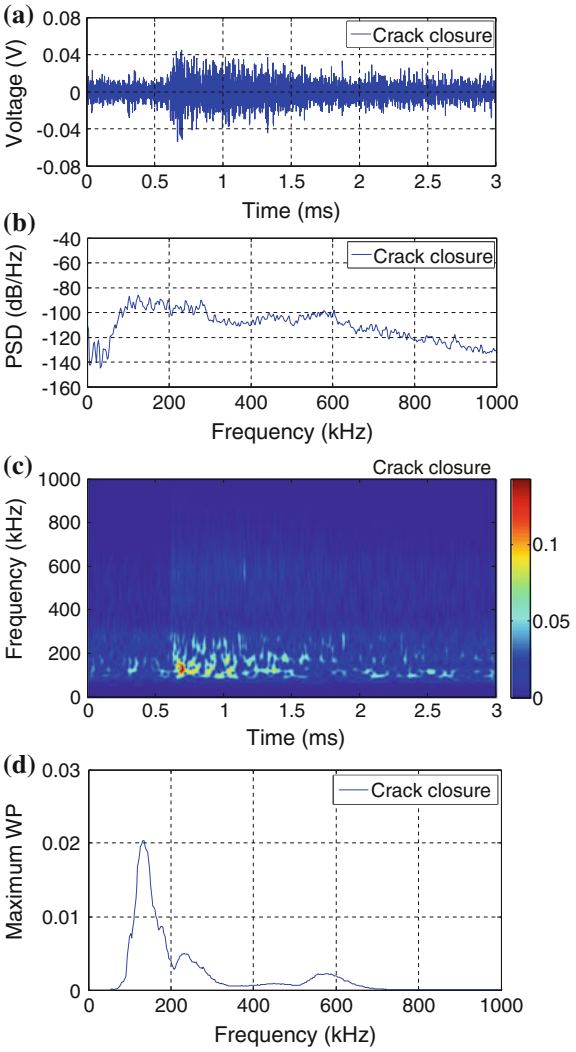

Fig. 4.11 CC-induced AE wave with a lower amplitude: **a** waveform, **b** PSD, **c** CWT and **d** WP maxima

In view of these observations, the ratio between the two WP maxima, from the two representative frequency bands B_1 = [100–350] kHz and B_2 = [400–650] kHz respectively, is defined as the classification index R:

$$R = \frac{\max\{WP_i | WP_i \subset B_2\}}{\max\{WP_i | WP_i \subset B_1\}} = \frac{P_2}{P_1} \tag{4.4}$$

It will be used to distinguish between the CP-induced and CC-induced AE waves by implementing an appropriate threshold.

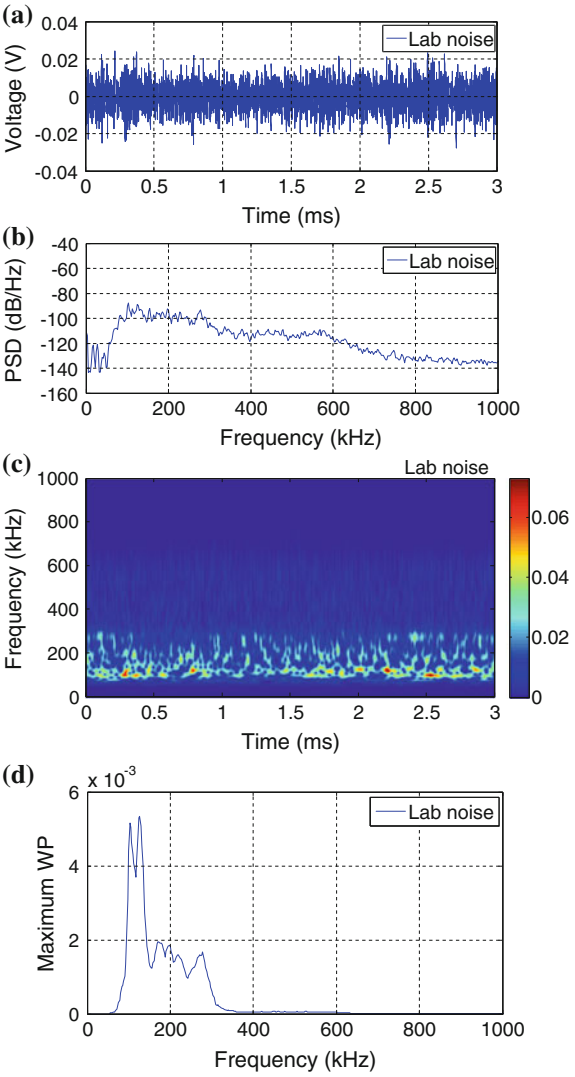

Fig. 4.12 Background noise of fatigue tests in the laboratory: **a** waveform, **b** PSD, **c** CWT and **d** WP maxima

4.3.2 Threshold Determination for the Classification Index

The threshold of the classification index is determined based on the probability density functions (PDFs) of the index values of the two types of AE waves. 1000 CP-induced AE hits recorded from the top 5% of load ranges and 1000 CC-induced AE hits recorded from the bottom 5% of load ranges were utilized to estimate the corresponding PDFs through the kernel density estimation (KDE) method (Bowman and Azzalini 1997). KDE is a non-parametric method for estimating the PDF of random variables. A kernel function is assigned to each of

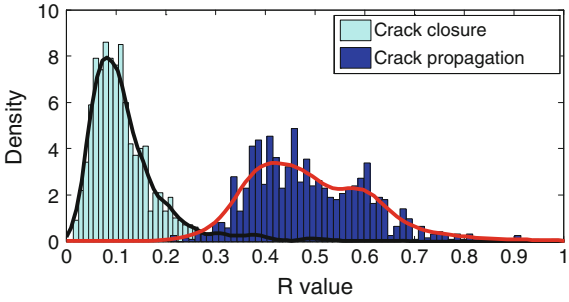

Fig. 4.13 Histograms and PDFs of index values

the N observations of a random variable X, and all the respective kernels are summed up to obtain the PDF (Botev et al. 2010):

$$\hat{f}(x;t) = \frac{1}{N}\sum_{i=1}^{N}\phi(x, X_i; t) \tag{4.5}$$

where

$$\phi(x, X_i; t) = \frac{1}{\sqrt{2\pi t}}\exp\left(\frac{(x - X_i)^2}{-2t}\right) \tag{4.6}$$

is the Gaussian kernel function with location X_i and scale $\sqrt{t}$ (usually referred as the bandwidth).

Figure 4.13 presents the two histograms and estimated PDFs of the classification index respectively for the CP-induced and CC-induced AE waves. To ensure a minimum error probability, the threshold for classification is set at the intersection of the two PDFs, which equals 0.27 as indicated by the blue arrow in Fig. 4.14. The overlap area in gray represents the error rate associated with the classification, which is below 0.06. Overall, the ratio between the two WP maxima from frequency bands B_1 and B_2 is found to be an effective index which could be used to classify CP-induced and CC-induced AE waves.

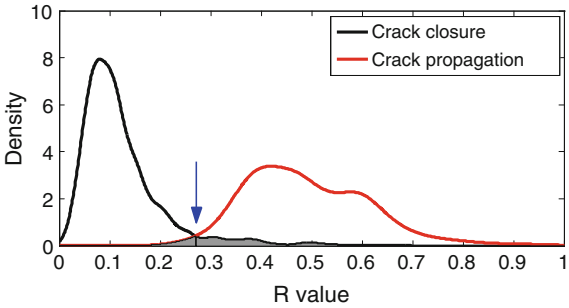

Fig. 4.14 Classfication threshold

Table 4.4 Selected results of classification error using different frequency bands

	B_1 = [100–160]		B_1 = [100–200]		B_1 = [200–350]		B_1 = [100–350]	
	Thr.	Err.	Thr.	Err.	Thr.	Err.	Thr.	Err.
B_2 = [400–500]	0.19	0.52	0.15	0.48	0.13	0.35	0.12	0.49
B_2 = [500–650]	0.34	0.38	0.31	0.29	0.30	0.25	0.25	0.10
B_2 = [400–650]	0.28	0.42	0.28	0.31	0.32	0.14	0.27	0.06

Note the unit of frequency bands is kHz

4.3.3 Frequency Bands Selection for the Classification Index

As mentioned previously, the two frequency bands used for the classification index are [100–350] kHz and [400–650] kHz. To achieve a robust classification index, the frequency bands were selected not only through visual observation of the wavelet analysis of AE waves, but also through a quantitative evaluation of the classification error. Based on the plots of CWT and WP maxima (as shown in Figs. 4.8, 4.9, 4.10 and 4.11), several frequency sub-bands were preliminarily obtained: [100–160] kHz, [160–200] kHz, [200–250] kHz, [250–350] kHz, [400–500] kHz, [500–650] kHz. For each bandwidth pair, the classification error was calculated by following the procedure as outlined in Sect. 4.3.2. Some selected results are reported in Table 4.4. It is clear from the table that the pair of [100–350] kHz and [400–650] kHz resulted in the minimum classification error of 0.06. Hence, this bandwidth pair was chosen for this study.

4.4 Fatigue Crack Sizing Methods

4.4.1 Traditional Method Based on CP-Induced AE Waves

It is well known that the fatigue crack growth generally proceeds through three stages: initiation stage, stable propagation stage and fast propagation stage. The Paris' law (Paris and Erdogan 1963) describes a critical relationship between fatigue crack growth rate da/dN and stress intensity factor range ΔK in the stable propagation stage:

$$\frac{da}{dN} = C_1(\Delta K)^{C_0} \tag{4.7}$$

where a is the crack length, N is the number of fatigue cycles, and C_0 and C_1 are material constants. Since the absolute energy of AE waves is considered proportional to the total energy released during crack propagation, an empirical

relationship between the count rate of crack propagation induced AE waves dc_p/dN and ΔK is widely used (Rabiei and Modarres 2013; Roberts and Talebzadeh 2003a; Yu et al. 2011):

$$\frac{dc_p}{dN} = C_3(\Delta K)^{C_2} \tag{4.8}$$

where c_p is the AE counts induced by crack propagation, and C_2 and C_3 are material constants. After eliminating ΔK, the relationship between dc_p/dN and da/dN, linear in the log-log scale, is deduced as:

$$\frac{da}{dN} = \alpha_1 \left(\frac{dc_p}{dN}\right)^{\alpha_0} \quad \text{or} \quad \log\left(\frac{da}{dN}\right) = \alpha_0 \log\left(\frac{dc_p}{dN}\right) + \log \alpha_1 \tag{4.9}$$

Here, α_0 and α_1 are also material constants. A higher AE count rate indicates a faster crack growth rate. The length of crack extension Δa during load cycles $N_i - N_j$ could be obtained through integration (Roberts and Talebzadeh 2003b):

$$\Delta a = \int_{a_i}^{a_j} da = \int_{N_i}^{N_j} \alpha_1 \left(\frac{dc_p}{dN}\right)^{\alpha_0} dN \tag{4.10}$$

where the numerical calculation is needed. This method is effective for detection of crack extension. However, the determination of crack length depends on the integration of AE information from an initial state of known crack length to the present cracked state. Thus, this method is useful for monitoring of newly-built structures with a known initial state, but not for in-service structures with many unknown existing cracks which are difficult to be calibrated. Moreover, this method is only accurate for the stable propagation stage of crack growth, which further limits its applicability.

4.4.2 *Novel Method Based on CC-Induced AE Waves*

During the growth of a fatigue crack under lower load ratio [below approximately 0.45 (Newman 1984; Singh et al. 2007)], the majority of AE waves are associated with CC instead of CP (Gagar et al. 2014; Li et al. 2015). The burst of CC-induced AE waves depends on the area of crack surfaces, material properties and load ratio. It is reasonable to postulate that, given a certain material, a higher rate of CC-induced AE waves is the direct result of a larger crack size in the structure. Based on the experimental data, the positive correlation between the count rate of AE waves induced by CC, dc_c/dN, and the crack length a can be described by a second-order polynomial:

$$a = \beta_2 \left(\frac{dc_c}{dN}\right)^2 + \beta_1 \left(\frac{dc_c}{dN}\right) + \beta_0 \tag{4.11}$$

where c_c is the AE counts induced by CC, β_0, β_1 and β_2 are regarded as material constants. According to the empirical model in Eq. (4.11), the size of fatigue crack can be directly estimated by the count rate of CC-induced AE waves. This method can be used to quantify fatigue cracks under low load ratios, which is the usual case for a large number of civil engineering structures. It has the potential to detect rolling contact fatigue cracks of rail track, where friction of crack surfaces is expected to occur when trains pass by (Esveld 2001). In addition, the estimation of crack length can be obtained based on just a small number of load cycles where the crack is not expected to grow. This is because the method is based on the AE waves induced by CC rather than those induced by CP, which is sparse. More importantly, this novel crack sizing method proposed here requires no prior knowledge of initial crack length and integration of AE data, and could be applied to monitor both of new and existing structures.

4.4.3 Comparison of Crack Sizing Methods

A comparison of three crack sizing methods, namely the traditional method (based on CP-induced AE waves), the proposed novel method (based on CC-induced AE waves), and a third method (based on CC-induced AE waves and loads) (Gagar et al. 2014) is summarized in Table 4.5. These methods employ different empirical models which were derived using experimental data, and each has its own strengths and weaknesses. These methods can be used to complement each other leading to a more robust crack sizing analysis when applied in practice.

4.5 Results and Discussion

4.5.1 AE Waves Classification

Using the classification index based on WP, the recorded AE hits of each specimen could be separated into the two types, i.e. AE induced by CP or CC. The classification result for specimen S6 is presented in Fig. 4.15. There are 4075 CP-induced AE hits, marked by the red bars, and 17,648 CC-induced AE hits, marked by the blue bars. It is obvious that the majority of AE data generated by the fatigue crack is associated with CC instead of CP. The height of the bar gives the amplitude of the corresponding AE wave. The amplitudes of AE hits induced by CP vary from 50 to 100 dB, while those of AE hits induced by CC are all below 80 dB.

Table 4.5 Comparison of crack sizing methods

Traditional method based on CP-induced AEs	
Model	A log-log linear relationship between the CP-induced AE count rate dc_p/dN and the crack growth rate da/dN: $\log\left(\frac{da}{dN}\right) = \alpha_0 \log\left(\frac{dc_p}{dN}\right) + \log \alpha_1$ Crack extension Δa during load cycles $N_i - N_j$: $\Delta a = \int_{a_i}^{a_j} da = \int_{N_i}^{N_j} \alpha_1 \left(\frac{dc_p}{dN}\right)^{\alpha_0} dN$ Note: a is the crack length; N is the number of fatigue load cycles; c_p is the AE counts induced by CP; α_0 and α_1 are material constants
Strengths and weaknesses	(1) Direct estimation of crack extension but absolute crack length
	(2) Prior knowledge of initial crack length needed
	(3) Real-time load amplitude not needed
	(4) Require continuous monitoring for the integration of AE data
	(5) Only applicable to the stable propagation stage of crack growth
	(6) Not limited by the load ratio
Proposed novel method based on CC-induced AEs	
Model	A second-order polynomial relationship between the CC-induced AE count rate dc_c/dN and crack length a: $a = \beta_2 \left(\frac{dc_c}{dN}\right)^2 + \beta_1 \left(\frac{dc_c}{dN}\right) + \beta_0$ Note: c_c is the AE counts induced by CC; β_0, β_1 and β_2 are material constants
Strengths and weaknesses	(1) Direct estimation of absolute crack length
	(2) Prior knowledge of initial crack length not needed
	(3) Real-time load amplitude not needed
	(4) Can be implemented in a few number of load cycles
	(5) Applicable throughout the crack growth
	(6) Limited to lower load ratios less than about 0.45
Method based on CC-induced AEs and loads (Gagar et al. 2014)	
Model	An exponential relationship between the average normalized stress range $f(a)$ where CC-induced AEs generated and the crack length a: $f(a) = \gamma_0 \exp(\gamma_1 a) + \gamma_2 \exp(\gamma_3 a)$ Note: γ_0, γ_1, γ_2 and γ_3 are material constants
Strengths and weaknesses	(1) Direct estimation of absolute crack length
	(2) Prior knowledge of initial crack length not needed
	(3) Real-time load amplitude needed
	(4) Can be implemented in a fewer number of load cycles
	(5) Applicable throughout the crack growth
	(6) Limited to lower load ratios less than about 0.45

Figure 4.15 also reveals the fatigue cycles and loads information corresponding to the AE hits. Firstly, the majority of the CP-induced AE hits concentrate in the vicinity of the top 10% of the load range, i.e. 18.2–20 kN, while the number of those hits occurring below 18.2 kN was found to gradually increase as the crack grows. In general, the load amplitudes corresponding to the CP-induced AE hits decrease as

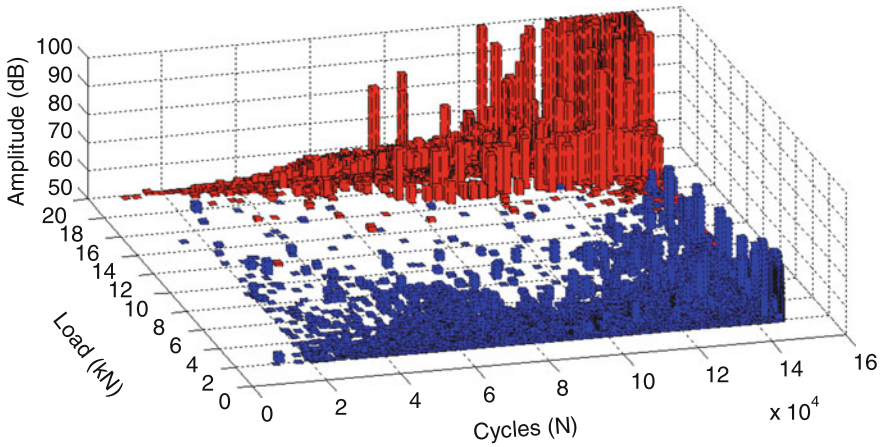

Fig. 4.15 AE waves classification for S6 (*Notes* red bars represent CP-induced AE waves; blue bars represent CC-induced AE waves)

the crack grows, especially at the final fast propagation stage. Secondly, the CC-induced AE hits arise mainly in the vicinity of the bottom 10% of the load range, i.e. 2–3.8 kN, while a large number of them spread throughout the entire load range. The AE classification results of the rest of the specimens are similar to that of S6. It is important to note that the corresponding load levels of the two types of AE waves overlap each other and errors would be inadvertently introduced if they are classified using a load threshold approach. Hence, to effective AE wave classification, the use of the intrinsic characteristics of AE signal is preferred instead of the load information.

The cumulative AE counts induced by CP are plotted against the load cycles for the six specimens tested as shown in Fig. 4.16. As expected, each specimen undergoes the slow-increase, stable-increase and fast-rise stages in the same progression as the crack growth. The cumulative AE counts induced by CC are also plotted against the load cycles for the six specimens for comparison and are shown in Fig. 4.17. As can be seen, each specimen increases smoothly as the load cycle elapses. The longer the fatigue life of a specimen, the larger the total number of CC-induced AE counts released.

4.5.2 *Crack Sizing Using the Traditional Method*

Figure 4.18 plots the CP-induced AE count rate dc_p/dN against the crack growth rate da/dN in the log-log scale for specimens S1–S5. Based on these data, the linear crack sizing model of the traditional method (see Table 4.5) was calibrated through regression analysis, as shown by the solid line. It can be seen that the majority of the data points are located within the 95% confidence bounds (dashed lines).

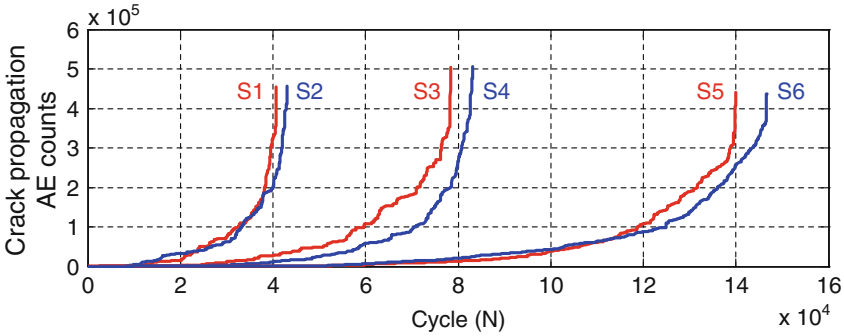

Fig. 4.16 Cumulative AE counts induced by CP for all the specimens

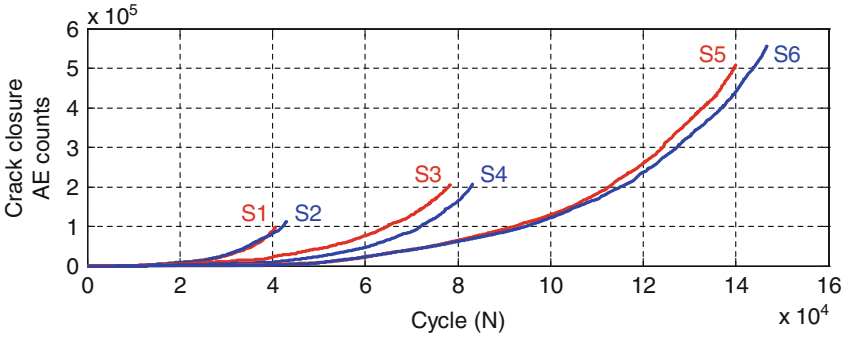

Fig. 4.17 Cumulative AE counts induced by CC for all the specimens

The results of the various specimens exhibited excellent agreement with each other despite the variations in their loading conditions. After removing the influence of CC through the AE wave classification process, a strong correlation between the CP-induced AE count rate and crack growth rate could be obtained, which is less divergent than those in other studies (Roberts and Talebzadeh 2003a; Yu et al. 2011). The results verify the effectiveness of the AE classification index proposed.

Validation of the traditional method was conducted by performing the crack sizing for specimen S6. Figure 4.19 shows the relationship between the CP-induced AE count rate and the crack growth rate in the log-log scale for specimens S6, along with the previously calibrated crack sizing model. It can be observed that the result also follows the linear trend. Figure 4.20 presents the estimated crack length (blue squares) versus the actual crack length measured by the COD gauge (blue crosses), where the crack length varies from about 1 to 11 mm (typically found in the stable propagation stage). Here, the integration computation for crack length estimation was done numerically using Simpson's rule. Figure 4.21 plots the absolute and relative errors of crack sizing at various crack lengths. It is demonstrated that, using

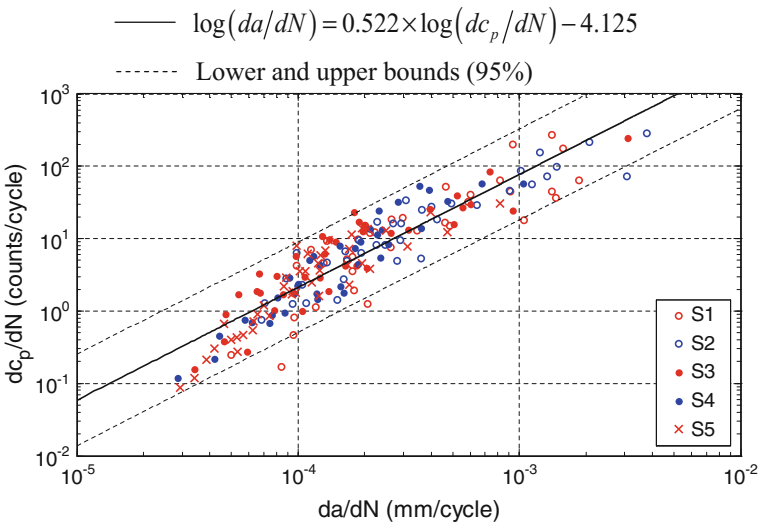

Fig. 4.18 Relationship of CP-induced AE count rate and crack growth rate for S1–S5

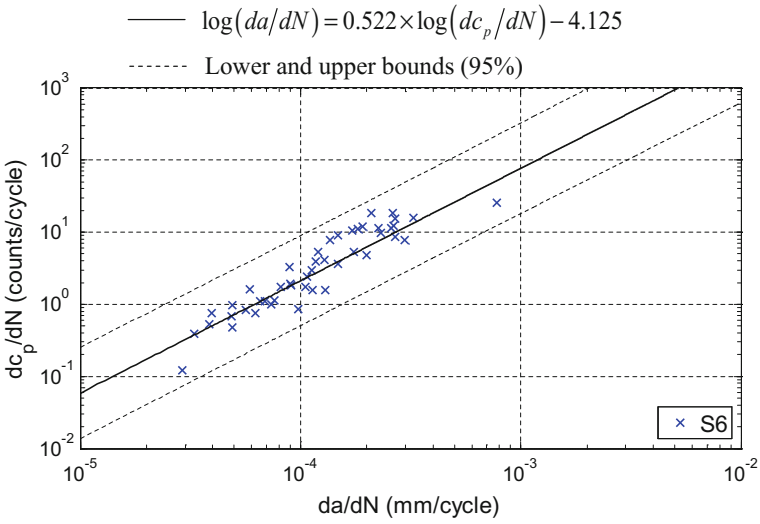

Fig. 4.19 Relationship of CP-induced AE count rate and crack growth rate for S6

the traditional crack sizing method together with the AE classification process proposed, the crack lengths (in the stable propagation stage) could be identified with absolute errors of less than 2 mm and relative errors of less than 20%.

As a summary, the CP-induced AE count rate reflects the dynamic crack extension, whereas the estimation of crack length depends on the integration of AE

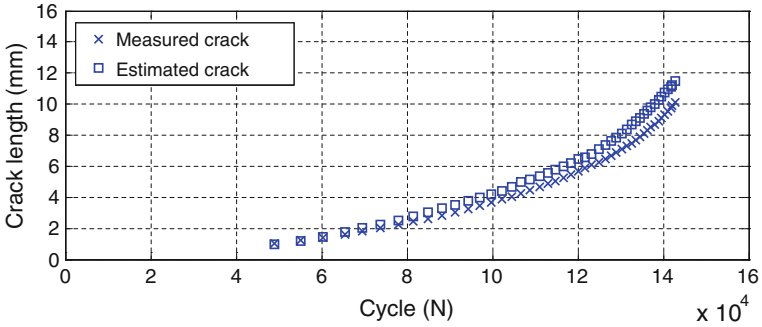

Fig. 4.20 Measured crack length versus estimated crack length using traditional method for S6

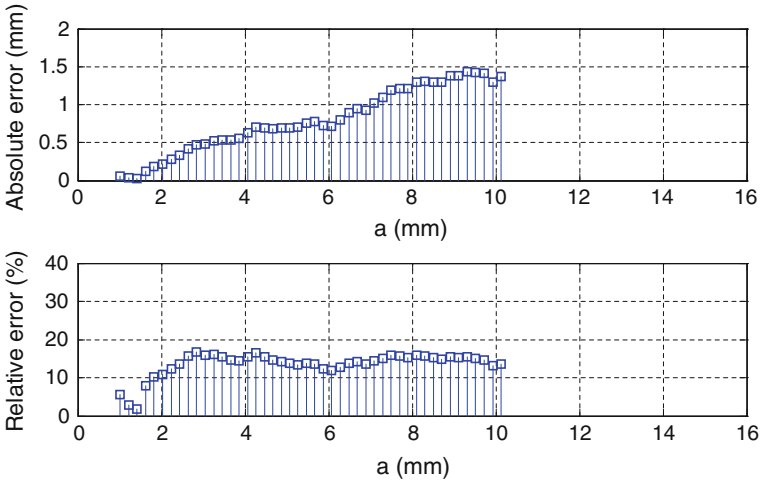

Fig. 4.21 Absolute and relative errors in crack sizing using traditional method for S6

data and the prior knowledge of initial crack length. In view of this, the traditional method could only be applied to newly-built structures with known initial crack states, but not to existing in-service structures with many potential cracks that are difficult to be calibrated. In addition, the method is only accurate for the stable propagation stage of crack growth, which further limits its applicability.

4.5.3 Crack Sizing Using the Novel Method

Figure 4.22 plots the CC-induced AE count rate dc_c/dN against crack length a for specimens S1–S5. Based on these data, the second-order crack sizing model of the

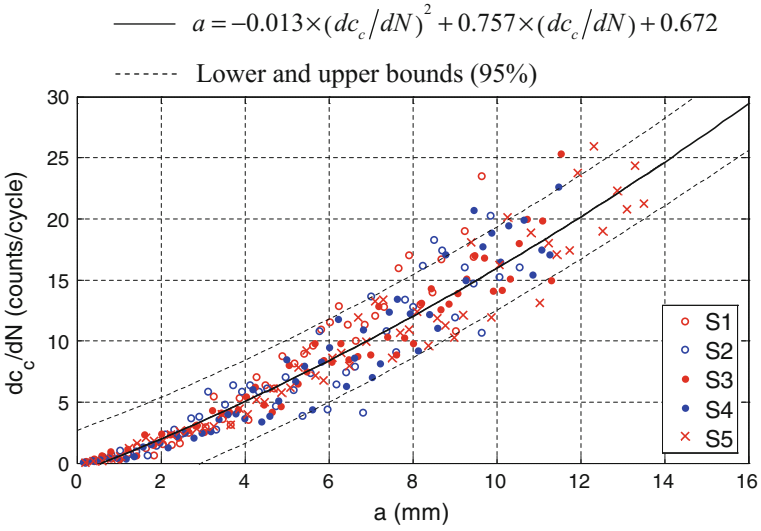

Fig. 4.22 Relationship of CC-induced AE count rate and crack length for S1–S5

proposed method was calibrated through the regression analysis, as shown by the solid curve. The majority of the data points are located within the 95% confidence bounds (dashed curves), although there are some outliers at crack lengths larger than 6 mm. As can be seen, the CC-induced AE count rate increases in tandem with the growth of the crack. The curve almost passes through the origin, implying that no CC-induced AE waves were generated prior to the presence of crack. As before, the results of different specimens exhibited excellent agreement with each other despite the differences in their loading conditions. It is evident that the variations of stress range and maximum stress level as well as the slight variation of load ratio have no significant influence on the crack sizing model used here (based on CC-induced AE waves), compared to the randomness of the AE data which can be observed for the series of specimens tested.

Validation of the method proposed was also conducted by performing the crack sizing for specimen S6. Figure 4.23 shows the relationship between the CC-induced AE count rate and crack length for specimens S6, along with the calibrated crack sizing model. It can be seen that the result also follows the second-order trend. Figure 4.24 presents the estimated crack length (blue squares) versus the actual crack length measured by the COD gauge (blue crosses), where the crack length varies from approximately 0 to 14 mm (throughout the fatigue life). Figure 4.25 plots the absolute and relative errors of crack sizing at various crack lengths. The results demonstrated that, using the novel crack sizing method together with the AE classification process proposed here, the majority of crack lengths could be identified with absolute errors of less than 2 mm and relative errors of less than 25%. It should be noted that the high relative errors observed from 0 to 2 mm are due to the small values of crack length at the denominator.

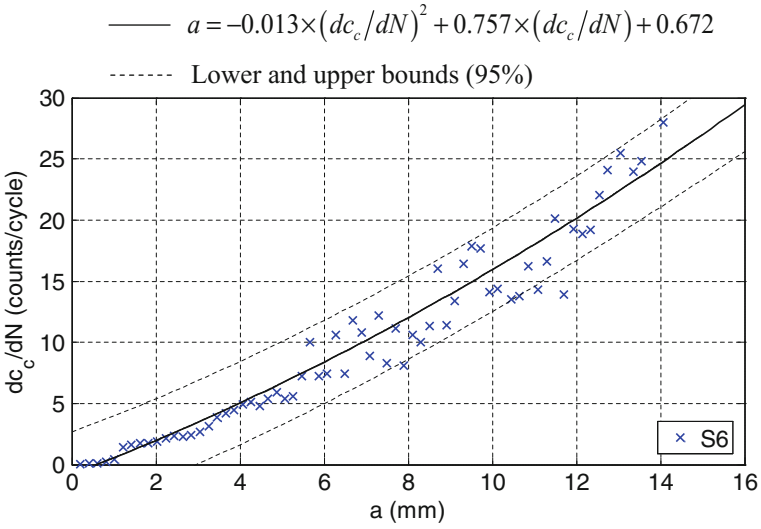

Fig. 4.23 Relationship of CC-induced AE count rate and crack length for S6

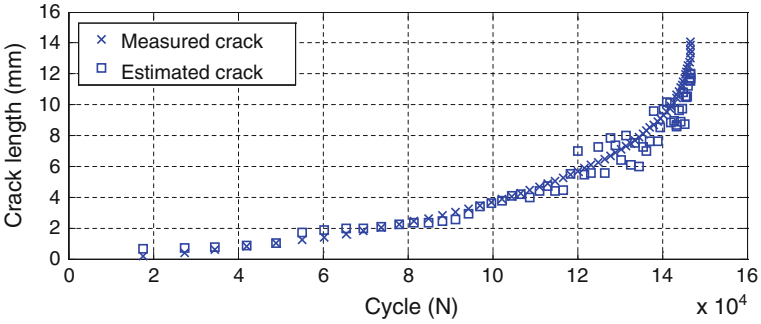

Fig. 4.24 Measured crack length versus estimated crack length using novel method for S6

As a summary, this section demonstrates that the CC-induced AE count rate can be correlated directly to the size of the fatigue crack. The method proposed does not depend on prior knowledge of initial crack length, integration of AE data or real-time load amplitude, allowing it to be applied to both new and existing structures. Additionally, this method applies to all the three stages of crack growth as long as the load ratio is sufficiently low to cause contact of the crack surfaces.

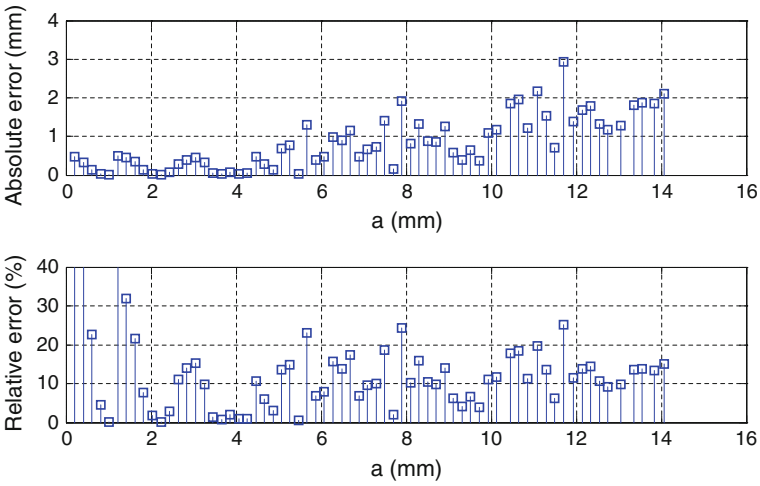

Fig. 4.25 Absolute and relative errors in crack sizing using novel method for S6

4.6 Concluding Remarks

This chapter focuses on the AE fatigue crack sizing in rail steel. A novel crack sizing method based on CC-induced AE waves is demonstrated. The main findings are summarized as below.

(1) In order to obtain fatigue cracks and related AE waves, three-point bending fatigue tests of different loading conditions were carried out on rail steel specimens in the laboratory. WT was utilized to investigate the time-frequency characteristics of the AE waves. The CP-induced AE waves were found to have different energy distribution in various frequency bands compared with the CC-induced counterparts.

(2) Since AE waves may be generated by either CP or CC processes during fatigue crack growth, the classification of these two types of AE waves is necessary as a pre-processing step to achieve a more reliable crack sizing result. A classification index based on WP was established to distinguish between the CP-induced and CC-induced AE waves. The threshold and frequency bands used for the classification were appropriately determined based on experimental data. Here, information embedded within the AE signal was used to perform the AE wave classification, which is preferred to the use of real-time load information, typically adopted in other studies. With the proposed approach, it renders the AE technique more amenable to practical implementation.

(3) Following the AE wave classification, the novel method proposed utilized the CC-induced AE waves to quantify the crack size. Here, a second-order correlation between the CC-induced AE count rate and the crack length was empirically derived from the AE data acquired during the fatigue tests of rail

steel specimens and subsequently used as the crack sizing model to estimate the crack length. Its performance was validated through the crack sizing of one specimen, and compared to that of the traditional crack sizing method based on CP-induced AE waves. The results showed clear evidence of the ability of the proposed method to quantify the crack length with good accuracy.

(4) In contrast with other AE crack sizing methods, the novel method proposed does not require prior knowledge of initial crack length, integration of AE data or real-time load amplitude to determine the crack length, allowing it to be applied to both new and existing structures. Although the novel method is limited to fatigue cracks under lower load ratios, this is nevertheless the prevailing condition for a large number of civil engineering structures including rail tracks. For future studies, the influence of specimen geometry, crack mode and fatigue load ratio on the generation of AE waves associated with CC can be investigated. An equivalent crack length or size could be studied for the cases of multiple cracks or irregular crack shapes (compared with through-thickness cracks). Besides, it is expected that the traditional and novel methods could be used together to complement each other leading to a more robust approach for crack sizing in rail track.

References

ASTM. (2013a). *E647-13a standard test method for measurement of fatigue crack growth rates*. West Conshohocken: ASTM International.

ASTM. (2013b). *E1820-13 standard test method for measurement of fracture toughness*. West Conshohocken: ASTM International.

Botev, Z. I., Grotowski, J. F., & Kroese, D. P. (2010). Kernel density estimation via diffusion. *The Annals of Statistics, 38*(5), 2916–2957.

Bowman, A. W., & Azzalini, A. (1997). *Applied smoothing techniques for data analysis*. New York: Oxford University Press.

Chang, H., Han, E. H., Wang, J. Q., & Ke, W. (2009). Acoustic emission study of fatigue crack closure of physical short and long cracks for aluminum alloy LY12CZ. *International Journal of Fatigue, 31*(3), 403–407.

Daniel, I. M., Luo, J. J., Sifniotopoulos, C. G., & Chun, H. J. (1998). Acoustic emission monitoring of fatigue damage in metals. *Nondestructive Testing and Evaluation, 14*(1–2), 71–87.

Esveld, C. (2001). *Modern railway track* (2nd ed.). Zaltbommel: MRT-Productions.

Gagar, D., Foote, P., & Irving, P. (2014). A novel closure based approach for fatigue crack length estimation using the acoustic emission technique in structural health monitoring applications. *Smart Materials and Structures, 23*(10), 105033.

Kohn, D. H., Ducheyne, P., & Awerbuch, J. (1992). Acoustic emission during fatigue of Ti-6Al-4V: Incipient fatigue crack detection limits and generalized data analysis methodology. *Journal of Materials Science, 27*(12), 3133–3142.

Li, D., Kuang, K. S. C., & Koh, C. G. (2015). Detection and quantification of fatigue cracks in rail steel using acoustic emission technique. In *Proceedings of the 10th International Workshop on Structural Health Monitoring*, pp. 2529–2536. Stanford, CA, USA.

Lindley, T. C., Palmer, I. G., & Richards, C. E. (1978). Acoustic emission monitoring of fatigue crack growth. *Materials Science and Engineering, 32*(1), 1–15.

Newman, J. J. C. (1984). A crack opening stress equation for fatigue crack growth. *International Journal of Fatigue, 24*(4), R131–R135.

Niri, E. D., & Salamone, S. (2012). A probabilistic framework for acoustic emission source localization in plate-like structures. *Smart Materials and Structures, 21*(3), 035009.

Paris, P. C., & Erdogan, F. (1963). A critical analysis of crack propagation laws. *Journal of Basic Engineering, 85*(4), 528–533.

Physical Acoustics Corporation. (2016b). WD wideband differential AE sensor. Retrieved from http://www.physicalacoustics.com/by-product/sensors/WD-100-900-kHz-Wideband-Differential-AE-Sensor.

Piotrkowski, R., Castro, E., & Gallego, A. (2009). Wavelet power, entropy and bispectrum applied to AE signals for damage identification and evaluation of corroded galvanized steel. *Mechanical Systems and Signal Processing, 23*(2), 432–445.

Rabiei, M., & Modarres, M. (2013). Quantitative methods for structural health management using in situ acoustic emission monitoring. *International Journal of Fatigue, 49,* 81–89.

Ritchie, R. O., & Suresh, S. (1982). Some considerations on fatigue crack closure at near-threshold stress intensities due to fracture surface morphology. *Metallurgical Transactions A, 13*(5), 937–940.

Roberts, T. M., & Talebzadeh, M. (2003a). Acoustic emission monitoring of fatigue crack propagation. *Journal of Constructional Steel Research, 59*(6), 695–712.

Roberts, T. M., & Talebzadeh, M. (2003b). Fatigue life prediction based on crack propagation and acoustic emission count rates. *Journal of Constructional Steel Research, 59*(6), 679–694.

Scruby, C. B. (1987). An introduction to acoustic emission. *Journal of Physics E: Scientific Instruments, 20*(8), 946.

Singh, P. J., Mukhopadhyay, C., Jayakumar, T., Mannan, S., & Raj, B. (2007). Understanding fatigue crack propagation in AISI 316 (N) weld using Elber's crack closure concept: Experimental results from GCMOD and acoustic emission techniques. *International Journal of Fatigue, 29*(12), 2170–2179.

Yu, J. G., Ziehl, P., Zrate, B., & Caicedo, J. (2011). Prediction of fatigue crack growth in steel bridge components using acoustic emission. *Journal of Constructional Steel Research, 67*(8), 1254–1260.

Chapter 5
Field Monitoring of Rail Cracks

Following encouraging results from the PLB test and fatigue tests performed under controlled conditions, the study was taken forward by deploying AE technique to monitor cracks in rail track in the field. Here, tests were carried out on actual rail tracks to acquire AE signals in the presence of high operational noise. In view of the noisy environment, the methodology for crack identification and location had to be improved. This chapter outlines the modifications and improvements in signal processing algorithms developed in this study to overcome the challenges encountered in field implementation.

5.1 Introduction

In open literature, the application of AE technique for damage detection in rail tracks is still limited to laboratory studies, and these include fatigue tests on rail steel specimens (Bassim et al. 1994; Kostryzhev et al. 2013) and studies performed on small-scale test rigs simulating wheel-rail interaction (Bruzelius and Mba 2004; Thakkar et al. 2010; Zhang et al. 2015). Field study is necessary in view of three important considerations.

(1) The SNR of AE signal obtained under field condition is likely to be very low due to the high operational noise. The AE waves induced by rail cracks are very weak especially at the incipient stage where crack growth is very slow. When the AE signals related to cracks are submerged in noise, the traditional defect detection method based on amplitude threshold becomes ineffective. To overcome this problem, advanced algorithms would be required in order to extract the crack-related AE features for further processing and interpretation.
(2) AE sources induced by real cracks under field environment may be different from those induced by artificial cracks generated in laboratory fatigue tests (with standard specimens, controlled loads and simple cracking modes). In

D. Li, *Rail Crack Monitoring Using Acoustic Emission Technique*,
Springer Theses, https://doi.org/10.1007/978-981-10-8348-8_5

addition, PLB sources widely used to simulate cracks in laboratory studies do not perfectly represents real cracks in signal intensity, frequency characteristics and dispersive features (Hamstad 2007). The performance of algorithms developed for crack detection under controlled environment in the laboratory could be significantly impaired when applied in the field.

(3) Various secondary AE waves are frequently encountered in the field. For instance, as a result of surface unevenness, wheels passing over RCF cracks could cause impacts resulting in multiple distinct AE transients. Although these AE waves can be utilized to detect the RCF cracks, these signals should be carefully identified and distinguished from those induced by crack propagation in order to achieve accurate crack identification.

It is commonly accepted that the wheel-rail interaction can be classified as rolling contact, which is similar to that of roller bearings. The typical failure mode of a roller bearing results from a localized defect that occurs when a sizable piece of material on the contact surface is dislodged during operation due to fatigue cracking under cyclic contact stress (Widner and Littmann 1976). Once a localized defect emerges in the inner or outer race of the bearing, an impact occurs every time the rolling element crosses the defected area. As a result, a high frequency AE burst is generated periodically due to elastic or plastic deformation of asperities, fracture of asperities or adhesion between asperities (Ferrando Chacon et al. 2015). There have been many studies on the subject of AE condition monitoring of roller bearings. Almost all the AE condition monitoring strategies for roller bearings proposed in the literature rely on the detection of such impact-induced AE bursts instead of CP-induced AE waves (Al-Dossary et al. 2009; Mba 2003; Tandon et al. 2007). However, for rail crack monitoring, these strategies based on impact-induced AE waves only applies to the surface cracks which are inevitably accompanied by material spalling or distortion at their later stages. CP-induced and CC-induced AE waves (as mentioned in Chap. 4) are important for detecting crack initiation and crack growth and for quantifying the crack size. In order to achieve a robust crack monitoring strategy for field application, it is of interest in this study to develop the method to be able to identify all of these AE waves in the presence of operational noise.

In a given situation, there is normally more than one degradation process that produces transient AE waves. For example, in fiber composite materials, AE waves result from the energy release of three failure modes, i.e. fiber breakage, interface debonding and matrix cracking (Ni and Iwamoto 2002; Wandowski et al. 2011); in the rail track, CP-induced, CC-induced and impact-induced AE waves are observed (Li et al. 2015). It is therefore necessary to distinguish different types of AE waves from each other in order to quantitatively analyze the AE signals and estimate the extent of the defects.

There are two main approaches for AE wave classification. One approach is to classify based on the time-frequency analysis where AE waves induced by different mechanisms would have different energy distribution over different frequency scales. For instance, Piotrkowski et al. (2009) identified several failure mechanisms

of corroded galvanized steel, using wavelet power, entropy and bispectrum; Khamedi et al. (2010) separated different failure micromechanisms in dual phase steels using wavelet packet analysis. The other approach is to classify using machine learning techniques, such as support vector machine (SVM) and artificial neural networks (ANNs), where different types of AE waves are clustered by intelligent algorithms. For instance, Widodo et al. (2009) employed relevance vector machine (RVM) and SVM in the fault diagnosis of a low speed bearing with various types of defects respectively on the inner race, outer race and rollers. Sause et al. (2012) proposed a pattern recognition approach based on an exhaustive screening to cluster AE signals originating from particular failure mechanisms of carbon fiber reinforced plastic specimens. Compared with the machine learning which functions like a black box, time-frequency analysis is explicit, easy-to-use and helpful in understanding the mechanisms of AE events. In this study, the time-frequency approach was chosen to classify different types of AE waves encountered in the field. It is worth noting that the time-frequency characteristics of AE waves obtained can also be used as input parameters for machine learning in future study (Gutkin et al. 2011; Marec et al. 2008).

In this chapter, the synchrosqueezed wavelet transform (SWT) is introduced to explore the time-frequency characteristics of AE waves originating from several mechanisms related to rail crack. The Tsallis synchrosqueezed wavelet entropy (TSWE) is then proposed as an index with time to identify the existence and location of RCF cracks in rail tracks in the field. To improve accuracy in crack monitoring, enhanced SWT scalogram is put forward to classify the multiple AE waves induced by the various mechanisms associated with rail crack. The performance of the proposed strategy (Fig. 5.1) is validated by a series of field tests with real rail cracks in the presence of high operational noise.

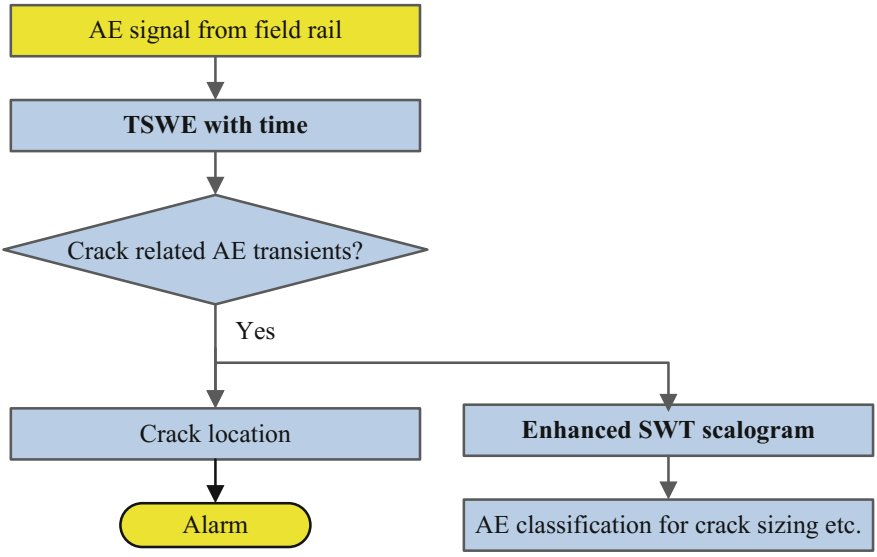

Fig. 5.1 Flowchart of the crack monitoring strategy proposed for field application

5.2 Experimental Procedure

5.2.1 Field Tests

Field tests were carried out on rail tracks with known rolling contact fatigue (RCF) cracks in Wuhan, China, in 2016. As mentioned in Sect. 2.1, the crack detection in field condition can be very complicated. A damage site with a known single RCF crack was finally determined for this quantitive study. Figure 5.2 shows the test site and experimental setup. The rail track used in the railway system was Chinese 60 kg/m rail, the cross-section and material of which are similar to UIC 60 used worldwide. Here, the rail track was supported by concrete sleepers and ballast. The distance between two rails was 1435 mm, and the distance between two adjacent sleepers was about 600 mm. As shown in Fig. 5.2e, the length of the crack is less than 40 mm and the depth of the crack is less than 2 mm. Based on the depth of the crack, this is considered an incipient RCF crack. The size of crack was confirmed by measurement using an ultrasonic instrument; however, the present experimental conditions limit us to accurately measure the crack size.

AE sensors were installed on the field side of rail head as it is the optimal position for crack detection in rail head as identified in the earlier PLB test described in Chap. 2. As shown in Figs. 5.2c–e and 5.3, three sensor locations were selected corresponding to three AE channels: Channel 1 (CH1) with AE sensor on the healthy rail used as the reference benchmark, Channel 2 (CH2) with AE sensor at 11.7 m away from the RCF crack, and Channel 3 (CH3) with AE sensor located at the same cross-section as the RCF crack.

The distance between CH2 and CH3 was set at 11.7 m, which was the length between the bogie centers of the freight train used in the tests. This was done to obtain the worst-case condition where the SNR level is expected to be the lowest. As illustrated in Fig. 5.4, three cases of different SNR levels could be encountered in the field according to the distances among the sensor, the crack, and the wheels. In case (a), the sensor is near the crack and the wheel that stimulates crack-related AE waves. Relative high crack-related AE waves and high rolling noise would be recorded. In case (b), the sensor is far away from the crack and the wheel that stimulates crack-related AE waves. Relative low crack-related AE waves and low noise would be recorded. In case (c), the sensor is far away from the crack and the wheel that stimulates crack-related AE waves as case (b), however, another wheel (of another bogie) is passing nearby the sensor. Relative low crack-related AE signal and high noise (introduced by the second wheel near the sensor) would be acquired, and the SNR level is thus the lowest. In this study, case (c) with the lowest SNR was considered in order to realize a robust crack detection strategy for field applications.

AE signals were collected during actual operation periods with trains operating in full service. The passenger trains have an axial load of about 17,000 kg and run at speeds of approximately 120 km/h, while the freight trains have an axial load of about 21,000 kg and travel at speeds of approximately 80 km/h. It is expected that the heavier the axial load, the higher the likelihood of damage to the tracks. The AE

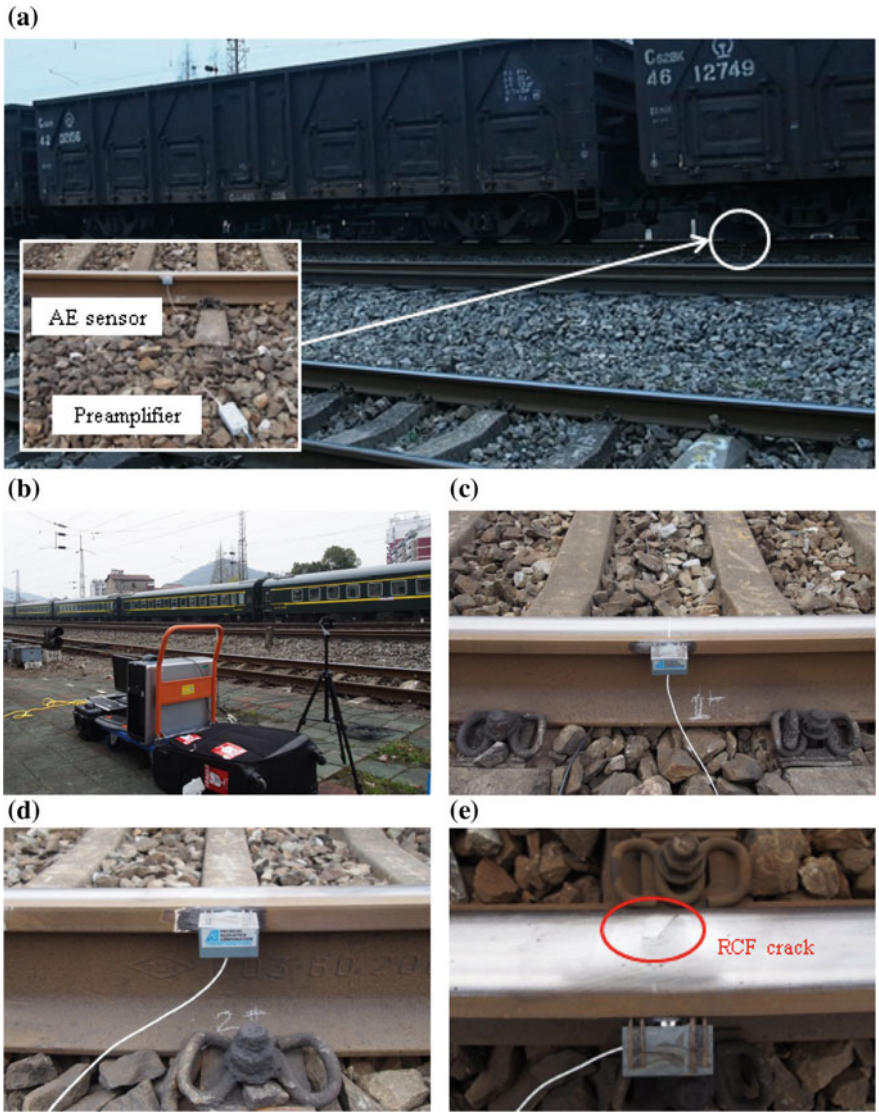

Fig. 5.2 Test site and experimental setup: **a** field site, **b** data acquisition instruments, **c** side view of CH1, **d** side view of CH2 and **e** top view of CH3

data of freight trains were thus collected and used in the analysis. Due to limited duration of access to the site, we could only carry out continuous monitoring over a set period. Although the crack growth could only be observed for a limited duration during the testing period, the field study provided a valuable opportunity to improve and validate the AE monitoring strategy adopted in this study for crack detection in rail track under field condition.

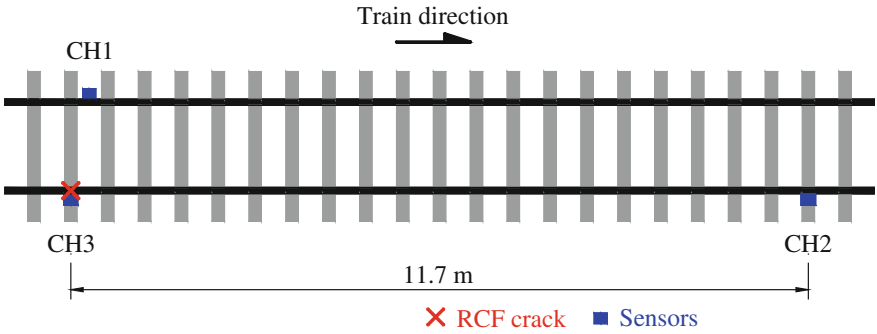

Fig. 5.3 Schematic of AE sensor layout

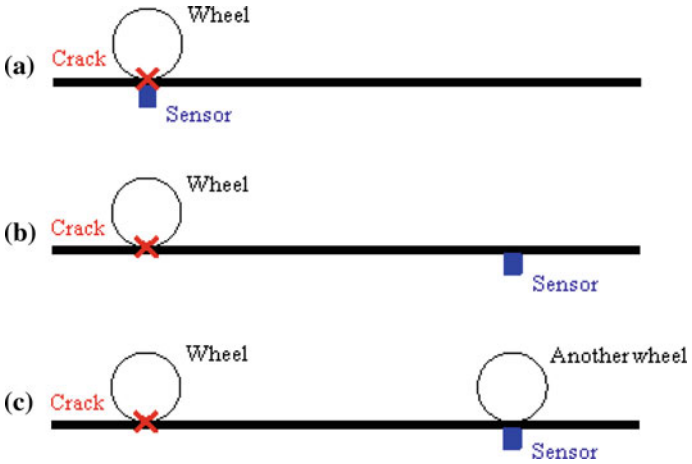

Fig. 5.4 Different cases of SNR for AE data acquisition: **a** the case with high crack AE and high noise, **b** the case with low crack AE and low noise and **c** the case with low crack AE and high noise

5.2.2 AE Data Acquisition

The AE signals were collected by a multi-channel Physical Acoustics (PAC) AE system. WD AE sensors were employed, which have a wide operating bandwidth of 125–1000 kHz with a resonant frequency of approximately 450 kHz. They have a flat frequency response over the operating bandwidth, which allows the study of the natural frequency characteristics of AE signals more accurately. Adhesive couplant was applied to ensure good contact between the sensor and the rail surface. Magnetic clamps were utilized to fix them in place. AE signals acquired by the sensors were amplified via preamplifiers (PAC 2/4/6) and finally recorded by a data acquisition board. For all the tests, the gain of preamplifier was set to 40 dB (referring to 1 μV at the sensor), and the sampling rate of 5 MHz was used. Initially, it was expected to acquire the AE signals over a wide frequency band in

order to ensure high signal fidelity over the frequency range of interest, as well as to identify any defects which might be associated with different characteristic frequency components. The analog band-pass filter was thus selected to be 100–1000 kHz during the test. Numerical filtering was subsequently applied during the signal processing.

5.3 Time-Frequency Representation of AE Waves

Wavelet analysis is a powerful tool to represent the non-stationary features of signals in the time-frequency domain. However, frequency aliasing and energy leakage can result in the continuous wavelet transform (CWT) of AE signals, which would further contaminate the time-frequency and non-stationary patterns associated with crack. As the AE signals collected in the field are already very noisy, a signal processing tool capable of representing the measured data more accurately in the time-frequency domain and further helping to denoise the data effectively is necessary. The synchrosqueezed wavelet transform (SWT) is thus introduced for this purpose.

5.3.1 Synchrosqueezed Wavelet Transform (SWT)

Synchrosqueezing was originally introduced in the context of analyzing auditory signals (Daubechies and Maes 1996). It is a special case of reallocation methods, which is aimed at sharpening a time-frequency representation of the original signal. The calculation procedure is briefly introduced here. The detailed derivation and the mathematical justifications could be found in (Daubechies et al. 2011; Thakur et al. 2013).

Recalling the definition of CWT of a signal $x(t)$:

$$WT(a,b) = \frac{1}{\sqrt{a}} \int_{-\infty}^{\infty} x(t)\psi^*\left(\frac{t-b}{a}\right)dt \tag{5.1}$$

where a is the scale parameter, b is the translation parameter, t is the time, $\psi(t)^*$ denotes the complex conjugate of wavelet function $\psi(t)$. For a mother wavelet $\psi(t)$ with its envelope fast decaying towards zero, its Fourier transform $\hat{\psi}(\xi) = (1/2\pi)\int_{-\infty}^{\infty}\psi(t)\exp(i\xi t)dt$ is concentrated around a certain positive frequency $\xi = \omega_0$, and more importantly $\hat{\psi}(\xi) = 0$ for $\xi < 0$.

For a purely harmonic signal $s(t) = A\cos(\omega_s t)$ (where ω_s is the angular frequency), the CWT of $s(t)$ with respect to $\psi(t)$ can be rewritten as:

$$\begin{aligned} WT_s(a,b) &= \frac{1}{2\pi}\int \hat{s}(\xi)a^{1/2}\hat{\psi}^*(a\xi)\exp(ib\xi)\mathrm{d}\xi \\ &= \frac{A}{4\pi}a^{1/2}\hat{\psi}^*(a\omega_s)\exp(ib\omega_s) \end{aligned} \tag{5.2}$$

The wavelet coefficients $WT_s(a,b)$ will concentrate around $a = \omega_0/\omega_s$, however, it will spread out over a region around the horizontal line on the time-scale plane. The CWT gives a somewhat "blurred" time-frequency representation. It is observed that although $WT_s(a,b)$ spread out in a, its oscillatory behavior in b points to the original frequency ω_s regardless of the value of a (Daubechies and Maes 1996). The candidate instantaneous angular frequency ω_s for the signal $s(t)$ can then be computed by

$$\omega_s(a,b) = -i[WT_s(a,b)]^{-1}\frac{\partial}{\partial b}[WT_s(a,b)] \tag{5.3}$$

For an arbitrary signal $x(t)$ containing multiple components, the angular frequencies $\omega(a,b)$ could be estimated by taking derivatives of the wavelet coefficients $|WT(a,b)| \neq 0$. In practice, the determination of the (a,b) pairs for which $|WT(a,b)| = 0$ is rather unstable, especially when $x(t)$ has been contaminated by noise. As a result, it is often more effective to consider a threshold T for $|WT(a,b)|$, below which $\omega(a,b)$ is not defined (Daubechies et al. 2011).

$$\omega(a,b) = \begin{cases} -i[WT(a,b)]^{-1}\frac{\partial}{\partial b}[WT(a,b)] & for\ |WT(a,b)| \geq T \\ \infty & for\ |WT(a,b)| < T \end{cases} \tag{5.4}$$

According to the above mapping $(a,b) \rightarrow (\omega(a,b),b)$, synchrosqueezing operation thus transfers the wavelet coefficients $WT(a,b)$ from time-scale plane to time-frequency plane.

If the frequency ω and the scale a are treated as continuous variables, the continuous form of SWT is defined as

$$SWT(\omega,b) = \int_{A(b)=\{a;\,|WT(a,b)|\geq T\}} WT(a,b)a^{-3/2}\delta(\omega(a,b)-\omega)\mathrm{d}a \tag{5.5}$$

where δ is the Dirac-delta function. The frequency in Hz could be obtained by $\omega/2\pi$. If the frequency variable ω and the scale variable a are discretized, $WT(a,b)$ would be computed only at discrete values a_j with $a_j - a_{j-1} = (\Delta a)_j$, and its synchrosqueezed transform $SWT(\omega,b)$ is likewise determined only at the centers ω_l of successive bins $[\omega_l - \Delta\omega/2,\ \omega_l + \Delta\omega/2]$ with $\Delta\omega = \omega_l - \omega_{l-1}$. The discrete form of SWT is defined as

$$SWT(\omega_l, b) = (\Delta\omega)^{-1} \sum_{a_j : \left|\omega\left(a_j, b\right) - \omega_l\right| \le \Delta\omega/2} WT\left(a_j, b\right) a_j^{-3/2} (\Delta a)_j \tag{5.6}$$

For efficient numerical implication, the CWT is sampled at locations $a_j = 2^{j/n_v}\Delta t$ with $j = 1, \ldots, Ln_v$, L is a non-negative integer and controls the largest scale value of interest, the number of voices n_v is a user-defined parameter that affects the number of scales (Goupillaud et al. 1984) and its value is recommended to be 32 or 64 for practical applications (Thakur et al. 2013). The value $n_v = 32$ is found to work well in this study. The discretized wavelet coefficients are then given with respect to $n_a = Ln_v$ log-scale samples of the scale a. The SWT finally becomes

$$SWT(\omega_l, b) = (\Delta\omega)^{-1} \sum_{a_j : \left|\omega\left(a_j, b\right) - \omega_l\right| \le \Delta\omega/2} WT\left(a_j, b\right) a_j^{-1/2} \frac{\log 2}{n_v} \tag{5.7}$$

Here, $\omega_l = 2^{l\Delta w}(n\Delta t)^{-1}$ $(l = 0, 1, \ldots, n_a - 1)$ for the signal $x(t)$ is discretized over an interval of length $n\Delta t$, where Δt is the discretization time period, n is the total number of discretization points and its $\log_2$ value should be a non-negative integer, and $\Delta\omega = (n_a - 1)^{-1}\log_2(n/2)$. Note that the time step Δt limits the range of frequencies that can be estimated. One form of the Nyquist sampling theorem shows that the maximum frequency is $\omega_{n_a - 1} = 1/2\Delta t$.

One of the advantages of SWT over other reassignment methods is the ability to perform signal manipulation (separation, reconstruction and denoising) (Auger et al. 2013). The inverse SWT for reconstructing the signal in the continuous form is

$$x(t) = \Re e\left[C_\psi^{-1} \int_0^\infty WT(a, b) a^{-3/2} \mathrm{d}a\right] \quad \text{with } C_\psi = \frac{1}{2}\int_0^\infty \hat{\psi}^*(\xi)\frac{\mathrm{d}\xi}{\xi} \tag{5.8}$$

where $\hat{\psi}(\xi)$ is the Fourier transform of mother wavelet $\psi(t)$. $\Re e[\cdot]$ returns the real part of the objective function. The inverse SWT in the discrete form is

$$\begin{aligned} x(t) &\approx \Re e\left[C_\psi^{-1} \sum_k WT(a_k, b) a_k^{-3/2} (\Delta a)_k\right] \\ &= \Re e\left[C_\psi^{-1} \sum_l SWT(\omega_l, b)(\Delta\omega)\right] \end{aligned} \tag{5.9}$$

The SWT has been applied to extract oscillatory components with time-varying frequency and amplitude in electrocardiogram signals (Daubechies et al. 2011), paleoclimate signals (Thakur et al. 2013), vibration signals of gearbox (Li and Liang 2012) and vibration signals of civil engineering structures (Liu et al. 2015;

Wang et al. 2013). For the application to AE signal in this study, the mother wavelet is selected to be a Bump wavelet by following the procedure illustrated in Sect. 3.3.2. Its function in frequency domain is

$$\hat{\psi}(\xi) \propto \exp\left(-\left(1-(2\pi\xi-\mu)^2\Big/\sigma^2\right)^{-1}\right) \tag{5.10}$$

where $\mu = 5$, $\sigma = 1$ and $\xi \in [\sigma(\mu-1), \sigma(\mu+1)]$ (Daubechies et al. 2011; Thakur et al. 2013; Wang et al. 2013).

5.3.2 Analysis of Example AE Waves

To demonstrate the effectiveness of the SWT and to compare its performance with the previously used CWT (Chaps. 3 and 4), several examples are presented here, including a numerical signal and several real measured AE signals. In order to demonstrate the results more clearly, the contour plots are used for both CWT and SWT. Figure 5.5 shows the waveform, theoretical instantaneous frequency trajectory, CWT plot and SWT plot of the numerical example. It is a frequency modulated (FM) signal composing two components around 7 and 10 Hz, respectively:

$$\begin{aligned} x(t) = {} & 1.7\sin(14\pi t + 3.6\sin(0.4\pi t)) \\ & + 1.8\sin(20\pi t + 3.2\sin(0.6\pi t)) \end{aligned} \tag{5.11}$$

In the CWT plot, the time-frequency representation of the signal spreads out around the real instantaneous frequency trajectory, which leads to spectral leakage and smearing between the two components. However, the SWT is able to delineate each individual component and resolve the instantaneous frequency close to the theoretical value. Importantly, the component around 10 Hz, considered as the dominant component of higher energy than that of the component around 7 Hz, is accurately represented in the SWT plot with more red colors.

Figures 5.6, 5.7, 5.8, 5.9, 5.10, 5.11, 5.12 and 5.13 show the time-frequency representations for real AE signals, related to PLB, crack propagation, crack closure, impact and field rolling noise, respectively, all of which involve complicated frequency components. It is obvious that SWT can give clearer time-frequency representations compared to CWT. For instance, the three dispersive modes of PLB-induced AE wave are better separated from each other in the SWT plot (Fig. 5.6d) than in the CWT plot (Fig. 5.6c). The two frequency bands [100–350] kHz and [400–650] kHz used for the classification index in Sect. 4.3 are more prominent in the SWT plots (Figs. 5.7d and 5.8d) than in the CWT plots (Figs. 5.7c and 5.8c). Detailed analysis of AE waves obtained from field tests (Figs. 5.9, 5.10, 5.11, 5.12 and 5.13) will be given in the following sections.

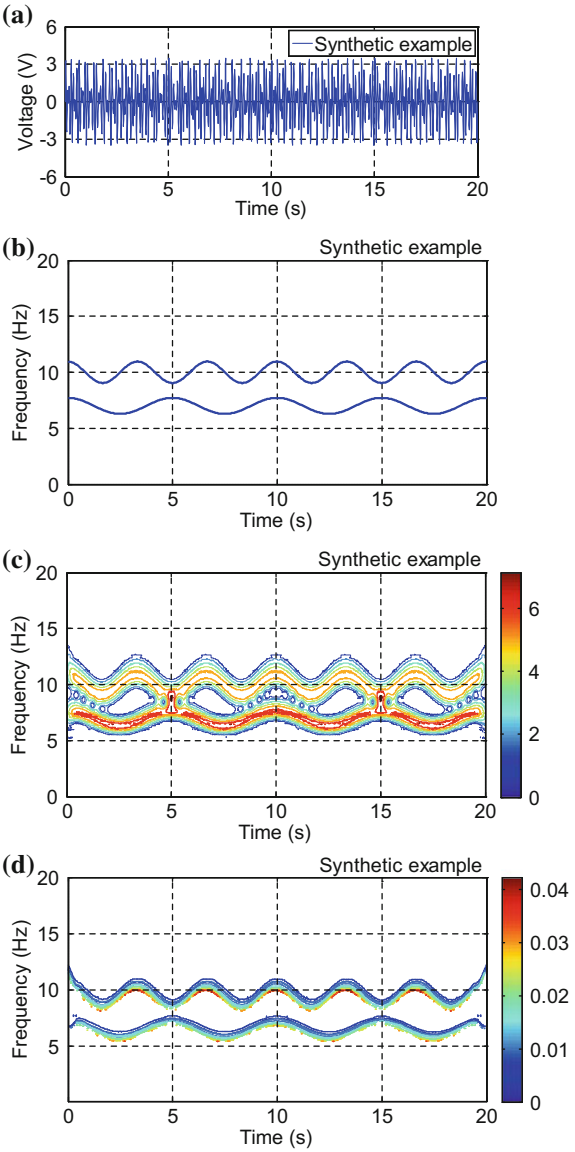

Fig. 5.5 Numerical example: **a** waveform, **b** real instantaneous frequency trajectory, **c** CWT plot and **d** SWT plot

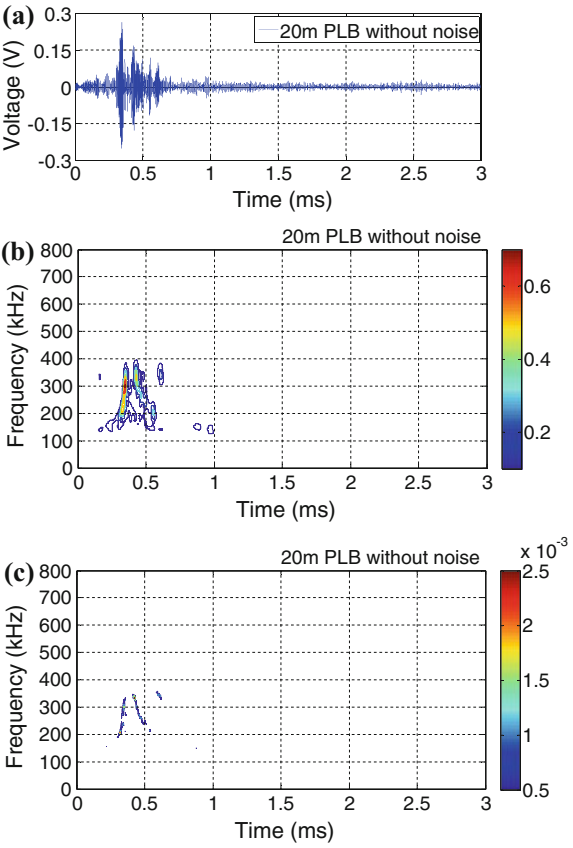

Fig. 5.6 PLB-induced AE wave with propagation distance of 20.0 m: **a** waveform, **b** CWT plot and **c** SWT plot

5.4 Crack Identification and Location Based on Time-Tsallis Synchrosqueezed Wavelet Entropy (TSWE)

AE waves induced by rail cracks exhibit significant non-stationarity and behave as impulsive transient disturbances in the recorded signals. However, they are likely to be overwhelmed by the operational noise in field environment. The rail crack monitoring strategy proposed for field application in this study is therefore based on a new kind of wavelet entropy that combines SWT and Tsallis entropy, namely Tsallis synchrosqueezed wavelet entropy (TSWE). The recently developed SWT is introduced to obtain clearer time-frequency representation of AE signals, and the Tsallis entropy is introduced to more accurately quantify the local variation of wavelet coefficients than the traditionally used Shannon entropy. TSWE is finally proposed as an index with time to identify and locate rail cracks from noisy AE signals.

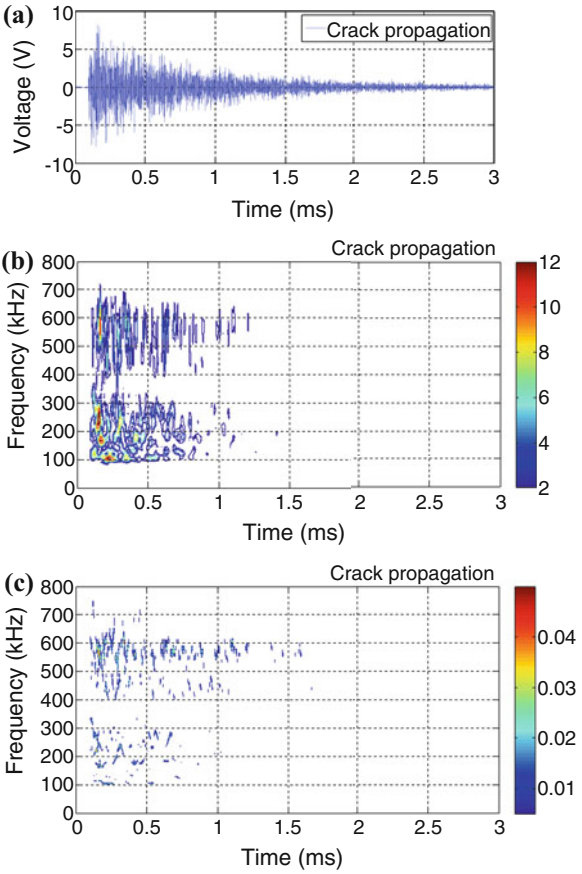

Fig. 5.7 CP-induced AE wave with a higher amplitude obtained from the laboratory fatigue tests: **a** waveform, **b** CWT plot and **c** SWT plot

5.4.1 Tsallis Entropy

Entropy is a kind of measurement of the complexity or uncertainty information of the signal or system. If the wavelet coefficient matrix is transformed into a series of probability distribution, the calculated entropy from this series reflects the sparseness degree of this wavelet coefficient matrix. Such entropy is called wavelet entropy, which is a kind of statistical index describing the energy distribution of wavelet coefficients (Cover and Thomas 2012), and is effective at quantitatively identifying local variation of non-stationary signals. The combination of wavelet and entropy can be used to determine the optimal mother wavelet if applied on the time-frequency plane, to select the representative frequency scales if applied along the frequency axis, and more importantly, to extract the defects-induced transient disturbances in low-SNR signals when applied along the time axis.

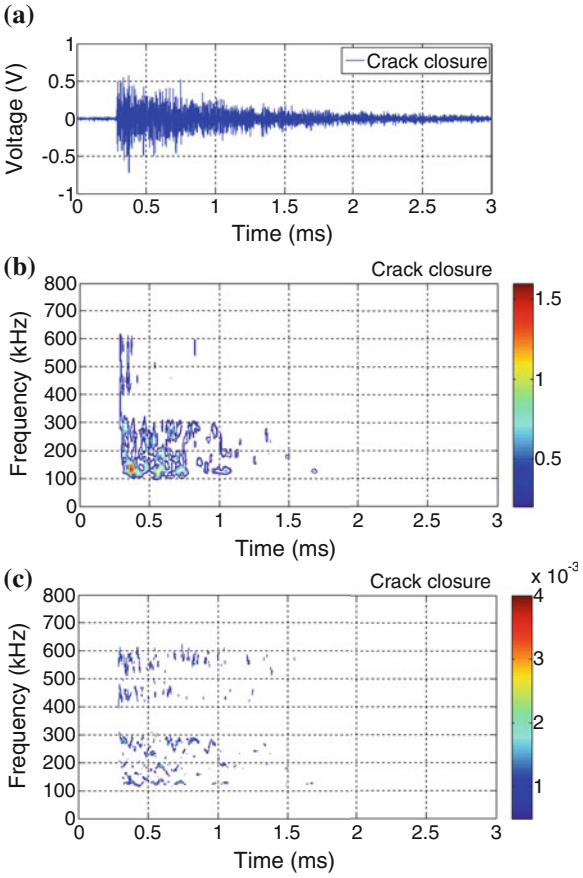

Fig. 5.8 CC-induced AE wave with a higher amplitude obtained from the laboratory fatigue tests: **a** waveform, **b** CWT plot and **c** SWT plot

Recently, Shannon wavelet entropy (SWE) has been proposed in the fault diagnosis of various structures using vibration, current and AE signals (Ekici et al. 2008; Ren and Sun 2008; Zhang et al. 2015). Shannon entropy is defined as (Shannon 1948)

$$E^S = -\sum_{i=1}^{I} p(i) \log p(i) \tag{5.12}$$

where I is the total number of possible configurations, $p(i)$ is the associated probabilities and $\sum_{i=1}^{I} p(i) = 1$. If $p(i) = 0$, $p(i) \log(i) = 0$. Shannon entropy is built based on Boltzmann-Gibbs (B-G) theory in thermodynamics. It belongs to the extensive entropy (B-G entropy) and only applies to extensive systems or data. The so-called "extensive entropy" is that when the system consists of two independent subsystems A and B, the system entropy satisfies the following additivity rule:

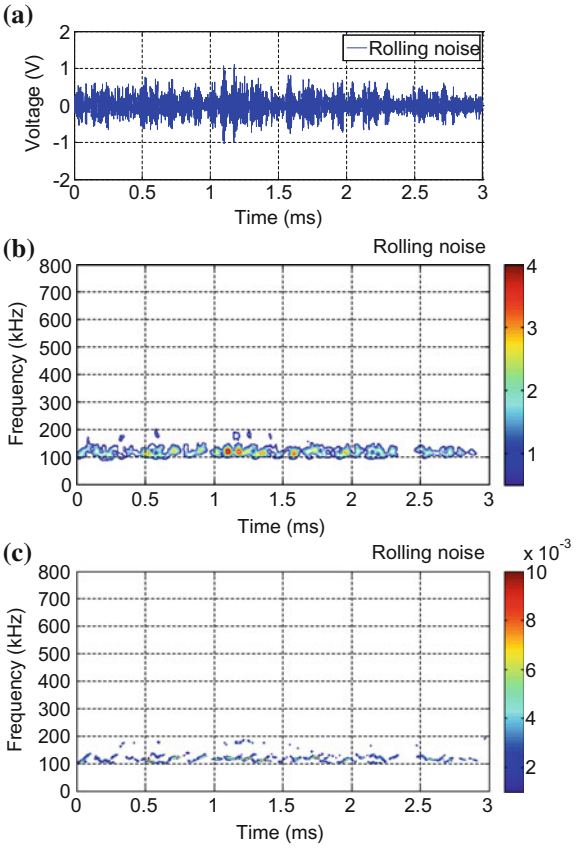

Fig. 5.9 Wheel-rail rolling noise obtained from the field tests: **a** waveform, **b** CWT plot and **c** SWT plot

$$\frac{E^S(A+B)}{k} = \frac{E^S(A)}{k} + \frac{E^S(B)}{k} \tag{5.13}$$

where the conventional constant k is typically taken to be the Boltzman constant for thermostatistical systems, or taken to be unity in information theory (Tsallis 1988, 2009).

However, many studies show the decomposition coefficients of signals are non-extensive, that is, does not satisfies the above additivity rule (Dong et al. 2013). For the wavelet coefficients of complicated AE signals, frequency aliasing and energy leakage could be produced (even when SWT is applied), which results in the loss of extensive property required for Shannon entropy (Liu et al. 2014). In the light of this, the Tsallis entropy is introduced to operate on the SWT coefficients of AE signals. Tsallis entropy belongs to the non-extensive entropy, and can be considered as the extension of the extensive entropy. It is able to explain some experimental phenomena that cannot be explained by the theory of extensive entropy, and owns additivity property for different subsystems that may have special correlations and interactions (Abe 1999; Tong et al. 2002; Tsallis et al. 1998).

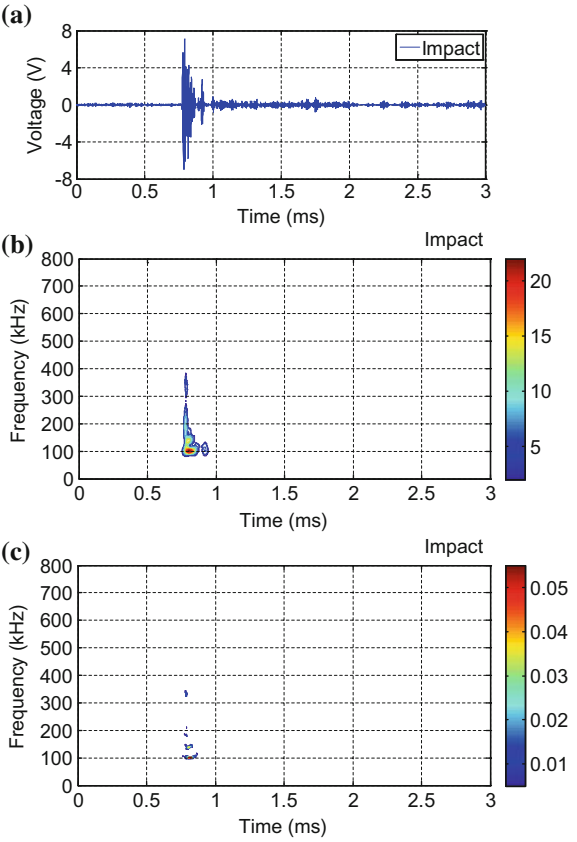

Fig. 5.10 Imapct-induced AE wave with a higher amplitude obtained from the field tests: **a** waveform, **b** CWT plot and **c** SWT plot

The expression of Tsallis entropy (Tsallis 1988) is

$$E^T = \frac{k}{q-1}\left(1 - \sum_{i=1}^{I} p(i)^q\right) = \frac{1}{q-1}\left(1 - \sum_{i=1}^{I} p(i)^q\right) \tag{5.14}$$

where q is the non-extensive parameter, I is the total number of possible configurations, $p(i)$ is the associated probabilities and $\sum_{i=1}^{I} p(i) = 1$. Alien from Shannon entropy, the parameter q is introduced to describe the non-extensive degree of the system in the following pseudo-additivity rule (Dong et al. 2013). When the system consists of two independent subsystems A and B, the system entropy satisfies

$$\frac{E^T(A+B)}{k} = \frac{E^T(A)}{k} + \frac{E^T(B)}{k} + (1-q)\frac{E^T(A)E^T(B)}{k^2} \tag{5.15}$$

Note that $q > 1$ and $q < 1$ correspond to sub-additivity and super-additivity of the system respectively. Indeed, as $q \to 1$, Tsallis entropy is equivalent to Shannon

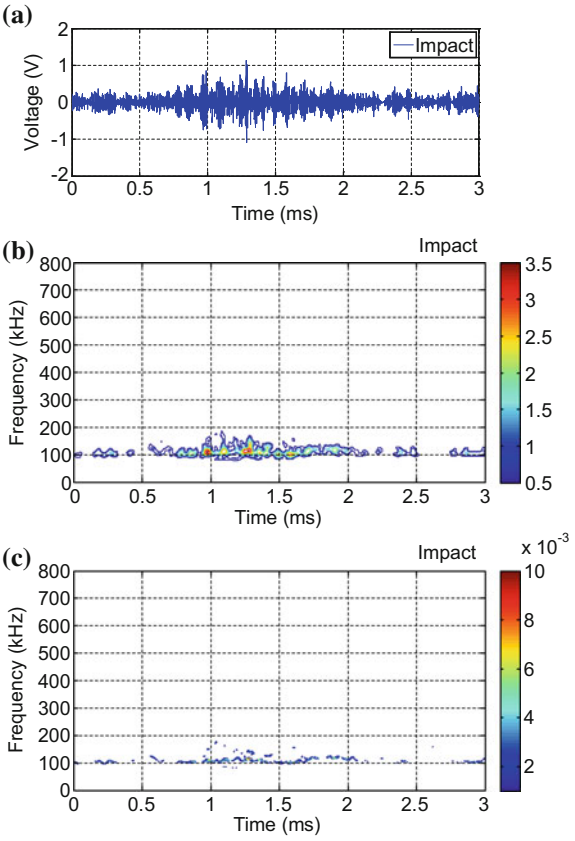

Fig. 5.11 Imapct-induced AE wave with a lower amplitude obtained from the field tests: **a** waveform, **b** CWT plot and **c** SWT plot

entropy defined in Eq. (5.12) (Tsallis 1988). For different systems, if the non-extensive parameter q is properly chosen for the calculation of Tsallis entropy, the information measurement of system can be flexibly and definitely expressed (Liu et al. 2014). In this study, the determination of q will be discussed in Sect. 5.4.3.

5.4.2 TSWE with Time

The Tsallis entropy of SWT coefficients, namely TSWE, is an information measurement to estimate the complexity of random signals. The crack-related transients bring a great deal of random and uncertain information to the AE signal, and change the corresponding TSWE values. TSWE is therefore employed in a time window sliding on the AE signal to locate the rail cracks in time and space. In a time window m, a set of synchrosqueezed wavelet coefficients are denoted as $\{swt(l,n)| = 1,2,\ldots,L;\ \ n = 1+m\delta, 2+m\delta,\ldots,N+m\delta\}$, where L is the total

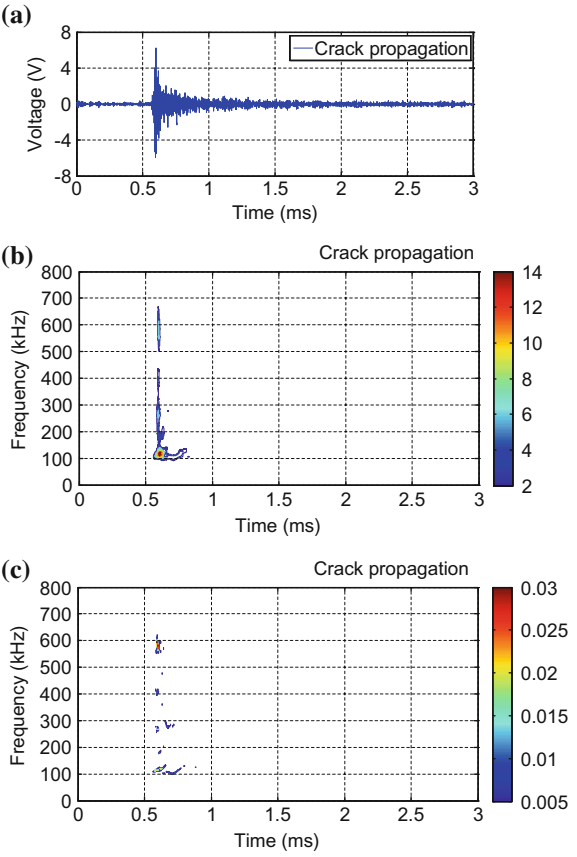

Fig. 5.12 CP-induced AE wave with a higher amplitude obtained from the field tests: **a** waveform, **b** CWT plot and **c** SWT plot

number of frequency scales of SWT, N is the total number of time instants in the time window, i.e. the length of time window, δ is the sliding interval of time window and $\delta = N/2$ is set in this study. The TSWE in the time window m is then defined as

$$E_{SWT}^{T}(m) = \frac{1}{q-1}\left(1 - \sum_{l=1}^{L}\sum_{n=1+m\delta}^{N+m\delta} p(l,n)^{q}\right) \tag{5.16}$$

where

$$p(l,n) = \frac{|swt(l,n)|^2}{\sum_{l=1}^{L}\sum_{n=1+m\delta}^{N+m\delta}|swt(l,n)|^2} \tag{5.17}$$

Here, $p(l,n)$ represents the energy probability distribution of wavelet coefficients, as defined above, and it is evident that $\sum_{l=1}^{L}\sum_{n=1+m\delta}^{N+m\delta} p(l,n) = 1$. The number of time window $m = 1, 2, \ldots, M$ with $M = (\bar{N} - N)/\delta$, where $\bar{N}$ is the

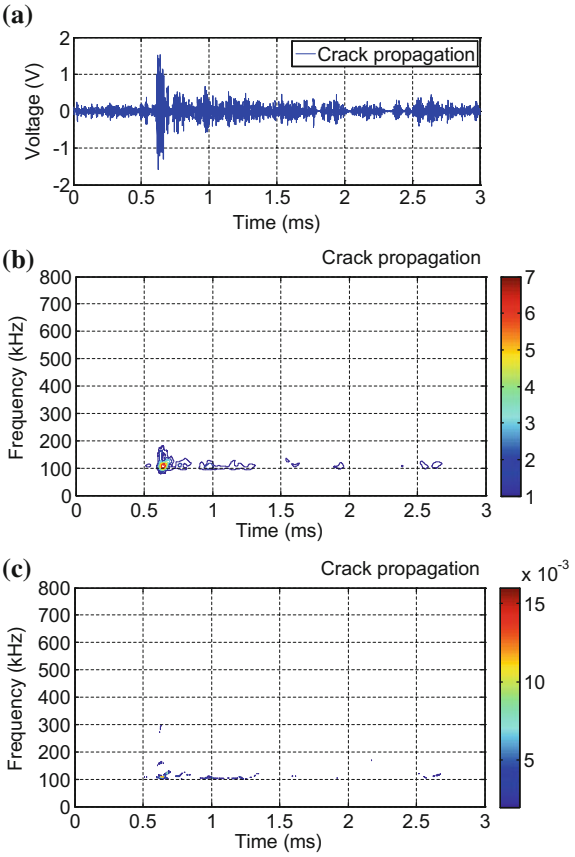

Fig. 5.13 CP-induced AE wave with a lower amplitude obtained from the field tests: **a** waveform, **b** CWT plot and **c** SWT plot

length of the whole signal to be analyzed. When m is changed from 1 to M, the time window slides over the whole signal, and the time-TSWE is then obtained. The schematic is shown in Fig. 5.14, where it is can be seen that the time resolution of time-TSWE is determined by the sliding interval δ.

After a proper non-extensive parameter q is adopted, TSWE well quantifies the time-frequency characteristics of AE signals. Low Tsallis entropy indicates high diversity of the wavelet matrix, corresponding to high energy concentration. If there is a crack-related AE transient in the time window analyzed, the distribution of signal energy will be more concentrated, and the TSWE will have a lower value compared to that of other time windows, where are background noise. When the time window slides over the whole AE signal, the onset of crack-related transient can be identified based on the variation of entropy values along the time, i.e. time-TSWE. The crack can then be located along the rail by using the arrival times of an individual AE transient at two neighboring sensors. It should be noted that this time-TSWE based strategy is not limited to crack monitoring in rail head since it does not rely on the dispersion properties of AE waves.

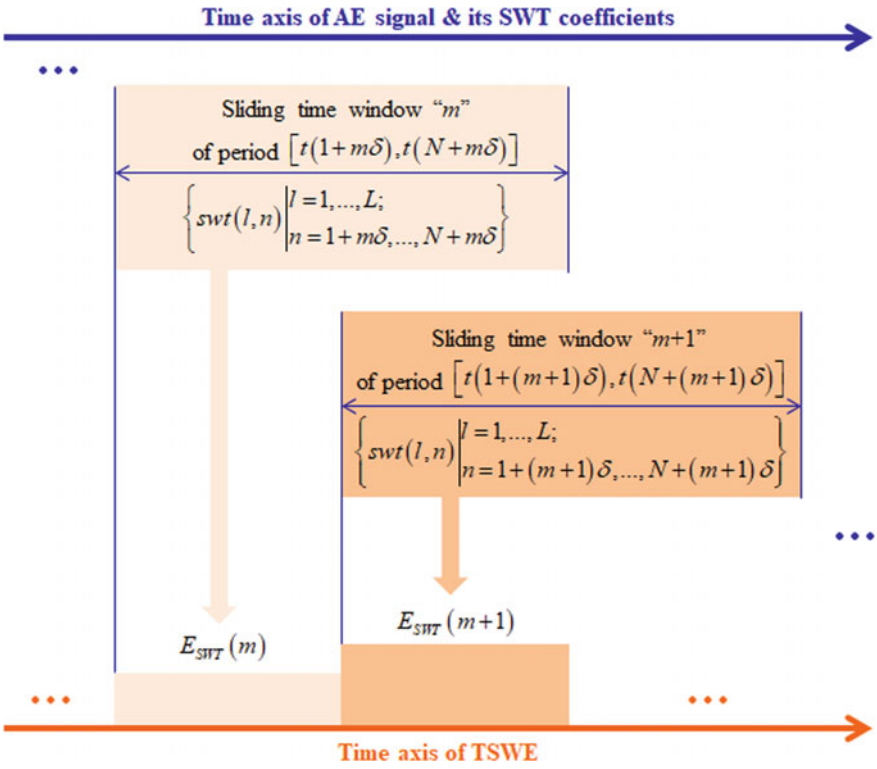

Fig. 5.14 Schematic of time-TSWE

5.4.3 Determination of Parameters in TSWE

Before the detection plan based on TSWE is implemented, some parameters that influence the detection performance should be appropriately determined, including characteristic frequency band, non-extensive parameter, time window length and wavelet filtering threshold. There will be discussed below:

(1) Characteristic frequency band

In order to improve the accuracy of crack detection, a suitable frequency band is selected for the calculation of TSWE after investigating the characteristic frequencies of crack and that of noise in the AE waves, respectively. As shown in Fig. 5.9, the operational noise caused by passing trains has energy concentration predominantly below 200 kH. It is observed to be the same case in field conditions where trains of different speeds and axial loads operate. Despite the vast differences in amplitudes of the corresponding AE signals, this observation holds true. It is concluded that in the site where the AE signals are collected (i.e. at the wheel-rail contact point or at some distance away), the frequency of the noise is mainly limited

to below 200 kHz. This is similar to the findings reported in reference (Zhang et al. 2015). This may not be surprising since the main source of noise comes from the mechanical interaction between wheel and rail, which is typically of the lower frequency band.

Several types of crack-related AE signals, i.e. CP-induced AE waves, CC-induced AE waves, impact-induced AE waves, were obtained under laboratory as well as field conditions. The SWT results of these AE waves obtained from both laboratory fatigue tests and field tests are exhibited respectively in Figs. 5.7, 5.8, 5.10, 5.11, 5.12 and 5.13. It is clear that all these crack-related signals have energy distributing below 200 kHz, which overlaps that of the noise. In fact, the impact-induced and crack propagation-induced AE waves from the field tests were inherently disturbed by operational noise. However, all these crack-related signals also have distinct energy contents clustering in the frequency band from 200 to 700 kHz, which are several times higher than that of the noise. Therefore, the frequency band [200–700] kHz is selected as the characteristic frequency band of interest and only SWT coefficients within this band are utilized in the calculation of TSWE in order to extract the AE signal features for crack monitoring. The function of such a characteristic frequency band is the same as the filtering based noise cancellation method proposed in Sect. 3.6.

(2) Non-extensive parameter

In order to determine a proper non-extensive parameter q for the AE signals to be analyzed and to better support the necessity of using Tsallis entropy instead of Shannon entropy (which is equivalent to $q = 1.0$), a comparison between different values of q was made based on the definition of additivity and pseudo-additivity, as specified in Eqs. (5.13) and (5.15) respectively (Dong et al. 2013). Two frequency sub-bands, [200–350] kHz and [350–700] kHz, were taken as two subsystems of the characteristic frequency band [200–700] kHz. This is because that the energy of AE signals originating from the rail cracks is mainly distributed in these two frequency bands and that the mechanisms of AE signals can be distinguished based on their different energy distribution in these two representative frequency sub-bands (see Figs. 5.27, 5.28, 5.29, 5.30 and 5.31 in Sect. 5.5). Following that, the entropy from the characteristic frequency band E was compared with the sum of the entropies from frequency sub-bands E_{sum}. The smaller the error, which was defined as $(|E_{sum} - E|/E) \times 100\%$, the more accurate the value of q, which is finally determined to be 1.3 in this study by trial-and-error.

Take an AE signal collected at the RCF crack as an example, for which the results of Shannon entropy ($q = 1.0$) and Tsallis entropy ($q = 1.3$) are illustrated here. It can be seen from Fig. 5.15 that the sum of Shannon entropies from frequency sub-bands deviates substantially from the Shannon entropy of the characteristic frequency band as a whole. The error is shown to be as large as 100%. It is clear that the results of Shannon entropy do not satisfy the principle of the extension entropy here. Tsallis entropy was then applied to analyze the same AE signal. As can be seen in Fig. 5.16, the error between the Tsallis entropy of the whole characteristic frequency

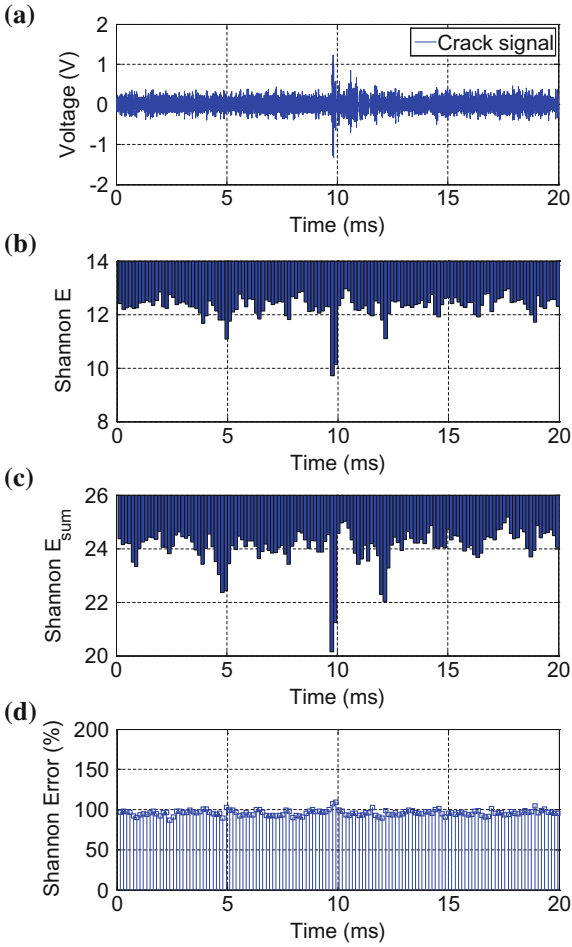

Fig. 5.15 Comparison results of Shannon wavelet entropy: **a** waveform, **b** Shannon entropy of the whole characteristic frequency band, **c** sum of Shannon entropies from frequency sub-bands and **d** relative error

band and the sum of Tsallis entropies from frequency sub-bands is less than 7% and that the disturbance induced by the crack is more obvious. Thus, the Tsallis entropy with $q = 1.3$ will be applied in the following analysis.

(3) Length of time window

The length of time window determines the time resolution (or space resolution) in the rail crack location. The smaller the window length (as well as the sliding interval of time window), the higher the time resolution. However, the operational noise will significantly influence the wavelet entropy of AE signal in a small window. If the time window is too small, the calculated entropy from the noise would fall into a similar level of that obtained from crack-related AE signals due to the local energy concentration, leading to false identification of cracks. On the other hand, a longer time window renders a smaller standard deviation of AE signal

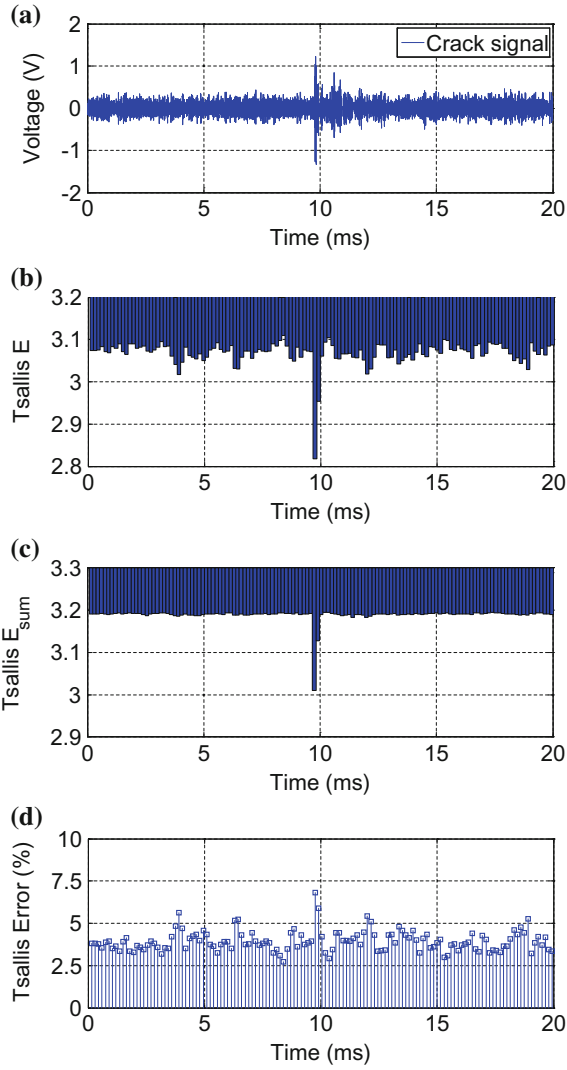

Fig. 5.16 Comparison results of Tsallis wavelet entropy: **a** waveform, **b** Tsallis entropy of the whole characteristic frequency band, **c** sum of Tsallis entropies from frequency sub-bands and **d** relative error

which helps to suppress the noise interference (Zhang et al. 2015). However, if the time window is too long, it does not only lead to lower time resolution but also easily miss crack-related AE transients of weak energy due to the average effect in the time window. Therefore, a tradeoff should be made between the time resolution and the noise suppression.

The length of time window is carefully determined based on the actual AE signals acquired during the field tests. As an illustration, Fig. 5.17 presents the previous AE signal (as shown in Figs. 5.15 and 5.16) and the corresponding time-TSWE with different lengths of time window, respectively 100, 200 and 300 μs. Comparing Fig. 5.17b–d, the crack detection performance of TSWE is

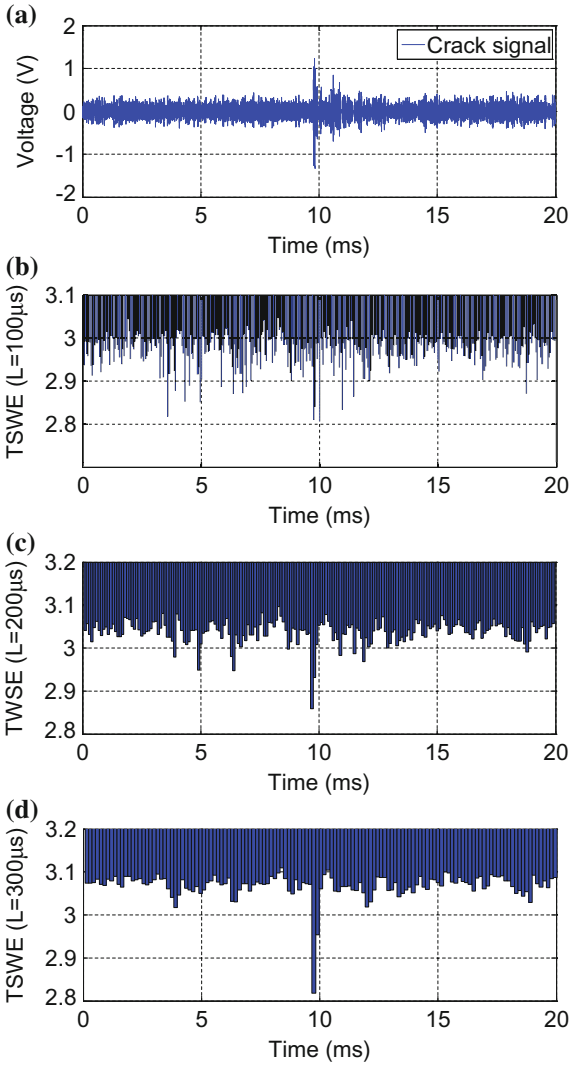

Fig. 5.17 TSWE of an crack signal with different lengths of time window: **a** waveform, **b** TSWE with time window of 100 μs, **c** TSWE with time window of 200 μs and **d** TSWE with time window of 300 μs

significantly affected by the operational noise when the length of time window is 100 μs. The main reason for the observed interference is the higher fluctuation and larger standard deviation of the entropy of noise. This results in the concentrated energy distribution in a small time window, leading to smaller values of the Tsallis wavelet entropy and the false detection of defects (Zhang et al. 2015). As the length of time window becomes longer, e.g. 200 and 300 μs, crack features become more distinct and could be distinguished from operational noise because the probability of concentrated energy distribution of noise is markedly reduced in longer time window. Meanwhile, it is worth noting that the mean value of the Tsallis entropy becomes slightly larger as the length of time window increases due to the definition

of the entropy. The alert threshold for crack detection should be discussed after the time window has been fixed. Finally, the time window length is determined to be 300 μs in this study in order to suppress the noise effects and to ensure the appropriate time resolution.

(4) Threshold of SWT

The hard wavelet threshold T helps to further suppress the influence of noise, which has energy spreading in the characteristic frequency band. The asymptotically optical threshold proposed by Donoho (1994) is the most popular of all threshold values. It is expressed as:

$$T = \sqrt{2\log N} \times \sigma = 1.4826 \times \sqrt{2\log N} \times MAD(|WT(i,j)|) \tag{5.18}$$

Here, N is the number of time instants and σ^2 is the noise power that can be estimated from the median absolute deviation (MAD) of the wavelet coefficients in the frequency band of interest (Thakur et al. 2013). In this study, the threshold was calculated using the wavelet coefficients of operational noise induced AE signal, which was collected by the reference channel on the healthy rail. For the TSWE with time window of 300 μs, the threshold value is determined to be $3.0e^{-4}$, which was employed to filter the noise interferences in the subsequent SWT and Tsallis entropy. Based on this threshold, crack-related features can be extracted more accurately and the noise interferences in the crack detection are greatly suppressed.

5.4.4 Results and Discussion

The results of field tests for crack identification and location using TSWE with time are presented and discussed in this section.

(1) Crack identification

The AE signal collected on the cracked rail involved numerous transient disturbances. Some of the transients had amplitudes higher than that of the operational noise, while some of them were submerged in the noise. The majority of these transients were induced by the impacts that happened when the wheel passed over the uneven surfaces at the RCF crack site. Since the actual rail crack grows very slowly, CP-induced AE transients were seldom observed at this stage of crack growth. The amplitude of impact-induced AE transients varies considerably from about 1.0–8.0 V due to the influence of complicated loading conditions and the attenuation of AE signal propagating in the rail track. Using the pre-determined parameters discussed previously, the time-TSWE exhibited excellent performance in identifying the rail crack identification in the field. This is remarkable in view of the fact that the crack-related AE transients were submerged in high operational noise. The TSWE results of selected AE signals are given in Figs. 5.18, 5.19, 5.20, 5.21, 5.22, 5.23, 5.24 and 5.25.

Firstly, as the benchmark, Fig. 5.18 exhibits the waveform and corresponding TSWE of AE signal recorded from the healthy rail (CH1). The whole signal lasts

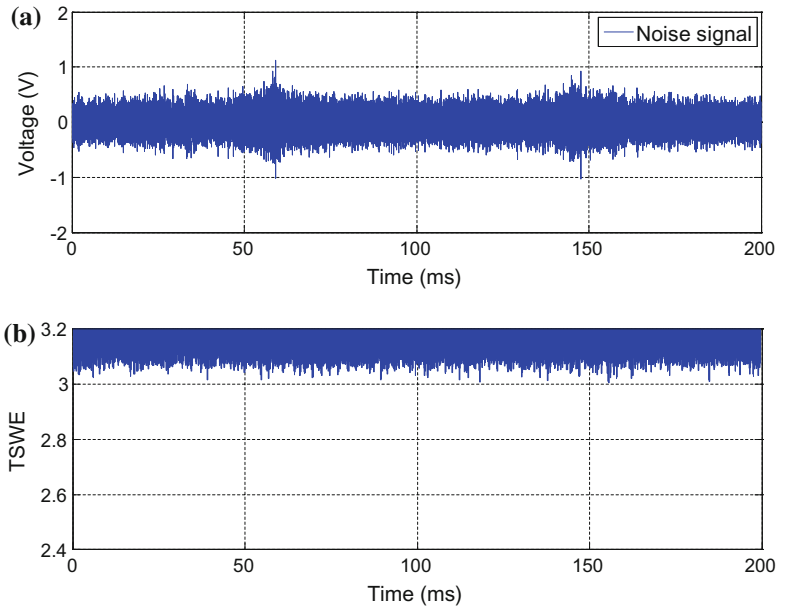

Fig. 5.18 Operational noise recorded by the reference channel (CH1): **a** waveform and **b** TSWE

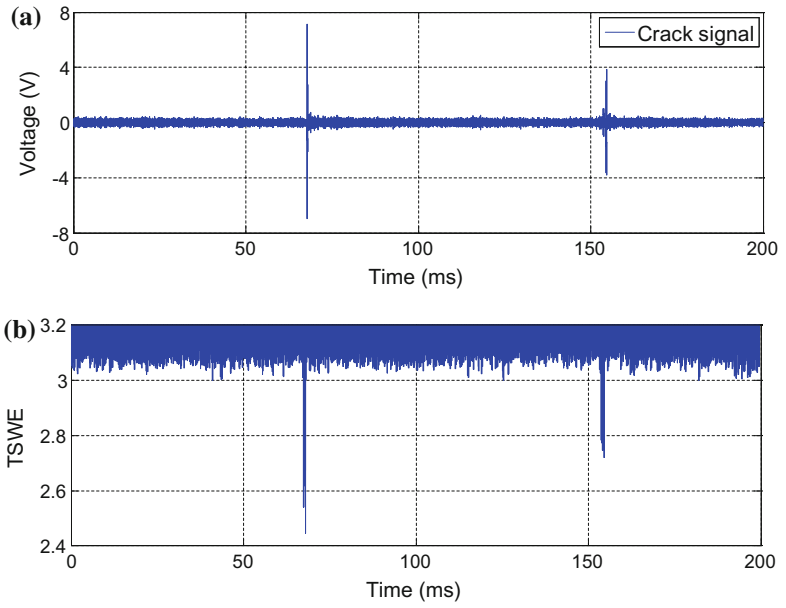

Fig. 5.19 Impact-induced AE signal with higher amplitudes recorded by the channel near the crack (CH3): **a** waveform and **b** TSWE

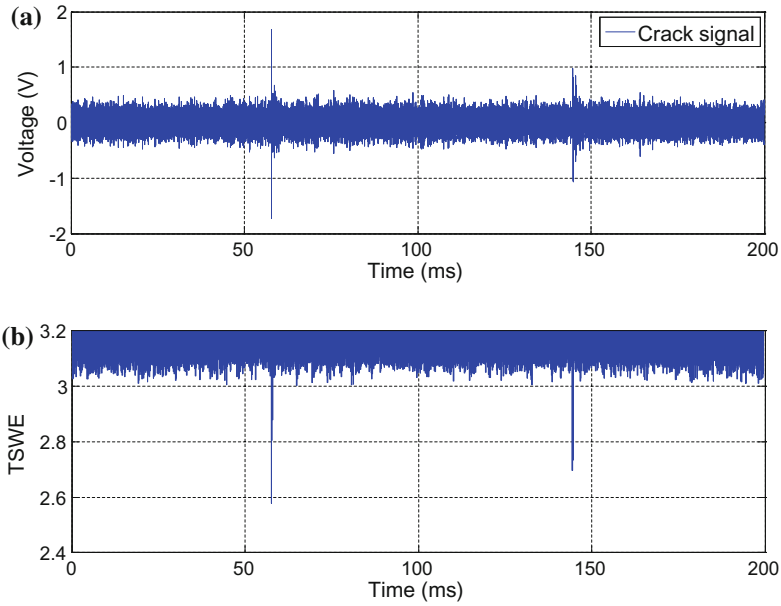

Fig. 5.20 Impact-induced AE signal with higher amplitudes recorded by the channel far away from the crack (CH2): **a** waveform and **b** TSWE

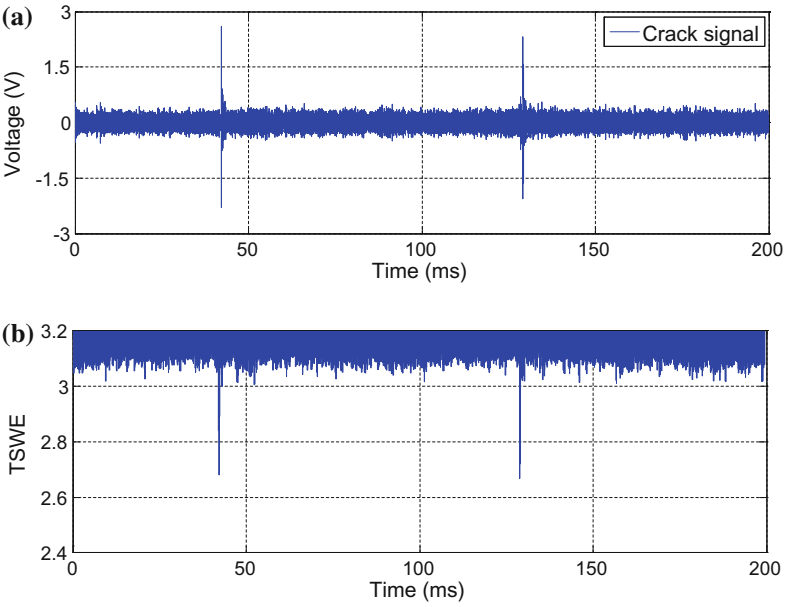

Fig. 5.21 Impact-induced AE signal with lower amplidues recorded by the channel near the crack (CH3): **a** waveform and **b** TSWE

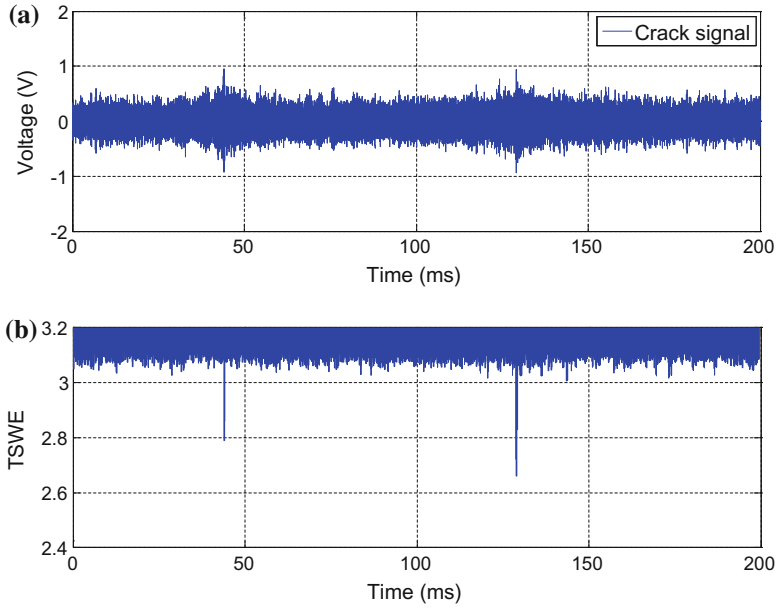

Fig. 5.22 Impact-induced AE signal with lower amplitudes recorded by the channel far away from the crack (CH2): **a** waveform and **b** TSWE

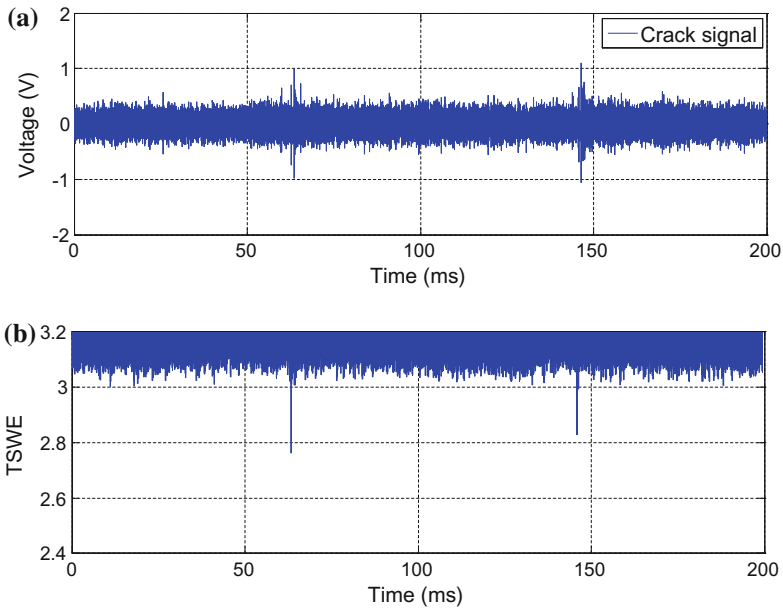

Fig. 5.23 Another impact-induced AE signal with lower amplitudes recorded by the channel far away from the crack (CH2): **a** waveform and **b** TSWE

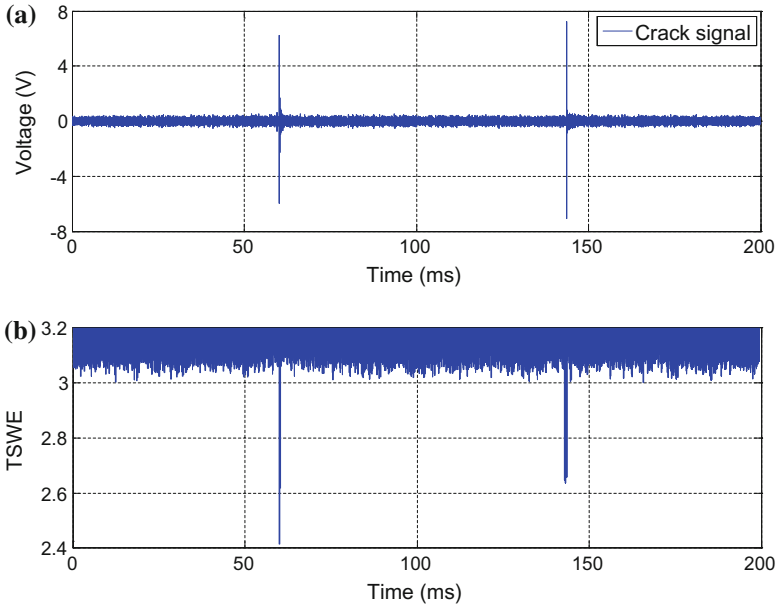

Fig. 5.24 CP-induced AE signal recorded by the channel near the crack (CH3): **a** waveform and **b** TSWE

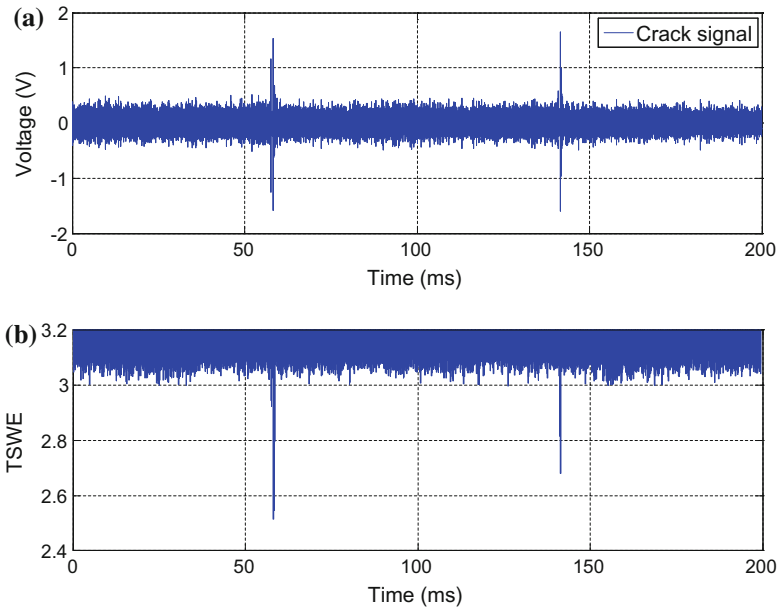

Fig. 5.25 CP-induced AE signal recorded by the channel far away from the crack (CH2): **a** waveform and **b** TSWE

200 ms which was sufficiently long to cover the transit time of one bogie with two axles (wheels). It can be seen that the waveform amplitude of operational noise induced mainly by the wheel-rail rolling contact could reach as high as 1.0 V. Two local maxima were reached when the two wheels pass by the same rail cross-section respectively where the AE sensor was installed. As expected, the corresponding TSWE did not fluctuate much at the waveform maxima of noise. All the TSWE values of operational noise obtained were found to be above 3.0 when no crack was present.

Secondly, Figs. 5.19 and 5.20 show an impact-induced AE signal with higher amplitudes recorded by the AE channel near the RCF crack (CH3) and the AE channel at 11.7 m away from the RCF crack (CH2), respectively. Here, the two distinct transients were caused by the two axles when they passed the RCF crack. After the impact transients were generated at the crack, their energy dissipated rapidly when they reached the sensor location at 11.7 m away. For the AE signals recorded by both channels, the value of TSWE decreased dramatically at the occurrence of impact-induced AE transients.

Thirdly, Figs. 5.21 and 5.22 display an impact-induced AE signal with lower amplitudes recorded by the AE channel near the RCF crack (CH3) and the AE channel at 11.7 m away from the RCF crack (CH2), respectively. TSWE was still able to identify the impulsive AE disturbances as clearly shown in the figures. The results are highly encouraging in view of the fact that CH2 was far away from the crack (Fig. 5.22), and despite the fact that the impact-induced transients were completely submerged in the operational noise. It is concluded that the proposed time-TSWE can effectively identify the existence of rail cracks by decreasing below 3.0.

It was found that the many of AE signals collected in the field, especially by CH2, are of very low SNRs. To further validate the performance of proposed strategy, one more example of low SNR is given in Fig. 5.23. The waveform of AE signal had a similar level of amplitudes (about 1.0 V) as the rolling noise shown in Fig. 5.18, while the results of TSWE indicated the existence of two crack-related transients which were submerged in the waveform. For the AE results of CH2, it should be noted that the local minima of TSWE (which were caused by the impulsive AE transients generated by the bogie near the crack) might not be always coincident with the two maxima of the AE waveform (which were generated by another bogie near the sensor, as shown in Fig. 5.4), adding to the complexity of the signal. It is due to random variation of the length between the bogie centers from the design value, i.e. 11.7 m. This further highlights the necessity of advanced signal processing algorithms capable of accurately extracting the signal for crack detection. These results show that TSWE with time is efficient in detecting RCF cracks by analyzing the impact-induced AE transients even in the presence of high operational noise.

Fourthly, although the crack did not exhibit observable growth during the period of the field study, there were a few AE transients (Figs. 5.12 and 5.13 in Sect. 5.3.2, that is, Figs. 5.30 and 5.31 in Sect. 5.5.2) that had energy distribution different with that of impact-induced AE transients (Figs. 5.10 and 5.11 in Sect. 5.3.2, that is, Figs. 5.28 and 5.29 in Sect. 5.5.2) in the time-frequency representation. These AE transients had more energy distributed in the higher frequency band of [350–700] kHz and were likely to be induced by the crack propagation process based on

the experience gained during laboratory fatigue tests on rail steel specimens. The classification and mechanism analysis of crack-related AE waves will be discussed in detail in the following section. It is however important to emphasize that the crack propagation process was naturally mixed with the impact process at such RCF cracks in the field. Figures 5.24 and 5.25 exhibit such a signal as recorded by the AE channel near the RCF crack (CH3) and the AE channel at 11.7 m away from the RCF crack (CH2), respectively. As can be seen, TSWE effectively identified the time of occurrence of CP-induced transients. This result corroborates that the time-TSWE is suitable for not only the detection of surface cracks (where both impact-induced AE waves and CP-induced AE waves could be observed) but also for the detection of internal cracks (where only CP-induced AE waves could be utilized).

In addition, the amplitudes of operational noise acquired by the sensor (CH1) on the healthy rail (Fig. 5.18) and the two sensors (CH2 and CH3) on the cracked rail (Figs. 5.19, 5.20, 5.21, 5.22, 5.23, 5.24 and 5.25) were found to be slightly different. This is mainly attributed to the difference in the positions where the AE sensors were installed. The sensor on the healthy rail was fixed at the middle span, while the sensors on the cracked rail were fixed near the sleeper. The operational noise at the middle span is noted to exhibit lightly higher amplitudes than that at the sleepers as supports.

(2) Crack location

In view of the complicated field condition, the source location methods discussed in Chap. 3 under controlled environment could not be applied directly in the field. Due to the lower energy of crack-related AE waves (leading to weak dispersive wave modes) and the high operational noise, the dispersion phenomenon was not clearly observed and the WTMAL is therefore would not be effective. Meanwhile, the TOA method based on the waveform in the time domain is also not reliable when the crack-related AE transients are submerged in high operational noise (as shown in Fig. 5.22).

TSWE with time is therefore proposed for rail crack location in the field. It helps to identify the arrival times of crack-related transients at the sensors. The crack can then be located based on the time difference between arrivals of individual AE transient at two sensors, similar as in the TOA method. In the setup of this study, the incipient RCF crack was detectable by an AE sensor 11.7 m away from the crack (CH2). Using the data from CH2 and CH3, the crack was located with errors less than 0.3 m.

For future study, additional train information such as speed and direction could be incorporated in the analysis to extend the working range of the AE sensors. Firstly, TSWE identifies the arrival time of the crack-related AE transients at the sensor. Secondly, the arrival time of the train wheel (that stimulates the AE transients when it passes the crack) at the sensor is then extracted from the waveform in the time domain (as shown in Fig. 5.18). Thirdly, given the speed of the train, the

distance between the crack and the sensor can be easily calculated. Further, given the direction in which the train is travelling, the exact location of the crack can be determined. Thus, instead of using the arrival times of AE transient at two neighboring sensors (as in the TOA method), the TSWE index together with the train information is able to identify the location of crack using the AE data of only one sensor (similar as in the WTMAL method). After taking into account the train information and AE waveform, the working range per AE sensor could be extended to 23.4 m along the rail track.

5.5 Classification of Crack-Related AE Waves Based on Enhanced SWT Scalogram

There are several types of AE waves related to rail crack, and these could be classified as impact-induced, CP-induced and CC-induced AE waves, as shown in Figs. 5.7, 5.8, 5.9, 5.10, 5.11, 5.12 and 5.13. For shallow RCF cracks (depth less than 2 mm), crack closure process as well as CC-induced AE waves are typically not evident. There are thus three types of AE waves encountered in the field tests, i.e. impact-induced AE waves, CP-induced AE waves and operational noise, which need to be carefully distinguished from each other to achieve accurate crack detection and quantification.

It is however not an easy task to classify these AE waves based on both of the CWT and SWT plots. For instance, with respect to the rolling noise in Fig. 5.9, the impact-induced AE wave in Fig. 5.11 and the CP-induced AE waves in Fig. 5.13 exhibit similar SWT contour plots, where the data are all clustered below 200 kHz. This problem could not be solved even after application of the characteristic frequency band, [200–700] kHz (as shown in Figs. 5.27, 5.28, 5.29, 5.30 and 5.31). Meanwhile, for those AE waves with high amplitudes (as shown in Figs. 5.10, 5.12, 5.28 and 5.30), the SWT plots normally have very concentrated colors while valuable information embedded in the blank area corresponding to low energy frequency components could be missed. The reason for this apparent problem is the wide range of SWT coefficients of the AE signal. The SWT coefficients for different AE signals are dramatically different from each other, rendering it difficult to classify them based on uniform criteria.

In order to make full use of the information embedded in frequency components of various energy levels and to distinguish different types of AE wave more efficiently, the gamma correction method is introduced to enhance the SWT plots. The enhanced SWT scalogram is finally proposed as an effective tool for AE wave classification in rail crack monitoring.

5.5.1 SWT Enhanced by Gamma Correction

Gamma correction or power law transformation is a common method in image processing to enhance the darker parts of an image (Gonzalez and Woods 2008). The gamma correction is applied to SWT coefficients matrix by the following function

$$S\bar{W}T(\omega, b) = C \times SWT(\omega, b)^{\gamma} \tag{5.19}$$

where C and γ are positive constants, and $SWT(\omega, b)$ and $S\bar{W}T(\omega, b)$ are the original SWT coefficients and the corrected SWT coefficients, respectively. Figure 5.26 plots $SWT(\omega, b)$ versus $S\bar{W}T(\omega, b)$ for various values of Y. The value of Y is determined to be 0.7 in this study based on the AE measurements in order to achieve good performance in AE wave classification.

The matrix of SWT coefficients is scaled by applying the gamma correction to reduce the dynamic range of SWT coefficients nonlinearly. The coefficients with low amplitudes (in which the features are easily overwhelmed by those with high amplitudes) can be mapped to a larger scale of the total range in a scalogram with absolute values of gamma-corrected SWT coefficients. The corrected SWT plot is then named enhanced SWT scalogram, for convenience.

5.5.2 Results and Discussion

Figures 5.27, 5.28, 5.29, 5.30 and 5.31 exhibits the waveform, original SWT plot and enhanced SWT scalogram of the operational noise, impact-induced AE waves

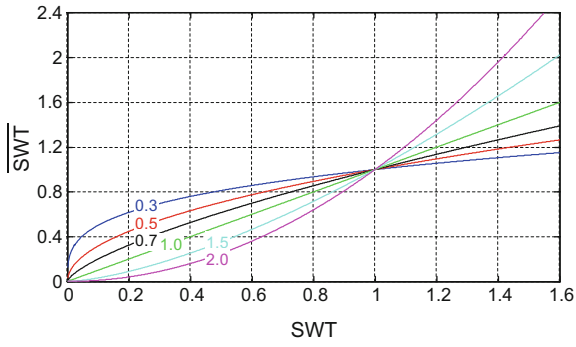

Fig. 5.26 Gamma correction curves for various values of γ

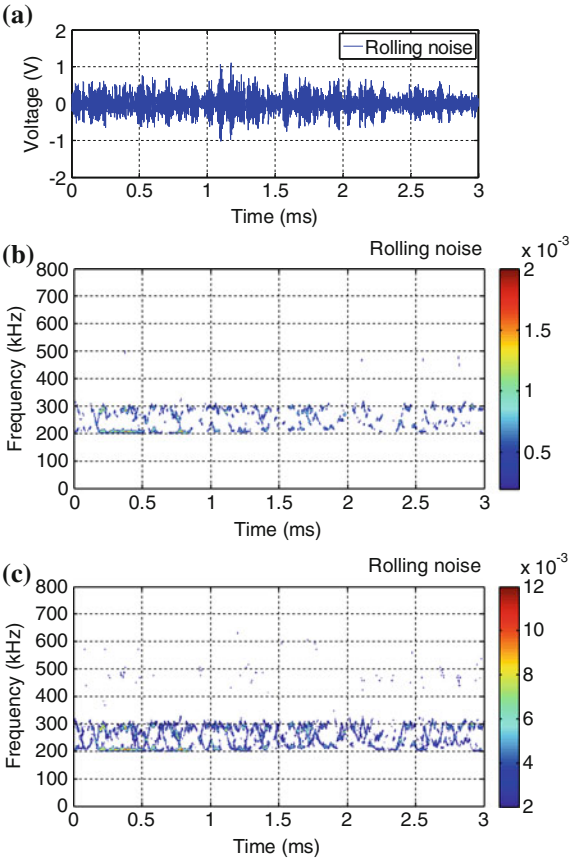

Fig. 5.27 Wheel-rail rolling noise: **a** waveform, **b** SWT plot and **c** enhanced SWT scalogram

and CP-induced AE waves, respectively. It should be noted that the SWT results were obtained after applying the characteristic frequency band and denoising threshold as specified in Sect. 5.4.3. The enhanced SWT scalogram reveals distinctly the different patterns for the different types of AE waves, which is summarized as below.

(1) The energy of operational (rolling) noise are almost all clustered in the lower frequency band of [200–350] kHz.
(2) The energy of impact-induced AE waves are mainly concentrated in the lower frequency band of [200–350] kHz, and spread out to the higher frequency band of [350–700] kHz.
(3) The energy of CP-induced AE waves are distributed in both the lower frequency band of [200–350] kHz and the higher frequency band of [350–700] kHz. The ratio of energy in the higher frequency band is clearly larger than that of impact-induced AE waves.

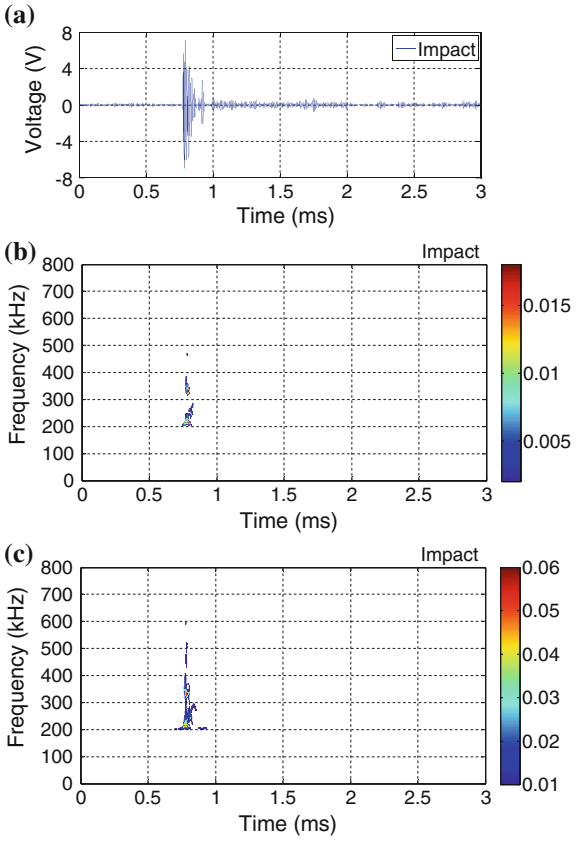

Fig. 5.28 Imapct-induced AE wave with a higher amplitude: **a** waveform, **b** SWT plot and **c** enhanced SWT scalogram

Based on these observations, AE waves in the field rail crack monitoring can be then distinguished using a classification index similar to that in Sect. 4.3. Efficient classification of the different types of AE waves induced by the various mechanisms will be important to achieve accurate sizing of crack.

5.6 Concluding Remarks

This chapter focuses on the AE crack monitoring of rail track under actual field condition with complex crack formations and noisy environment. The crack-related AE transients were found to be easily submerged in high operational noise. Traditional AE parameter analysis is incapable of identifying the presence of cracks, and the crack location method proposed in the previous chapter may become ineffective. In this regard, a crack monitoring strategy with improved AE

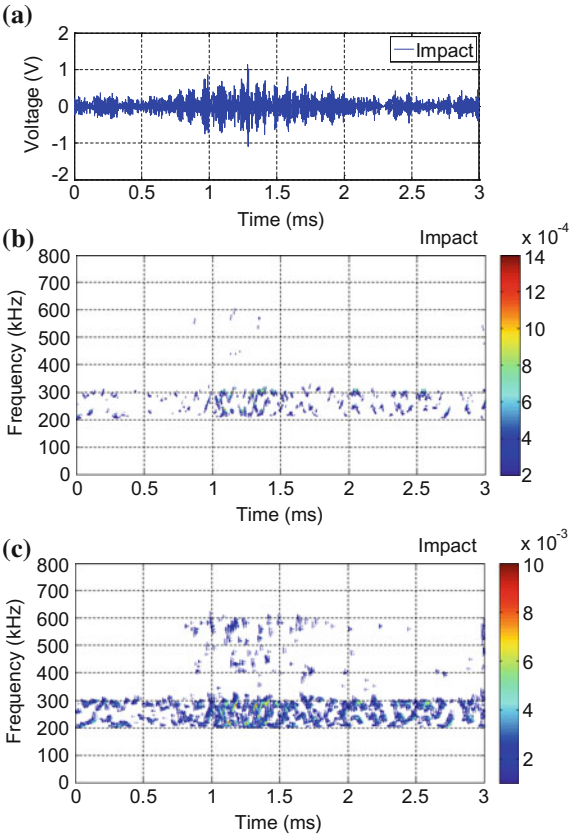

Fig. 5.29 Imapct-induced AE wave with a lower amplitude: **a** waveform, **b** SWT plot and **c** enhanced SWT scalogram

signal processing algorithms was developed and their performance evaluated and described in this chapter.

(1) In the monitoring of RCF cracks on rail track, several types of AE waves may be present and mixed with each other. They were respectively CP-induced AE waves, CC-induced AE waves, impact-induced AE waves and operational noise. Impact-induced AE wave, which was not covered in the previous laboratory study and simulated field study, is considered to be a type of secondary AE wave, which was demonstrated to be effective in identifying the existence of cracks.

(2) Wavelet entropy was used to quantitatively identify the crack-related transients in the AE signal. In order to represent AE waves more clearly in the time-frequency domain, SWT was introduced to explore the characteristics of various AE measurements. For the SWT coefficients of AE signal, the non-extensive Tsallis entropy was adopted instead of the extensive Shannon entropy. TSWE was then put forward as an index with time to detect the existence and location of RCF cracks in the field. The key parameters in TSWE were appropriately determined based on the experimental data.

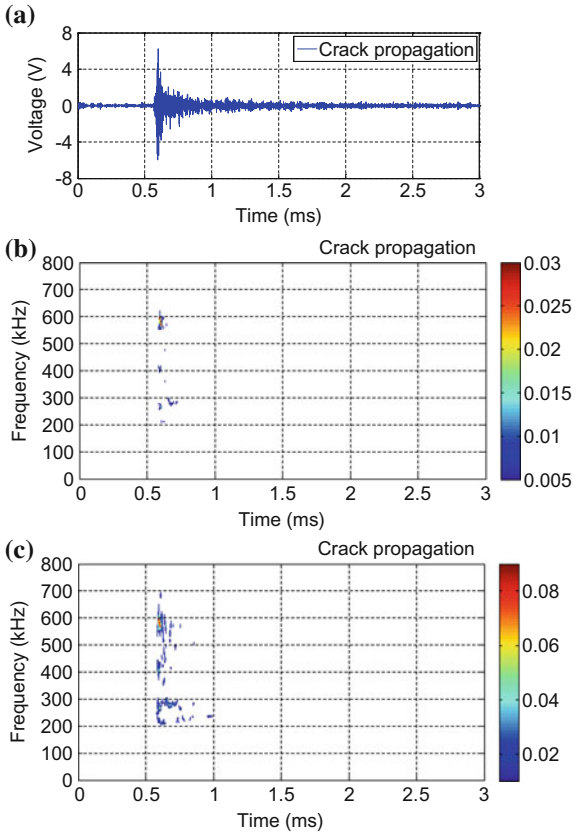

Fig. 5.30 CP-induced AE wave with a higher amplitude: **a** waveform, **b** SWT plot and **c** enhanced SWT scalogram

(3) The performance of TSWE was validated by a series of field tests where an incipient RCF crack was successfully identified and located with the sensor located 11.7 m away with errors less than 0.3 m. Although the sensing distance of sensors mounted on the track is relatively short compared to the length of railway lines, the crack detection strategy proposed can be applied to critical rail sections such as curved sections where lateral forces could result in high occurrences of cracks. In addition, the time-TSWE can be used to detect cracks not only in rail head but also in rail web and foot. By identifying crack-related AE waves including impact-induced ones and CP-induced ones, the time-TSWE is capable of detecting both surface and internal cracks.

(4) The enhanced SWT scalogram, which was inspired by the idea of gamma correction, was proposed and found to be able to classify AE measurements efficiently into three types, i.e. impact-induced AE waves, CP-induced AE waves and operational noise. Accurate classification is necessary to allow quantitative analysis of CP-induced AE waves and estimating of the crack size in the future.

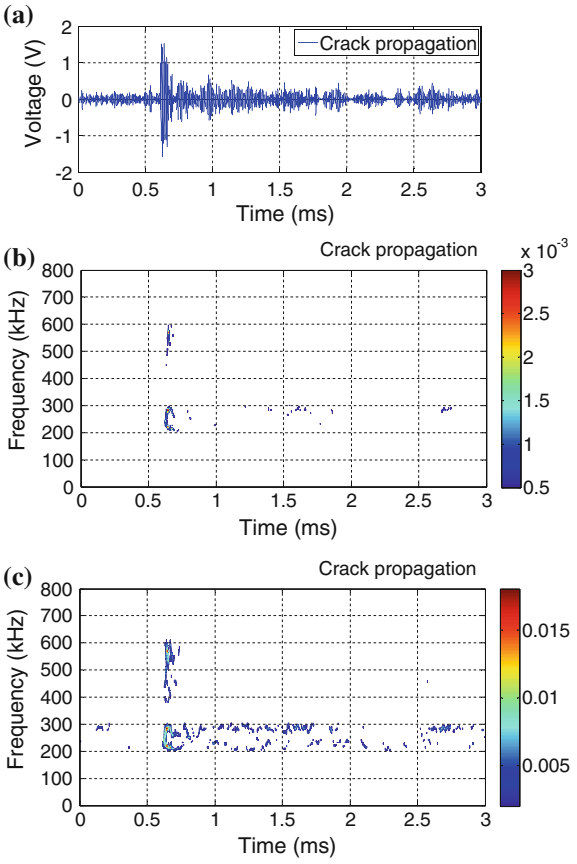

Fig. 5.31 CP-induced AE wave with a lower amplitude: **a** waveform, **b** SWT plot and **c** enhanced SWT scalogram

(5) Due to limited duration of access to the site, we could only carry out continuous monitoring over a set period. Few CP-induced and no CC-induced AE waves were acquired. For future work, long-term AE monitoring of rail crack should be done to record more CP-induced and CC-induced AE waves. The relationship between the AE waves and crack growth could be deeply studied.

References

Abe, S. (1999). Correlation induced by Tsallis' nonextensivity. *Physica A: Statistical Mechanics and its Applications, 269*(2), 403–409.

Al-Dossary, S., Hamzah, R., & Mba, D. (2009). Observations of changes in acoustic emission waveform for varying seeded defect sizes in a rolling element bearing. *Applied Acoustics, 70* (1), 58–81.

Auger, F., Flandrin, P., Lin, Y.-T., McLaughlin, S., Meignen, S., Oberlin, T., et al. (2013). Time-frequency reassignment and synchrosqueezing: An overview. *IEEE Signal Processing Magazine, 30*(6), 32–41.

Bassim, M. N., Lawrence, S. S., & Liu, C. D. (1994). Detection of the onset of fatigue crack growth in rail steels using acoustic emission. *Engineering Fracture Mechanics, 47*(2), 207–214.

Bruzelius, K., & Mba, D. (2004). An initial investigation on the potential applicability of acoustic emission to rail track fault detection. *NDT and E International, 37*(7), 507–516.

Cover, T. M., & Thomas, J. A. (2012). *Elements of information theory*. US: Wiley.

Daubechies, I., Lu, J. F., & Wu, H. T. (2011). Synchrosqueezed wavelet transforms: an empirical mode decomposition-like tool. *Applied and computational harmonic analysis, 30*(2), 243–261.

Daubechies, I., & Maes, S. (1996). A nonlinear squeezing of the continuous wavelet transform based on auditory nerve models. In A. Aldroubi & M. Unser (Eds.), *Wavelets in medicine and biology* (pp. 527–546). Boca Raton: CRC Press.

Dong, S., Tang, B., & Chen, R. (2013). Bearing running state recognition based on non-extensive wavelet feature scale entropy and support vector machine. *Measurement, 46*(10), 4189–4199.

Donoho, D. L., & Johnstone, I. M. (1994). Ideal spatial adaptation by wavelet shrinkage. *Biometrika, 81*(3), 425-455.

Ekici, S., Yildirim, S., & Poyraz, M. (2008). Energy and entropy-based feature extraction for locating fault on transmission lines by using neural network and wavelet packet decomposition. *Expert Systems with Applications, 34*(4), 2937–2944.

Ferrando Chacon, J. L., Kappatos, V., Balachandran, W., & Gan, T.-H. (2015). A novel approach for incipient defect detection in rolling bearings using acoustic emission technique. *Applied Acoustics, 89,* 88–100.

Gonzalez, R. C., & Woods, R. E. (2008). *Digital image processing* (3rd ed.). US: Pearson/Prentice Hall.

Goupillaud, P., Grossmann, A., & Morlet, J. (1984). Cycle-octave and related transforms in seismic signal analysis. *Geoexploration, 23*(1), 85–102.

Gutkin, R., Green, C., Vangrattanachai, S., Pinho, S., Robinson, P., & Curtis, P. (2011). On acoustic emission for failure investigation in CFRP: Pattern recognition and peak frequency analyses. *Mechanical Systems and Signal Processing, 25*(4), 1393–1407.

Hamstad, M. A. (2007). Acoustic emission signals generated by monopole (pencil-lead break) versus dipole sources: Finite element modeling and experiments. *Journal of Acoustic Emission, 25,* 92–107.

Khamedi, R., Fallahi, A., & Refahi Oskouei, A. (2010). Effect of martensite phase volume fraction on acoustic emission signals using wavelet packet analysis during tensile loading of dual phase steels. *Materials and Design, 31*(6), 2752–2759.

Kostryzhev, A. G., Davis, C. L., & Roberts, C. (2013). Detection of crack growth in rail steel using acoustic emission. *Ironmaking and Steelmaking, 40*(2), 98–102.

Li, D., Kuang, K. S. C., & Koh, C. G. (2015). Detection and quantification of fatigue cracks in rail steel using acoustic emission technique. In *Proceedings of the 10th International Workshop on Structural Health Monitoring*, Stanford, CA, USA, pp. 2529–2536.

Li, C., & Liang, M. (2012). Time–frequency signal analysis for gearbox fault diagnosis using a generalized synchrosqueezing transform. *Mechanical Systems and Signal Processing, 26,* 205–217.

Liu, Z., Hu, Q., Cui, Y., & Zhang, Q. (2014). A new detection approach of transient disturbances combining wavelet packet and Tsallis entropy. *Neurocomputing, 142,* 393–407.

Liu, J. L., Wang, Z. C., Ren, W. X., & Li, X. X. (2015). Structural time-varying damage detection using synchrosqueezing wavelet transform. *Smart Structures and Systems, 15*(1), 119–133.

Marec, A., Thomas, J. H., & El Guerjouma, R. (2008). Damage characterization of polymer-based composite materials: Multivariable analysis and wavelet transform for clustering acoustic emission data. *Mechanical Systems and Signal Processing, 22*(6), 1441–1464.

Mba, D. (2003). Acoustic emissions and monitoring bearing health. *Tribology Transactions, 46* (3), 447–451.

Ni, Q. Q., & Iwamoto, M. (2002). Wavelet transform of acoustic emission signals in failure of model composites. *Engineering Fracture Mechanics, 69*(6), 717–728.

Piotrkowski, R., Castro, E., & Gallego, A. (2009). Wavelet power, entropy and bispectrum applied to AE signals for damage identification and evaluation of corroded galvanized steel. *Mechanical Systems and Signal Processing, 23*(2), 432–445.

Ren, W. X., & Sun, Z. S. (2008). Structural damage identification by using wavelet entropy. *Engineering Structures, 30*(10), 2840–2849.

Sause, M. G. R., Gribov, A., Unwin, A. R., & Horn, S. (2012). Pattern recognition approach to identify natural clusters of acoustic emission signals. *Pattern Recognition Letters, 33*(1), 17–23.

Shannon, C. E. (1948). A mathematical theory of communication. *Bell System Technical Journal, 27*(3), 379–423, 623–656.

Tandon, N., Yadava, G. S., & Ramakrishna, K. M. (2007). A comparison of some condition monitoring techniques for the detection of defect in induction motor ball bearings. *Mechanical Systems and Signal Processing, 21*(1), 244–256.

Thakkar, N. A., Steel, J. A., & Reuben, R. L. (2010). Rail-wheel interaction monitoring using acoustic emission: A laboratory study of normal rolling signals with natural rail defects. *Mechanical Systems and Signal Processing, 24*(1), 256–266.

Thakur, G., Brevdo, E., Fučkar, N. S., & Wu, H. T. (2013). The synchrosqueezing algorithm for time-varying spectral analysis: Robustness properties and new paleoclimate applications. *Signal Processing, 93*(5), 1079–1094.

Tong, S., Bezerianos, A., Paul, J., Zhu, Y., & Thakor, N. (2002). Nonextensive entropy measure of EEG following brain injury from cardiac arrest. *Physica A: Statistical Mechanics and its Applications, 305*(3), 619–628.

Tsallis, C. (1988). Possible generalization of Boltzmann-Gibbs statistics. *Journal of Statistical Physics, 52*(1–2), 479–487.

Tsallis, C. (2009). Nonadditive entropy and nonextensive statistical mechanics -an overview after 20 years. *Brazilian Journal of Physics, 39,* 337–356.

Tsallis, C., Mendes, R., & Plastino, A. R. (1998). The role of constraints within generalized nonextensive statistics. *Physica A: Statistical Mechanics and its Applications, 261*(3), 534–554.

Wandowski, T., Malinowski, P., Kudela, P., & Ostachowicz, W. (2011). Guided wave-based detection of delamination and matrix cracking in composite laminates. *Proceedings of the Institution of Mechanical Engineers Part C: Journal of Mechanical Engineering Science, 225* (1), 123–131.

Wang, Z. C., Ren, W. X., & Liu, J. L. (2013). A synchrosqueezed wavelet transform enhanced by extended analytical mode decomposition method for dynamic signal reconstruction. *Journal of Sound and Vibration, 332*(22), 6016–6028.

Widner, R. L., & Littmann, W. E. (1976). Bearing damage analysis. In T. R. Shives & W. A. Willard (Eds.), *National Bureau of Standard Special Publication 423* (pp. 67–84).

Widodo, A., Kim, E. Y., Son, J. D., Yang, B. S., Tan, A. C. C., Gu, D. S., et al. (2009). Fault diagnosis of low speed bearing based on relevance vector machine and support vector machine. *Expert Systems with Applications, 36*(3), 7252–7261.

Zhang, X., Feng, N., Wang, Y., & Shen, Y. (2015). Acoustic emission detection of rail defect based on wavelet transform and Shannon entropy. *Journal of Sound and Vibration, 339,* 419–432.

Chapter 6
Conclusions and Future Work

With the aim of realizing a safe and smooth operation of the railway system, this thesis focuses on the rail crack monitoring using AE technique. The study begins with controlled laboratory and field experimental work where PLB-simulated AE sources were used to simulate cracks in rail track and fatigue cracks were created in rail steel specimens. After that, the study continues with field experimental work where real cracks in rail track were used for testing in the presence of high operational noise. A rail crack monitoring strategy was proposed, comprising of a noise cancellation method, an AE wave classification method, a crack sizing method and a crack identification and location method. The main conclusions and recommendations for future work are summarized in this chapter.

6.1 Conclusions

The conclusions can be grouped into six aspects related to the crack monitoring strategy and these are presented as follows:

(1) Classification of different AE waves

In this study, AE signals associated with rail cracks, including CP-induced AE waves, CC-induced AE waves, wheel-rail impact-induced AE waves and railway noise, were obtained through laboratory fatigue tests on rail steel specimens and field tests on operational rail tracks. As fatigue cracks typically grow very slowly over a long period of time, the majority of the AE waves collected were secondary AE events, that is, CC-induced AE waves (acquired in the laboratory fatigue tests) and impact-induced AE waves (acquired in the field tests).

It was found that the energy distribution of different types of AE waves varies in the time-frequency domain. A classification index based on WP extracted from CWT plot was established and shown to work well in distinguishing CP-induced and CC-induced AE waves under laboratory environment. Furthermore, the

D. Li, *Rail Crack Monitoring Using Acoustic Emission Technique*,
Springer Theses, https://doi.org/10.1007/978-981-10-8348-8_6

enhanced SWT scalogram was proposed instead of CWT plot to achieve a clearer time-frequency representation and a more efficient classification of multiple types of AE measurements under field environment.

(2) Crack sizing using AE waves

AE signals recorded during laboratory fatigue tests were studied for estimating the size of crack. A novel method was developed to quantify the fatigue crack length by taking advantage of the CC-induced AE waves, the count rate of which was found to be positively correlated with crack length. The results of the fatigue tests conducted showed clear evidence of the ability of the proposed method to quantify the crack length accurately.

In contrast with other AE crack sizing methods, the proposed method does not require prior knowledge of initial crack length, integration of AE data or real-time load amplitude, to determine the crack length, allowing it to be applied to both new and existing structures. Although the novel method can be applied to only fatigue cracks under low load ratios, this is nevertheless the prevailing condition for a large number of civil engineering structures including rail tracks.

(3) Propagation features of AE waves in rail track

This thesis was primarily focused on the crack detection in the rail head, which is one of the most vulnerable parts of the rail track. PLB-induced AE signals recorded on an actual rail track were studied for investigating the propagation features of AE waves in rail head. Here, it is recommended that the AE sensors be mounted at the field side of rail head (as opposed to underside of rail head and middle of rail web). The dominant velocity wave was found to be approximately 3000 m/s. Furthermore, AE waves arising from the rail head was found to be mainly guided in the rail head and they exhibit dispersion phenomena when propagating along the rail head.

(4) Noise cancellation

The operational noise of railway is extremely high, and the AE waves related to cracks are easy to be submerged in the noise. It is therefore necessary to improve the SNR of AE measurements by careful selection of instrumentation and use of advanced signal processing algorithms. The HT-based noise cancellation method proposed in this study provides a new easy-to-use tool in post-processing of AE signal. In addition, the characteristic frequency band, time window length and threshold in the calculation of TSWE also helped to significantly suppress the influence of noise.

(5) Crack identification and location in rail track

One of the most important contributions of this thesis compared to previous studies is the acquisition and analyses of field AE data obtained for real rail material and profile, complex crack conditions and field operational noise, which were demonstrated to significantly influence the performance of AE technique and the corresponding algorithms to be used for successful crack detection.

In the location of AE sources generated by PLB on rail track, the WTMAL method which employs the time-frequency analysis was found to be more effective than the traditional TOA method which relies on the detection of waveform amplitude threshold. The average working range of each AE sensor reached 30.0 m after having taken into account the railway noise. However, this could not be achieved under field environment where complex crack conditions and high operational noise exist.

In order to identify the crack-related AE transients in the noisy AE signal, Tsallis entropy of SWE coefficients was applied as a quantitative index. TSWE with time was finally proposed to identify the existence and location of cracks in the field. After the key parameters were appropriately determined, the time-TSWE was demonstrated to be able to successfully locate an incipient RCF crack at 11.7 m away from the sensor with errors less than 0.3 m. In addition, the time-TSWE has the capability to detect both surface and internal cracks.

(6) Rail crack monitoring using the track-based approach

The rail crack monitoring strategy proposed in this study is classified as a track-based approach. With sensors installed on the rail track, the approach offers continuous monitoring of critical rail sections, such as curved sections where lateral forces could result in higher occurrences of cracks. In contrast, a train-based approach, in which the sensors are attached to the inspection train, is limited to monitoring of the railway line during scheduled timings. Although the present study is developed for track-based implementation, the results can also provide valuable insights for the use of AE technique in train-based inspection system.

6.2 Future Work

Some recommendations for future research work and field applications are listed as follows:

(1) For the crack sizing method derived from the AE data acquired during the fatigue tests in the laboratory, more studies are needed to investigate the effects of loading and specimen geometry on the generation of AE waves during fatigue crack growth. The proposed crack sizing method based on CC-induced AE waves may then be further developed accordingly. Besides, it is worth to simulate the RCF crack in the laboratory and to quantitatively analyze the AE signal induced by such kind of cracks.
(2) For crack identification in the presence of high operational noise, more advanced denoising techniques for both hardware and software could be introduced. The operating bandwidth of AE sensors and analog filters could be customized to fit the frequency band of interest. More adaptive denoising techniques could be applied following the wavelet analysis instead of using a simple hard-threshold filtering.

(3) For the classification of AE waves induced by different mechanisms, machine learning algorithms could be introduced to take into account multiple characteristics of AE waves including their time-frequency characteristics proposed in this study. This would help to reduce the uncertainty in the analyses, particularly in field application studies.
(4) Long-term monitoring of rail track in the field would yield interesting information for further research. The influence of multiple cracks on the crack location and sizing methods could be studied. Efforts could also be directed to monitor fatigue cracks in the rail web and foot using AE technique.
(5) As highlighted earlier, rail crack monitoring could be implemented as a track-based approach or a train-based approach. Although more challenging, the train-based approach has the benefit of being able to inspect the entire railway line. The application of AE technique for train-based rail crack detection could be carried out by using traditional piezoelectric (PZT) AE sensors installed on the wheel or laser interferometers mounted on the bogie. AE signal processing algorithms used for track-based approach could be further developed for train-based approach. Progress in both approaches would be beneficial for a safer and smoother rail operation.